Universität Karlsruhe (TH)

IEKP-KA/2004-14

Entwicklung von Analyse-Software und Studie zur Messung des CP-Eigenzustands von Higgs-Bosonen mit dem CMS-Experiment am LHC

Sven Schalla

Diplomarbeit

an der Fakultät für Physik
der Universität Karlsruhe

Referent: Prof. Dr. G. Quast
Institut für Experimentelle Kernphysik

Korreferent: Prof. Dr. Th. Müller
Institut für Experimentelle Kernphysik

1. Juni 2004

Contents

List of Figures

List of Tables

Introduction

The Standard Model of Particle Physics (SM) is the accepted theory of elementary particles and their interactions. It provides an elegant theoretical framework and has successfully been tested in many precision experiments. However, one fundamental part of the theory has still not been confirmed experimentally: the Higgs sector. In the Standard Model Lagrangian a mass term can be generated by applying the so-called Higgs mechanism. This mechanism predicts a new particle, the Higgs boson. Although the Higgs mechanism has been introduced four decades ago, experimental sensitivity remains extremely limited.
The search for the Higgs boson is definitely one of the most exciting topics in particle physics. In the Standard Model, the Higgs mass is a priori a free parameter, but certain limitations require the mass to be between 100 and 200 GeV. In extensions that go beyond the Standard Model, e.g. supersymmetric theories, the Higgs sector is more complex. The Higgs bosons of these extended models differ from the SM Higgs boson in their mass and quantum numbers.
The CMS[1] detector, which will be operated at the LHC[2] at CERN[3] is designed to observe the Higgs boson. Great attention has been payed to the muon system. That makes the CMS detector well suited for the observation of the channel $H \rightarrow ZZ \rightarrow 4\mu$. This channel has the outstanding signature of four isolated muons in the final state.
This diploma thesis is addressed to the channel $H \rightarrow ZZ \rightarrow 4\mu$ at a Higgs boson mass of 200 GeV. In order to achieve realistic results, signal and background events were processed through full detector simulation. The study can be divided into two parts. The first part of the analysis discusses the discovery potential of the Higgs boson in the channel $H \rightarrow ZZ \rightarrow 4\mu$ at the CMS detector. The second part considers the possibility to determine the CP eigenvalue of the Higgs boson by analysing the angular distributions of the muons. The Standard Model Higgs boson can be distinguished from some other models by its CP eigenvalue.
In chapter one, a brief description of the Standard Model is given with special interest in the electroweak symmetry breaking and the Higgs mechanism. Different production and decay processes are presented in chapter two. In chapter three, the CMS detector and its components are explained. The description is focused on the muon system. In chapter four, the software needed to perform the full detector simulation, which was one of the challenges of the study, as well as the reconstruction and analysis software, is introduced. Event simulation and the analysis setup for the channel $H \rightarrow ZZ \rightarrow 4\mu$ is described in more detail in chapter five. The analysis results are divided into three chapters. In chapter six, the results of detector resolution and reconstruction efficiency studies are reported. An estimation of the observation potential of the signal at a Higgs boson mass of 200 GeV is given in chapter seven. In this chapter a cut optimisation has been performed. Finally, the results of the analysis to determine the CP eigenvalue of the Higgs boson are presented in chapter eight.

[1]Compact Muon Solenoid
[2]Large Hadron Collider
[3]European Organization for Nuclear Research in Geneva, Switzerland

Chapter 1

Theory of the Standard Model

1.1 The Standard Model - A Short Overview

The Standard Model of particle physics describes elementary particles and their interactions. Elementary particles are divided into two groups, quarks and leptons, and three families. All of these particles are fermions, i.e. particles with half-integer spin. Particles with integer spin are called bosons. The particles of one family couple to each other through weak interaction. Quarks and leptons, arranged according to their families, are listed in tables 1.1 and 1.2.
The eigenstates of the quarks in the electroweak interaction are not equal to their mass eigenstates. The mass eigenstates d, s, b, and the electroweak eigenstates d', s', b', are connected by the unitary CKM Matrix.
In order to fulfill the Pauli principle, quarks need to have an extra quantum number called colour. There are three different colours (and their respective anti-colours): red, green and blue. Observable particles have to be colourless. There are three-quark-states, baryons, that have quarks of all three colours, and two-quark-states, mesons, that consist of quarks of one colour and the according anti-colour.
The Standard Model also describes three of the four (known) interactions, electromagnetic, weak and strong interaction. These interactions are described by exchange of gauge bosons which are listed in table 1.3. Up to now, gravitation has not been included. But as its strength is small compared to the other interactions, it may be neglected in the case of high energy particle physics. A more detailed description can be found in [1].

first family	second family	third family	isospin T^3	charge Q	hypercharge Y
$\begin{pmatrix} u \\ d' \end{pmatrix}_L$	$\begin{pmatrix} c \\ s' \end{pmatrix}_L$	$\begin{pmatrix} t \\ b' \end{pmatrix}_L$	$\begin{pmatrix} \frac{1}{2} \\ -\frac{1}{2} \end{pmatrix}$	$\begin{pmatrix} \frac{2}{3} \\ -\frac{1}{3} \end{pmatrix}$	$\frac{1}{3}$
u_R	c_R	t_R	0	$\frac{2}{3}$	$\frac{4}{3}$
d_R	s_R	b_R	0	$-\frac{1}{3}$	$-\frac{2}{3}$

Table 1.1: The quarks and their quantum numbers.

first family	second family	third family	isospin T^3	charge Q	hypercharge Y
$\begin{pmatrix} e \\ \nu_e \end{pmatrix}_L$	$\begin{pmatrix} \mu \\ \nu_\mu \end{pmatrix}_L$	$\begin{pmatrix} \tau \\ \nu_\tau \end{pmatrix}_L$	$\begin{pmatrix} -\frac{1}{2} \\ \frac{1}{2} \end{pmatrix}$	$\begin{pmatrix} -1 \\ 0 \end{pmatrix}$	-1
e_R	μ_R	τ_R	0	-1	-2

Table 1.2: The leptons and their quantum numbers.

Name	Charge	Mass [GeV]	Interaction
g (Gluon)	0	0	Strong Interaction
γ (Photon)	0	0	Electromagnetic Interaction
Z^0	0	91.187	Weak Interaction
$W^{+/-}$	+/-	80.423	Weak Interaction

Table 1.3: Gauge Bosons in the Standard Model.

1.2 Local Gauge Invariance and QED

At first, a short review of the manifestations of gauge invariance in classical electrodynamics is given.
A global gauge transformation of the vector field $A^\mu = (\phi; \mathbf{A})$ with

$$A^\mu \to A^{'\mu} = A^\mu - \partial^\mu \chi \,, \tag{1.1}$$

where $\chi(x)$ is an arbitrary function of the coordinate, leaves the fields $\overrightarrow{E}$ and $\overrightarrow{B}$ invariant since

$$\vec{B} = \nabla \times \vec{A}\,, \;\; \vec{E} = -\nabla\phi - \frac{\partial \vec{A}}{\partial t} \,. \tag{1.2}$$

The electromagnetic field-strength tensor

$$F^{\mu\nu} = -F^{\nu\mu} = \partial^\nu A^\mu - \partial^\mu A^\nu = \begin{pmatrix} 0 & E_1 & E_2 & E_3 \\ -E_1 & 0 & B_3 & -B_2 \\ -E_2 & -B_3 & 0 & B_1 \\ -E_3 & B_2 & -B_1 & 0 \end{pmatrix} , \tag{1.3}$$

remains unchanged. Different potentials yield the same electromagnetic fields, thus describe the same physics. This is a manifestation of the gauge invariance of classical electrodynamics. If global gauge invariance is applied to quantum mechanics, the transformation is

$$\begin{aligned} \vec{A} \quad &\to \quad \vec{A}' = \vec{A} + \nabla\chi \,, \\ \phi \quad &\to \quad \phi' = \phi - \frac{\partial\chi}{\partial t} \,, \\ \psi \quad &\to \quad \psi' = e^{iq\chi}\psi \,, \end{aligned}$$

in order to fulfill the Schrödinger equation. Quantum-mechanical observables involve inner products of the form:

$$\langle O \rangle = \int \psi^* O \psi, \tag{1.4}$$

thus they are unaffected by a global phase rotation:

$$\psi \to \psi' = e^{iq\chi}\psi \; . \tag{1.5}$$

But what happens, if local phase invariance is applied?

$$\begin{aligned}\psi &\to e^{i\alpha(x)}\psi \; , \\ \overline{\psi} &\to e^{-i\alpha(x)}\overline{\psi}\end{aligned}$$

Can quantum mechanics be formulated to be invariant under local phase rotations? This question will lead to the interaction of particles with fields. Taking the Lagrangian of a free Dirac Particle

$$\mathcal{L} = i\overline{\psi}\gamma^\mu\partial_\mu\psi - m\overline{\psi}\psi \; , \tag{1.6}$$

one can see, that the last term is local gauge invariant, but for the derivative

$$\partial_\mu\psi \to e^{i\alpha(x)}\partial_\mu\psi + ie^{i\alpha(x)}\psi\partial_\mu\alpha, \tag{1.7}$$

invariance is broken by the term $\partial_\mu\alpha$.
However, local phase invariance may be achieved, if the gradient ∂_μ is replaced by the gauge-covariant derivative

$$D_\mu \equiv \partial_\mu - ieA_\mu \; , \tag{1.8}$$

where e is the charge of the particle described by $\psi(x)$ and the transformation of the field $A_\mu(x)$ under phase rotations is given by:

$$A_\mu \to A'_\mu \equiv A_\mu + \frac{1}{e}\partial_\mu\alpha \; . \tag{1.9}$$

For the gauge-covariant derivative

$$D_\mu\psi \to e^{i\alpha(x)}D_\mu\psi \tag{1.10}$$

holds and the Lagrangian is invariant.
The required transformation law (1.9) for the four-vector A_μ is exactly the form (1.1) of a gauge transformation in electrodynamics. Moreover, the covariant derivative corresponds to the familiar replacement $p \to p - eA$.
Regarding A_μ as the photon field and adding an invariant term corresponding to the kinetic energy to the Lagrangian one gets:

$$\mathcal{L} = \overline{\psi}(i\gamma^\mu\partial_\mu - m)\psi + e\overline{\psi}\gamma^\mu A_\mu\psi - \frac{1}{4}F_{\mu\nu}F^{\mu\nu} \; . \tag{1.11}$$

Thus the interacting field theory QED is suggested by local gauge invariance. The addition of a mass term $\frac{1}{2}m^2A_\mu A^\mu$ is prohibited by gauge invariance. The gauge particle, the photon, must be *massless*.
It is possible to extend the ideas of local gauge invariance to more complicated gauge groups than the group of phase rotations. Construction of the $SU(3)$ color gauge theory for the interactions of color triplet quarks will lead to QCD and the introduction of gluons as gauge bosons. The appearance of interactions among gluons is a consequence of the non-Abelian nature of the gauge symmetry.
In QED and QCD, gauge bosons remain massless. A mass term in the corresponding Lagrangian would spoil local gauge invariance. This causes serious problems if we want to apply gauge symmetry to weak interaction, knowing that the bosons, $W^\pm$, Z, have mass. This will be discussed in the next sections.

1.3 V-A Theory of Weak Interaction

Before constructing the local gauge theory, it is necessary to recount some basic elements of weak interaction phenomenology.
Observing the nuclear beta decay of polarized ^{60}Co nuclei it was found that neutrinos occur in left-handed helicity states only and anti-neutrinos in right-handed states only. This parity non-conserving behavior in weak interaction can be explained with V-A theory.
Using the chirality-projection-operators $P_R = \frac{1}{2}(1+\gamma^5)$ and $P_L = \frac{1}{2}(1-\gamma^5)$, any Dirac-spinor u can be divided into two chirality components:

$$u = \frac{1}{2}(1+\gamma^5)u + \frac{1}{2}(1-\gamma^5)u = u_R + u_L \tag{1.12}$$

The spinors u_R and u_L are called right- and left-handed.
As an example for charged weak interaction we take the $e^+\overline{\nu_e}$ - vertex.

The form of charged current is:

$$J_\mu \equiv J_\mu^+ = \overline{u_e}\gamma_\mu \frac{1}{2}(1-\gamma^5)u_\nu \tag{1.13}$$

There are two terms at the vertex:

- The vector-current
$$V^\mu = \overline{\psi(e)}\gamma^\mu\psi(\nu) \tag{1.14}$$
that transforms like a four-vector.
- The axial-vector-current
$$A^\mu = \overline{\psi(e)}\gamma^\mu\gamma^5\psi(\nu) \tag{1.15}$$
that transforms like an axial-vector.

The axial-vector behaves like a vector under Lorentz-transformations, but keeps its sign under parity transformation. So, mixing vector- and axial-vector currents violates parity conversation. The chirality-projection-operators fulfill the relation $P_L^2 = P_L$, and charged current of the $e^+\overline{\nu_e}$-vertex can be transformed into:

$$\overline{u}_e\gamma_\mu \frac{1-\gamma^5}{2} u_\nu = \overline{u}_e\gamma_\mu \left(\frac{1-\gamma^5}{2}\right)^2 u_\nu = \overline{(u_e)}_L\gamma_\mu(u_\nu)_L \; . \tag{1.16}$$

Only left-handed components participate in this weak interaction. Matrix elements of charged weak interaction contains only left-handed components of spinors and right-handed components of anti-spinors.

The neutral weak current is not as simple. Instead of the purely V-A vertex for W bosons, the Z bosons vertex has a mixed form:

$$\gamma^\mu(c_V^f - c_A^f\gamma^5) \; . \tag{1.17}$$

The coefficients depend on the particular particle involved in the interaction.

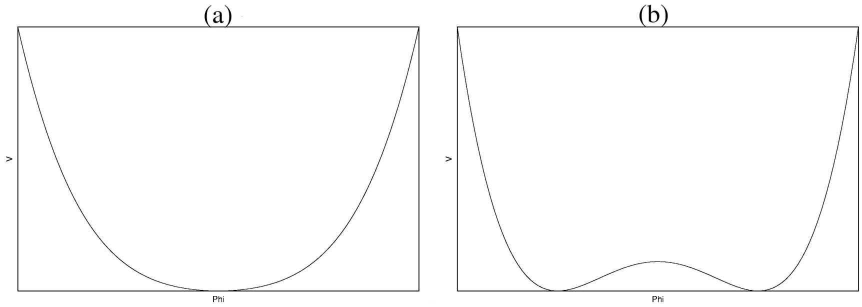

Figure 1.1: The Higgs Potential with (a) $\mu^2 > 0$ and (b) $\mu^2 < 0$.

1.4 Spontaneous Symmetry Breaking

Symmetry principles are fundamental for gauge invariance. They will be inspected more closely in this section. The Lagrangian may display an imperfect or explicitly broken symmetry, or it may happen that the Lagrangian is symmetric but the physical vacuum does not respect the symmetry. In the latter case, the symmetry of the Lagrangian is called spontaneously broken.
To explore the possibilities, it is convenient to consider a scalar field described by the Lagrangian

$$\mathcal{L} \equiv T - U = \frac{1}{2}\left(\partial_\mu \phi\right)^2 - \left(\frac{1}{2}\mu^2\phi^2 + \frac{1}{4}\lambda\phi^4\right) \quad , \text{ with } \lambda \geq 0\ . \tag{1.18}$$

We have required the Lagrangian to be invariant under the symmetry operation $\phi \to -\phi$. The two possible forms of the potential are shown in figure 1.1. Case (a), where $\mu^2 > 0$, is familiar. It simply describes a scalar field with mass μ. The ϕ^4 term denotes a four particle vertex with coupling λ implying that ϕ is a self-interacting field. The ground state (vacuum) corresponds to $\phi = 0$. It obeys the reflection symmetry of the Lagrangian.
Figure 1.1 (b), where $\mu^2 < 0$, is more interesting. Now, the Lagrangian has a mass term of the wrong sign for the field ϕ and contrary to figure 1.1 (a) the potential has two minima:

$$\phi_0 = \pm v\ , \tag{1.19}$$

with $v = \sqrt{-\mu^2/\lambda}$. $\phi = 0$ does not correspond to the energy minimum. Perturbative calculations should involve expansions around the classical minimum $\phi = v$ or $\phi = -v$. Therefore we take

$$\phi(x) = v + \eta(x), \tag{1.20}$$

where $\eta(x)$ represents the quantum fluctuations about the minimum. Substituting (1.20) into the Lagrangian, we obtain

$$\mathcal{L}' = \frac{1}{2}(\partial_\mu \eta)^2 - \lambda v^2\eta^2 - \lambda v\eta^3 - \frac{1}{4}\lambda\eta^4 + \text{const}\ . \tag{1.21}$$

Identifying the first two terms with $\mathcal{L} = \frac{1}{2}(\partial_\mu\phi)(\partial^\mu\phi) - \frac{1}{2}m^2\phi^2$ gives a mass term of the correct sign

$$m_\mu = \sqrt{2\lambda v^2} = \sqrt{-2\mu^2}\ . \tag{1.22}$$

The higher-order terms in η represent the interaction of the field with itself.
Surprisingly, $\mathcal{L}$ and $\mathcal{L}$' are equivalent and at the same time yield different masses. But using $\mathcal{L}$, perturbation around the unstable point $\phi = 0$ would not converge, so the correct way to proceed is

to use $\mathcal{L}$'. The scalar particle therefore has a mass.
This example illustrated how spontaneous symmetry breaking occurs when a symmetry of the Lagrangian is not represented by the vacuum state, defined as the state of lowest energy. The same method of choosing a vacuum from among a degenerated set of vacua and discovering the particle spectra applies equally well to more complicated situations.
At this point a remark about the Goldstone theorem should be made. It states that massless scalars, so called Goldstone bosons, occur whenever a continuous symmetry of a physical system is spontaneously broken. Nevertheless, when proceeding from global to local gauge theory, an appropriate choice of gauge, the unitary gauge, will sort out the spectrum of particles. The Goldstone bosons will disappear from the Lagrangian. The scalar degrees of freedom associated with the Goldstone bosons become the longitudinal polarizations of the massive vector bosons. This way of giving mass to the gauge bosons is called the Higgs mechanism.

1.5 Breaking of $\mathbf{SU(2) \otimes U(1)_Y}$ local gauge symmetry

The minimum model now regarded as "standard" is the result of a long development and many ingenious contributions. Considering the model in its purely leptonic form will exhibit the motivation and the principal features.
For this short overview it suffices to include only the electron and its neutrino, which form a left-handed "weak-isospin" doublet

$$\mathbf{L} \equiv \begin{pmatrix} \nu_e \\ e^- \end{pmatrix}_L \tag{1.23}$$

where left-handed states are

$$\begin{aligned} \nu_L &= \frac{1}{2}(1-\gamma_5)\nu \; , \\ e_L &= \frac{1}{2}(1-\gamma_5)e \end{aligned}$$

Idealizing the neutrino as massless, its right-handed state does not exist. Thus we designate only one right-handed fermion,

$$\mathbf{R} \equiv e_R = \frac{1}{2}(1+\gamma_5)e \; , \tag{1.24}$$

which is a weak-isospin singlet.
To incorporate electromagnetism, a "weak hypercharge", Y, is defined. The Gell-Mann-Nishijima relation

$$Q = I_3 + \frac{1}{2}Y \; , \tag{1.25}$$

where Q is the charge and I_3 the weak isospin projection, leads to the assignments

$$\begin{aligned} Y_L &= -1 \; , \\ Y_R &= -2 \; . \end{aligned}$$

By construction, the weak isospin projection I_3 and the weak hypercharge Y commute:

$$[I_3, Y] = 0 \; . \tag{1.26}$$

Taking the (product) group of transformations generated by I and Y to be the gauge group $SU(2) \otimes U(1)_Y$, it is possible to construct the theory by introducing the gauge bosons

$$\begin{aligned} &b^1_\mu,\ b^2_\mu,\quad b^3_\mu &&\text{, for } \mathrm{SU(2)_L} \\ &\qquad\quad\ \ A_\mu &&\text{, for } \mathrm{U(1)_Y} \end{aligned}$$

The Lagrangian for the theory may be written as

$$\mathcal{L} = \mathcal{L}_{\rm gauge} + \mathcal{L}_{\rm leptons} \;, \tag{1.27}$$

where the kinetic term for the gauge fields is

$$\mathcal{L}_{\rm gauge} = -\frac{1}{4}F^l_{\mu\nu}F^{l\mu\nu} - \frac{1}{4}f_{\mu\nu}f^{\mu\nu} \tag{1.28}$$

and the field-strength tensors are

$$F^l_{\mu\nu} = \partial_\nu b^l_\mu - \partial_\mu b^l_\nu + g\varepsilon_{jkl}b^j_\mu b^k_\nu \tag{1.29}$$

for the $SU(2)_L$ gauge field and

$$f_{\mu\nu} = \partial_\nu A_\mu - \partial_\mu A_\nu \tag{1.30}$$

for the $U(1)_Y$ gauge field. The matter term is

$$\mathcal{L}_{\rm leptons} = \overline{\mathbf{R}}i\gamma^\mu\left(\partial_\mu + \frac{ig'}{2}A_\mu Y\right)\mathbf{R} + \mathbf{L}i\gamma^\mu\left(\partial_\mu + \frac{ig'}{2}A_\mu Y + \frac{ig}{2}\tau\cdot\mathbf{b}_\mu\right)\mathbf{L} \;, \tag{1.31}$$

where g is the coupling constant for the weak-isospin group $SU(2)_L$ and $\frac{g'}{2}$ is the coupling constant for the weak-hypercharge group $U(1)_Y$.
For two obvious reasons, the theory described by this Lagrangian is not satisfying. It contains four massless gauge bosons (b^1, b^2, b^3, A) and the global $SU(2)$ invariance forbids a mass term for the electron.
To modify this in the right way, we introduce a complex doublet of scalar fields

$$\begin{pmatrix} \phi^* \\ \phi^0 \end{pmatrix} \;, \tag{1.32}$$

which transforms as an $SU(2)_L$ doublet and must therefore have weak hypercharge $Y_\phi = +1$, by virtue of the Gell-Mann-Nishijima relation.
We add to the Lagrangian a term

$$\mathcal{L}_{\rm scalar} = (\mathcal{D}^\mu\phi)^\dagger(\mathcal{D}_\mu\phi) - V(\phi^\dagger\phi) \;, \tag{1.33}$$

where the covariant derivative is given by

$$\mathcal{D}_\mu = \partial_\mu + \frac{ig'}{2}A_\mu Y + \frac{ig}{2}\tau\cdot\mathbf{b}_\mu \;, \tag{1.34}$$

and as usual the potential is

$$V(\phi^\dagger\phi) = \mu^2(\phi^\dagger\phi) + |\lambda|(\phi^\dagger\phi)^2 \;. \tag{1.35}$$

An additional interaction term involves Yukawa coupling of the scalars to the fermions,

$$\mathcal{L}_{\rm Yukawa} = -G_e\left[\overline{\mathbf{R}}(\phi^\dagger\mathbf{L}) + (\overline{\mathbf{L}}\phi)\mathbf{R}\right] \quad \text{,with the Fermi constant G}_\text{e} \;, \tag{1.36}$$

which is symmetric under local $SU(2)_L \otimes U(1)_Y$ transformations and is a Lorentz scalar.
Now, we take the case $\mu^2 < 0$ and consider the consequences of spontaneous symmetry breaking.
We choose as the vacuum expectation value of the scalar field

$$\langle\phi\rangle\_0 = \begin{pmatrix} 0 \\ v/\sqrt{2} \end{pmatrix} \quad \text{, with v} = \sqrt{-\mu^2/|\lambda|} \;. \tag{1.37}$$

It breaks both, the $SU(2)_L$ and $U(1)_Y$ symmetry, but preserves the invariance under the $U(1)_{EM}$ symmetry transformation, generated by the electric charge operator. It has to be recalled that a Goldstone boson is associated with every generator of the gauge group that does not leave the vacuum invariant. A generator $\mathcal{G}$ leaves the vacuum invariant if

$$e^{i\alpha\mathcal{G}} \langle\phi\rangle_0 = \langle\phi\rangle_0 \ . \tag{1.38}$$

For an infinitesimal transformation the equation becomes

$$(1 + i\alpha\mathcal{G}) \langle\phi\rangle_0 = \langle\phi\rangle_0 \ , \tag{1.39}$$

so the condition to leave the vacuum invariant is simply

$$\mathcal{G} \langle\phi\rangle_0 = 0 \ . \tag{1.40}$$

For the generators of $SU(2)_L \otimes U(1)_Y$ holds:

$$\begin{aligned}
\tau_1 \langle\phi\rangle_0 &\neq 0 \ , \\
\tau_2 \langle\phi\rangle_0 &\neq 0 \ , \\
\tau_3 \langle\phi\rangle_0 &\neq 0 \ , \\
Y \langle\phi\rangle_0 &\neq 0 \ ,
\end{aligned}$$

but

$$Q \langle\phi\rangle_0 = \frac{1}{2}(\tau_3 + Y) \langle\phi\rangle_0 = 0 \ . \tag{1.41}$$

All the original four generators are broken, but the linear combination corresponding to electric charge is not. Thus, the photon will remain massless while the three other gauge will acquire mass. The expansion of the Lagrangian about the minimum of the Higgs potential ϕ follows by writing

$$\phi = \exp\left(\frac{i\zeta\cdot\tau}{2v}\right) \begin{pmatrix} 0 \\ (v+\eta)/\sqrt{2} \end{pmatrix} \tag{1.42}$$

and transforming to unitary gauge:

$$\begin{aligned}
\phi \to \phi' &= \exp\left(\frac{-i\zeta\cdot\tau}{2v}\right)\phi = \begin{pmatrix} 0 \\ (v+\eta)/\sqrt{2} \end{pmatrix} \ , && (1.43) \\
\tau\cdot\mathbf{b}_\mu &\to \tau\cdot\mathbf{b}'_\mu \ , && (1.44) \\
\mathcal{A}_\mu &\to \mathcal{A}_\mu \ , && (1.45) \\
R &\to R \ , && (1.46) \\
L &\to L' = \exp\left(\frac{-i\zeta\cdot\tau}{2v}\right) L \ . && (1.47)
\end{aligned}$$

It is now possible to rewrite the Lagrangian in terms of the U-gauge fields and investigate the consequences of spontaneous symmetry breaking.
The Yukawa term has become

$$\mathcal{L}_{\text{Yukawa}} = -G_e\frac{v+\eta}{\sqrt{2}}(\overline{e_R}e_L + \overline{e_L}e_R) = \frac{-G_e v}{\sqrt{2}}\overline{e}e - \frac{G_e\eta}{\sqrt{2}}\overline{e}e \ , \tag{1.48}$$

so the electron has acquired a mass

$$m_e = G_e v/\sqrt{2}\,. \tag{1.49}$$

The scalar term in the Lagrangian now is

$$\mathcal{L}_{\text{scalar}} = \frac{1}{2}(\partial^\mu \nu)(\partial_\mu \nu) - \mu^2\nu^2 + \frac{v^2}{8}\left[g^2|b^1_\mu - ib^2_\mu|^2 + (g' A_\mu - g b^3_\mu)^2\right] + ... \tag{1.50}$$

plus interaction terms. The η field has acquired mass $M_H^2 = -2\mu^2 > 0$. It is the physical Higgs boson.
The charged gauge fields can be defined as

$$W^\pm_\mu \equiv \frac{b^1_\mu \mp ib^2_\mu}{\sqrt{2}}\,, \tag{1.51}$$

the term proportional to g^2v^2 is recognizable as a mass term for the charged vector boson:

$$\frac{g^2v^2}{8}(|W^+_\mu|^2 + |W^-_\mu|^2)\,, \tag{1.52}$$

with the charged intermediate boson masses

$$M_{W^\pm} = gv/2\,. \tag{1.53}$$

Finally, defining the orthogonal combinations

$$Z_\mu = \frac{-g' A_\mu + g b^3_\mu}{\sqrt{g^2 + g'^2}} \tag{1.54}$$

and

$$B_\mu = \frac{g A_\mu + g' b^3_\mu}{\sqrt{g^2 + g'^2}}\,, \tag{1.55}$$

also the neutral intermediate boson has acquired a mass

$$M_{Z^0} = \sqrt{g^2 + g'^2}\,v/2 = M_W\sqrt{1 + \frac{g'^2}{g^2}}\,. \tag{1.56}$$

The field B_μ remains a massless gauge boson corresponding to the surviving $\exp[iQ\alpha(x)]$ symmetry. It can be identified as the photon, provided that we set

$$gg'/\sqrt{g^2 + g'^2} = e\,. \tag{1.57}$$

Introducing the weak mixing angle θ_W to parametrize the mixing of the neutral gauge bosons as

$$g' = g\tan\theta_W\,, \tag{1.58}$$

equations (1.54) and (1.55) may be rewritten as

$$Z_\mu = -A_\mu \sin\theta_W + b^3_\mu \cos\theta_W\,, \tag{1.59}$$

$$B_\mu = A_\mu \cos\theta_W + b^3_\mu \sin\theta_W\,. \tag{1.60}$$

Now, at least schematically, the desired particle content has been achieved – plus a massive Higgs scalar.

Neutral Higgs bosons	J^{PC}
H^0	0^{++}
h^0	0^{++}
A^0	0^{+-}
Charged Higgs bosons	J^P
$H^{\pm}$	0^{+}

Table 1.4: Higgs bosons in a two-Higgs-doublet model. Considering the fact that the Standard Model, ignoring fermions, separately conserves C and P, one can assign unique J^{PC} quantum numbers to all the bosons in the theory.

The Higgs scalar's mass depends on λ and v. The gauge boson mass determines v, but λ is a parameter of the scalar potential and up to now, there is no way to calculate λ without finding experimental information about the Higgs spectrum itself.
The interaction terms determine the production mechanisms and decays of the Higgs boson. The self-interaction terms depend on λ but the terms describing the interaction of the Higgs boson with other particles do not depend on λ, so their strength is known.
A good introduction to the Standard Model and gauge theory can be found in [2].

1.6 Beyond the Standard Model

In the minimal model described in the last section, without taking the $U(1)_Y$ symmetry into account, we introduced an $SU(2)$ doublet of complex scalars, $\begin{pmatrix} \phi^* \\ \phi^0 \end{pmatrix}$, with four real fields. Before transforming to U-gauge, there are three massless gauge bosons, $W^{\pm}$ and Z, with two polarization states each. Thus, the total number of independent fields is ten. In U-gauge there are three massive gauge bosons, with a total of nine degrees of freedom, so there will be one physical Higgs boson that should appear as a real particle. In a super-symmetric theory the added symmetry implies that two $SU(2)$ doublets of complex Higgs fields are required to give mass to fermions. There will be eight real scalar fields, plus six massless gauge boson degrees of freedom, fourteen in total. After applying the Higgs mechanism, the same nine states as above are required for the gauge bosons. Five real fields remain, so there should be five spin-zero Higgs fields in the spectrum. Three of the scalar bosons are neutral and the other two are a charged pair. See table 1.4 for the case where C and P are separately conserved.
Any other theory with additional physics beyond the Standard Model will have a spectrum of spin-zero Higgs fields (one or two or more states, $SU(2)$ singlets or doublets or triplets, etc.) that leads to a specific number of spin-zero bosons. Ultimately it will be necessary to determine experimentally the full spectrum of scalar bosons, including their parameters, in order to be confident that any particular theory is correct.
A good description of the two-Higgs-doublet model is given in [3].

Chapter 2

The Higgs Boson at the LHC

In this chapter, the main characteristics of the Standard Model Higgs Boson in Hadron Colliders, such as LHC, are discussed. In the first two sections, an overview of the production and decay processes will be given. Section three will offer a more detailed look at the channel $H \rightarrow 4\mu$. In the last section, the possibility of non Standard Model Higgs Bosons in this channel will be considered and observables to differentiate between these models will be introduced.

2.1 Higgs Boson Production at the LHC

The Higgs Boson's couplings are proportional to the masses of the particles that couples to it. However, the constituents of the protons (predominately gluons) are essentially massless. Higgs production has to be mediated by " third-party particles" that couple the Higgs boson to the gluons and light quarks. The four most important production modes are:

- gluon fusion (via top quark loop)
- associated Higgs production with weak gauge bosons (Higgs strahlung)
- associated Higgs production with a top quark pair ($t\bar{t}H$)
- weak gauge boson fusion

They will be discussed in the following. Their cross sections versus the Higgs boson mass at the LHC can be seen in figure 2.1. More information can be found in [7].

Gluon Fusion: Over the whole mass range gluon fusion turns out to be the dominating Higgs production mode. As gluons are massless the coupling between the gluons and the Higgs boson is mediated by a top quark loop (see figure 2.2). The high gluon luminosity at the LHC compensates for the loop suppression and lets this mode exceed all the other channels. However, the leading order prediction for the cross section of this channel suffers from large uncertainties. QCD corrections are enhanced, since the leading order process is pure color singlet production, which is no longer true at higher orders of corrections, where real gluon and quark radiation has to be included.
Evaluation of QCD corrections is challenging due to the fact that the leading order is given by massive one-loop triangle diagrams. It has been calculated in next-to-leading order (NLO) [8] and turned out to be almost 100% leading to a K-Factor [1] of about 2. For the Higgs production

[1] $K = \frac{\sigma_{nlo}}{\sigma_{lo}}$

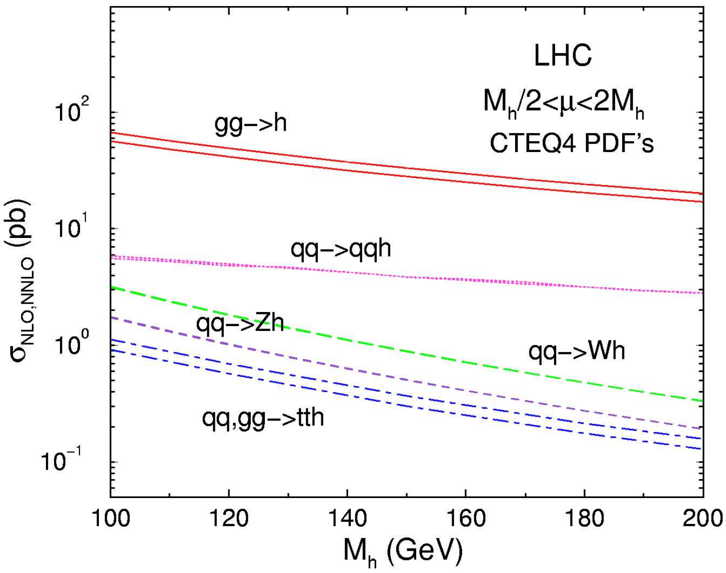

Figure 2.1: Higgs production cross section at 14 TeV, including known higher orders and theoretical uncertainties [7]

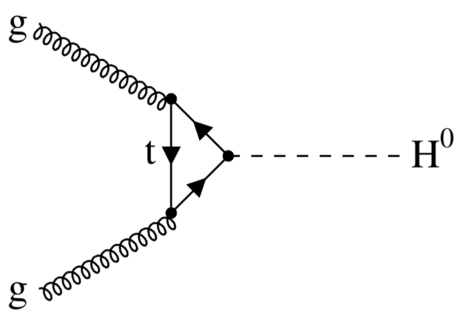

Figure 2.2: Higgs boson Production via gluon fusion mediated by a top-quark loop

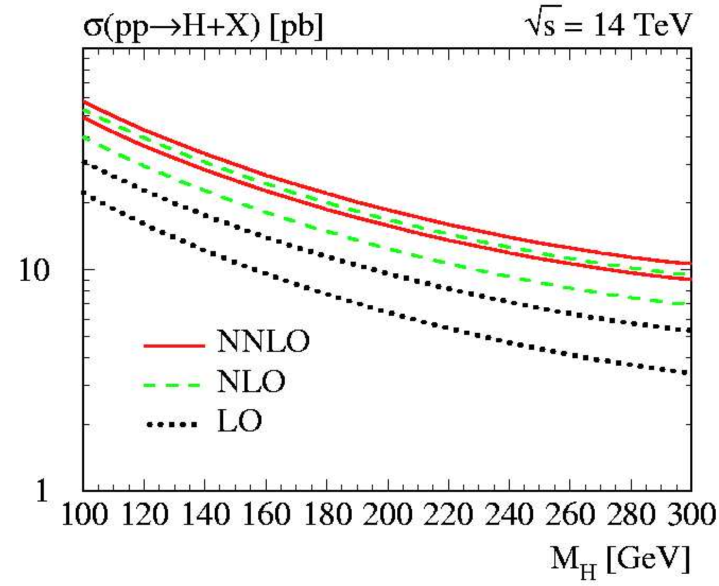

Figure 2.3: Total cross section for Higgs production in gluon fusion at 14 TeV in leading, next-to-leading and next-to-next-to-leading order [7].

rate at next-to-next-to-leading order (NNLO), one has to include the virtual two-loop corrections, radiation of one quark or gluon up to the one-loop level, and radiation of two quarks or gluons up to tree level. The resulting corrections are shown in figure 2.3.

Higgs Strahlung: The leading order Feynman diagram of the Higgs strahlung process is shown in figure 2.4. The Higgs boson is produced in association with a weak gauge boson. The QCD corrections can be derived from the Drell-Yan process and give an increase to the LO prediction. The cross section is almost one order of magnitude smaller than in the case of gluon fusion. Higgs Strahlung can be distinguished from its background through the tagging of the W- and Z-decay products, which is useful in lower mass regions where the Higgs boson mainly decays into two b-quarks.

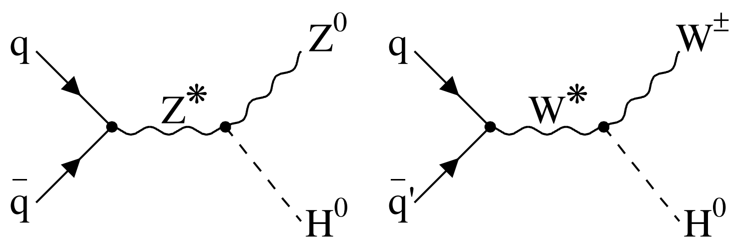

Figure 2.4: Higgs strahlung at leading order. Z^0 and $W^{\pm}$ are produced off-shell and can therefore radiate a Higgs boson.

Vector Boson Fusion: This channel has the second largest rate at the LHC (see figure 2.1). The corresponding Feynman diagram is shown in figure 2.5. QCD corrections for vector boson fusion are known up to NLO and are about 10%. It can be used for Higgs measurements that go beyond discovery and mass determination, i.e. determination of the CP properties and, in combination with gluon fusion and associated $t\bar{t}H$ production, measurement of the ratios of Higgs coupling.

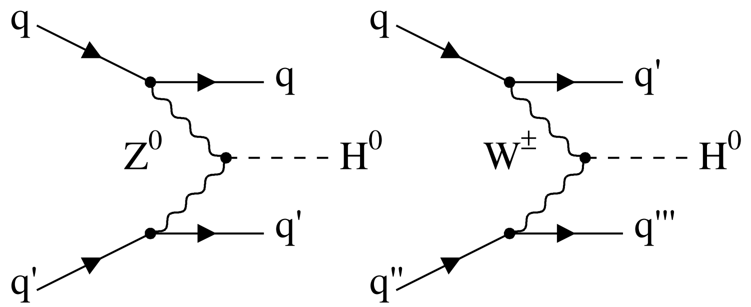

Figure 2.5: Vector boson fusion process at leading order. The Z^0 fusion leaves the quark flavors unchanged, the $W^\pm$ changes the quark flavors from down to up type or vice versa.

Associated $\mathbf{t\bar{t}H}$ Production: This mode has a remarkable signature: four b quarks in association with two W bosons. The leading order Feynman diagrams are shown in figure 2.6. Because of its tagging potential, this signature makes $t\bar{t}H$ production attractive even though its cross section is rather small.The next-to-leading order K-Factor for LHC was determined to be $K \approx 1.3$.

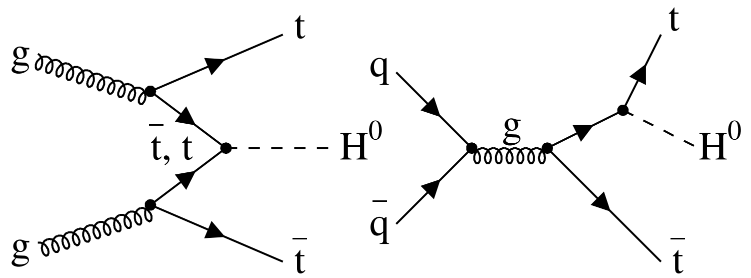

Figure 2.6: Associated Higgs production with a top quark pair at leading order.

2.2 Higgs Boson Decay Modes

The Standard Model predicts that the coupling strength for Higgs decays is proportional to the mass of the decay products, so the Higgs boson prefers to decay into the heaviest particles kinematically possible. The decay into massless particles, i.e. gluons and photons, is mediated by " third-party particles", mainly via top-loops (see figure 2.7). As can be seen in figure 2.8, the branching ratios change dramatically across the possible range of the Higgs mass, making it necessary to have different strategies for the Higgs identification depending on its mass. To discuss the Higgs boson decay modes it is convenient to divide the mass sector into two ranges: The "low mass" range $m_{\text{Higgs}} \lesssim 130$ GeV and the "high mass" range $m_{\text{Higgs}} \gtrsim 130$ GeV .
In the "low mass" range, the main decay mode is by far the decay into a $b\bar{b}$ pair with a ratio $\sim 90\%$ followed by the decays into $c\bar{c}$ and $\tau\bar{\tau}$ (see figure 2.9) with a ratio of $\sim 5\%$. The Higgs decay into gluons at a level of $\sim 5\%$ for m_{Higgs} =120 GeV is also of significance in this mass region.
In the "high mass" range, the Higgs boson decays mainly into WW and ZZ bosons (see figure 2.10), one of the gauge bosons being virtual below the threshold. Above the ZZ threshold, the

Higgs boson decays almost exclusively into these channels, with the branching ratios of WW and ZZ being $2/3$ and $1/3$ respectively. The opening of the $t\bar{t}$ channel does not contribute significantly, since for large Higgs masses, the width of $t\bar{t}$ decays rises only linearly with m_{Higgs} while the width to WW and ZZ grows with m^3_{Higgs}.
Figure 2.11 shows the Standard Model Higgs boson decay width. It becomes rapidly wider for masses larger than 130 GeV, reaching 1 GeV at the ZZ threshold. For masses $m_{\text{Higgs}} \gtrsim$ 700 GeV the Higgs bosons decay width becomes comparable to its mass.
A good summary on this subject can be found in [9]

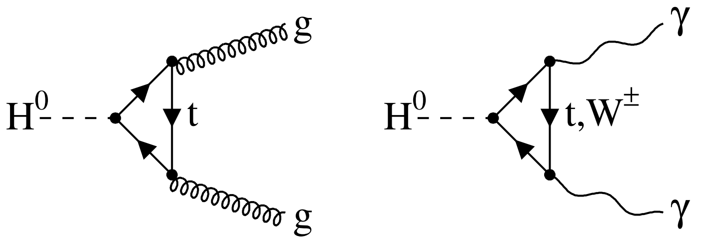

Figure 2.7: Higgs decay to massless particles at LO via top-loops

2.3 The “Gold Plated” Channel H $\rightarrow 4\mu$

The decay channel $H \rightarrow ZZ \rightarrow 4\mu$ (see figure 2.12) is characterised by several qualities. The main reasons, why this decay channel often is called the “gold plated” channel are related to its final state consisting of four isolated muons:

- Chances to trigger the events are outstanding. The fact that it is easy to detect muons and to distinguish them from other particles makes them perfect for triggering.
- The channel has a manageable background. Only a small number of processes have four isolated muons in their final states.
- The kinematics of this channel are completely reconstructible. Muons do not suffer from bremsstrahlung or electromagnetic showers.
- The channel $H \rightarrow ZZ \rightarrow 4\mu$ has a noticeable branching ratio across almost the whole interesting mass range. It opens for masses $m_{\text{Higgs}} \gtrsim$ 100 GeV as a decay into an on-shell Z and an off-shell Z^* boson with an significant ratio for $m_{\text{Higgs}} \gtrsim$ 120 GeV.

Background processes There are not many background processes with a signature similar to $H \rightarrow 4\mu$. The three most relevant ones will be discussed in the following:

- **ZZ Production:** ZZ Production is the most important background. Since it has the same signature as $H \rightarrow ZZ \rightarrow 4\mu$, it is hard to suppress. After radiation of a Z boson a quark anti-quark pair annihilate to produce a second Z boson (see figure 2.13). Since the only difference to the signal channel can be found in the production process of the Z bosons, this background process almost perfectly mimics the signal except for the reconstructed Higgs boson mass.

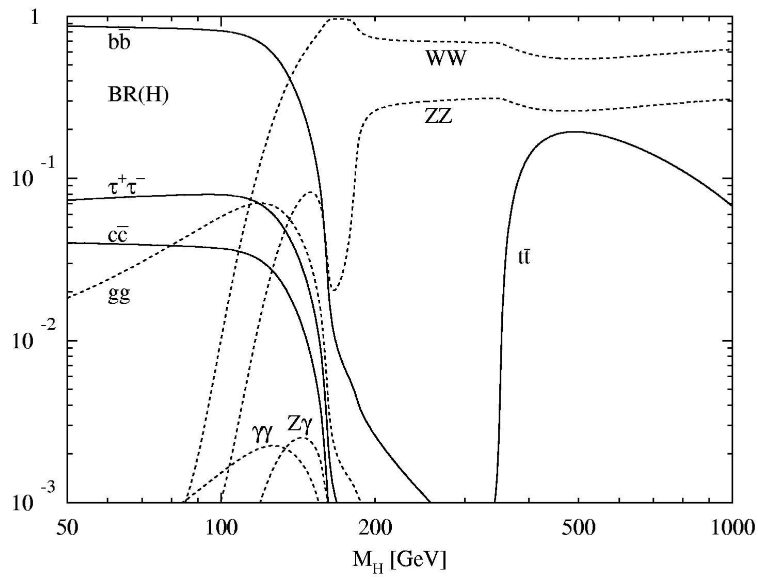

Figure 2.8: Branching ratios of the main decay channels of the Standard Model Higgs boson [10].

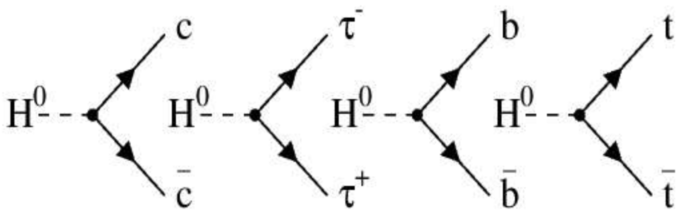

Figure 2.9: Higgs decay to fermion pairs at LO. The Higgs coupling is proportional to the fermion mass, which increases from left to right

- **$t\bar{t}$ Production:** Production of the $t\bar{t}$ pair is possible via quark anti-quark annihilation and gluon fusion. This results in a state with two W bosons and two b quarks. The W boson decays into a muon and the according neutrino with a ratio of 10.47%. Furthermore, there is a probability of about 10% that a muon exists in a b quark jet. Thus, one can get a final state with four muons (see figure 2.14). This background can be easily surpressed mainly because there are non-isolated muons in the final state and reconstruction of a Z boson often fails.

- **$Zb\bar{b}$ Production:** The Feynman diagram of this channel can be seen in figure 2.15. The produced Z boson can decay into two muons and again there are two b quark jets that may contain muons. The final state consists of non-isolated muons, a fact that helps to suppress this background. However, since there is a Z boson in the decay, Z reconstruction will be positive.

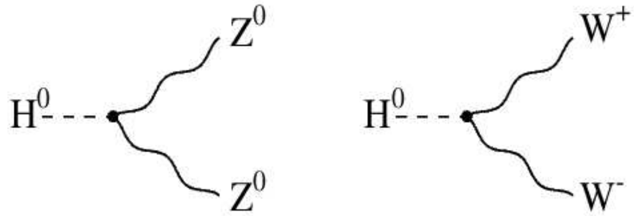

Figure 2.10: Higgs decay to vector bosons Z^0 and $W^{\pm}$ in leading order

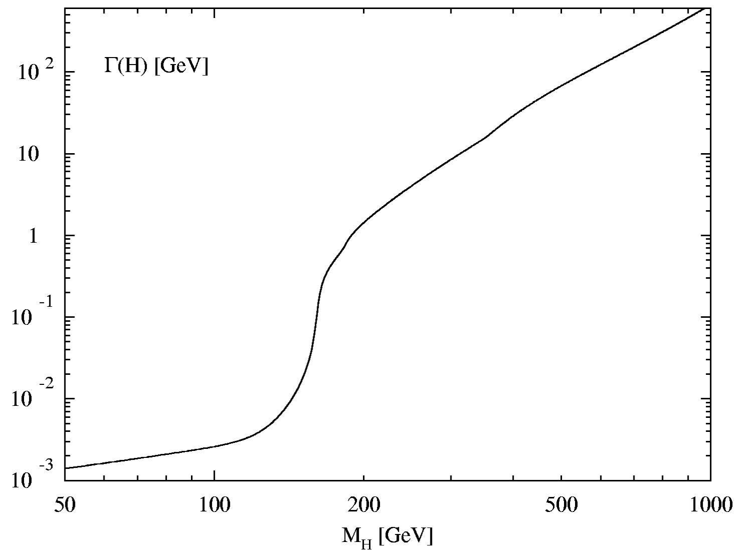

Figure 2.11: Total decay width of the Standard Model Higgs boson [10]

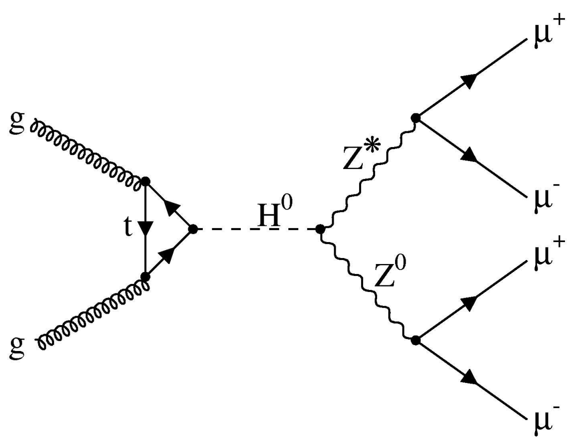

Figure 2.12: Feynman diagram of the Higgs decay $H \rightarrow ZZ \rightarrow 4\mu$, the "Gold Plated" channel.

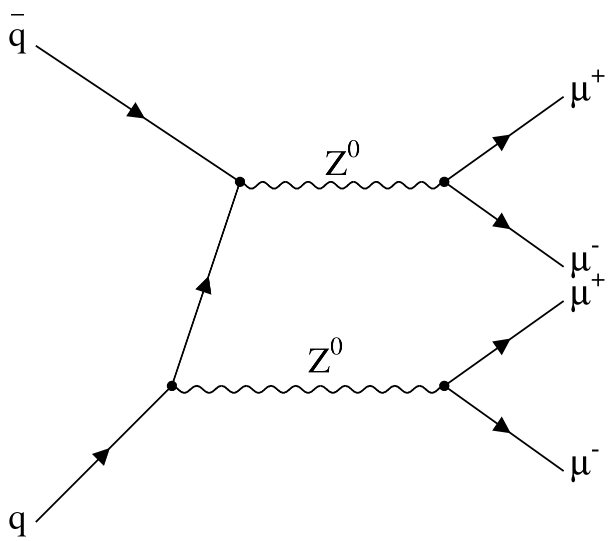

Figure 2.13: ZZ background: The two Z bosons decay into two muons each, resulting in an 'irreducible' background

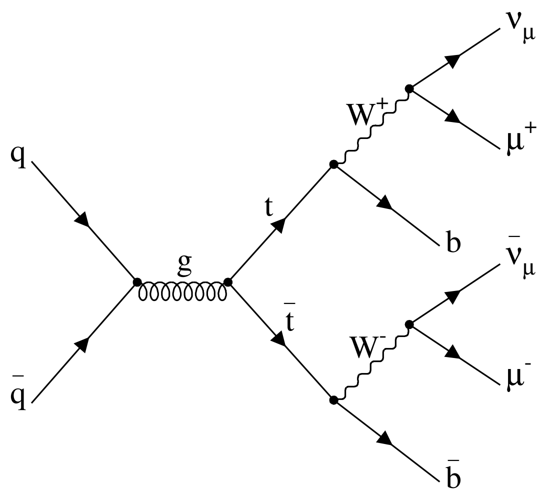

Figure 2.14: $t\bar{t}$ background: The t quark decays almost exclusively into a W boson and a b quark. The W boson decaying into a muon and muon neutrino and the b quark jets containing muons, the four muon final state results.

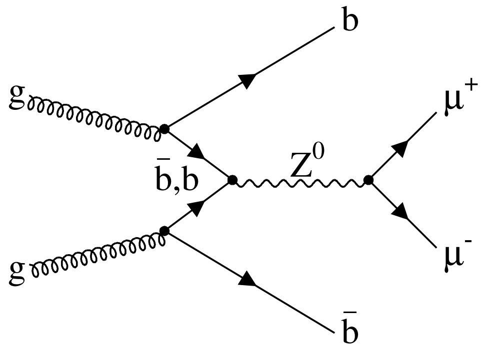

Figure 2.15: $Zb\bar{b}$ background: The Z boson decays into two muons the b quark jets contain two muons on their part to build a four muon final state.

2.4 Determining Quantum Numbers of the Higgs Boson

Once the Higgs boson will be discovered and its mass will be measured it is important to determine its quantum numbers. The Standard Model predicts a $J^{PC} = 0^{++}$ field. In extended gauge models, e.g. two-doublet Higgs models, other quantum numbers are possible. To underline the uniqueness of the SM prediction, it is interesting to confront the Standard Model Higgs with pseudo-scalar states (0^{-+}). These can have radiatively induced couplings to two Z bosons of the form $\frac{D}{m_Z^2}\varepsilon_{\mu\nu\rho\sigma}\varepsilon_1^\mu\varepsilon_2^\nu p_1^\rho p_2^\sigma$.[1] The structure of this coupling can be tested making use of the angular distribution of the final state particles, in the case of $H \to ZZ \to 4\mu$ the correlation between the $\mu_1^+\mu_1^-$ and $\mu_2^+\mu_2^-$ decay planes.
A detailed examination of this subject can be found in [6, 5, 22, 4]

2.4.1 The Helicity Structure of the H $\to$ ZZ Amplitude

Generally, the decay $H \to ZZ$ produces a system of two Z bosons in the helicity state

$$|ZZ\rangle = c_+|++\rangle + c_-|--\rangle + c_0|00\rangle \, . \tag{2.1}$$

If H is scalar, the two Z polarisations will be parallel; if H is pseudo-scalar, the two Z polarisations will be perpendicular. The effective interaction Lagrangian for the ZZH vertex can be written as

$$\mathcal{L}_{HZZ} = \frac{1}{2}g_H H\left[BZ^\nu Z_\nu + \frac{1}{4}DM_H^{-2}\varepsilon_{\mu\nu\rho\sigma}Z^{\mu\nu}Z^{\rho\sigma}\right] ,$$

where $g_H = (g_2 M_Z/\cos\theta_W)$, $Z^{\mu\nu}$ is the field strength of the Z boson and B and D are dimensionless form factors. For the Standard Model Higgs boson holds: $D = 0$ and $B = 1$. The D term is a P-wave coupling, odd under parity and even under charge conjugation while the B term is an S-wave coupling, even under parity and charge conjugation. Simultaneous presence of D and B is CP violating.

[1]Here, (ε_1, p_1) and (ε_2, p_2) denote the polarisation vectors and momenta of the Z bosons.

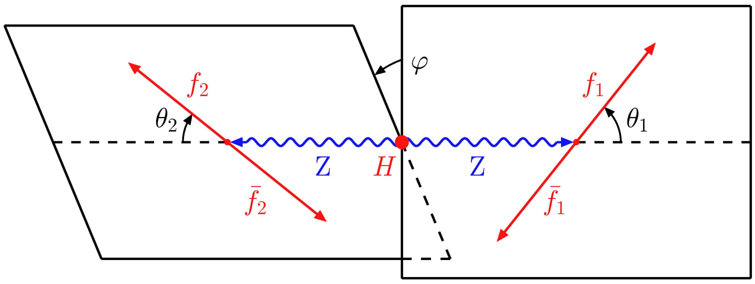

Figure 2.16: The definition of polar angles, θ_1 and θ_2, and the azimuthal angle, φ for the decay $H \to ZZ \to f_1\overline{f_1}f_2\overline{f_2}$ in the rest frame of the Higgs boson.[6]

In momentum space, the effective vertices give rise to the covariant amplitude

$$iM_{H\to Z(p_1,\varepsilon_1),Z(p_2,\varepsilon_2)} = ig_H\left[B\varepsilon_1\cdot\varepsilon_2 + (D/M_H^2)\epsilon_{\mu\nu\rho\sigma}\varepsilon_1^\mu\varepsilon_2^\nu p_1^\rho p_2^\sigma\right] \tag{2.2}$$

and the following characteristic helicity wave-functions:

$$\begin{aligned} Bg_{\mu\nu}\varepsilon_1^\mu\varepsilon_2^\nu &\quad : \quad |++\rangle + |--\rangle + \frac{1+\beta^2}{1-\beta^2}|00\rangle \\ \frac{D}{m_Z^2}\varepsilon_{\mu\nu\rho\sigma}p_1^\rho p_2^\sigma\varepsilon_1^\mu\varepsilon_2^\nu &\quad : \quad |++\rangle - |--\rangle\,. \end{aligned}$$

The Standard Model Higgs coupling generates a transversely polarised state $|++\rangle+|--\rangle$ mixed with a specific amount of longitudinal polarisation $|00\rangle$. The longitudinal component dominates in the high energy limit $\beta \to 1$. In comparison, a pseudo-scalar Higgs boson decays into a transversely polarised state $|++\rangle - |--\rangle$.

2.4.2 Characteristic Observables

Since distributions in the $Z \to f\overline{f}$ decay are different for longitudinally and transversally polarised Z bosons, angular distributions of the final-state fermions in the decay $H \to ZZ \to f_1\overline{f_1}f_2\overline{f_2}$ are characteristic observables for measuring spin and parity of the Higgs boson. The polar angles of the fermions f_1, f_2 in the rest frame of the Z bosons are denoted by θ_1 and θ_2, and the azimuthal angle between the planes of the fermion pairs by φ (see figure 2.16).

The differential distribution in $\cos\theta_1, \cos\theta_2$ is predicted by the Standard Model to be

$$\frac{d\Gamma_H}{d\cos\theta_1 d\cos\theta_2} \sim \sin^2\theta_1\sin^2\theta_2 + \frac{1}{2\gamma^4(1+\beta^2)^2} \tag{2.3}$$

$$\times \left[(1+\cos^2\theta_1)(1+\cos^2\theta_2) + 4\eta_1\eta_2\cos\theta_1\cos\theta_2\right] \tag{2.4}$$

and with respect to the azimuthal angle φ

$$\frac{d\Gamma_H}{d\varphi} \sim 1 - \eta_1\eta_2\frac{1}{2}\left(\frac{3\pi}{4}\right)^2\frac{\gamma^2(1+\beta^2)}{\gamma^4(1+\beta^2)^2+2}\cos\varphi + \frac{1}{2}\frac{1}{\gamma^4(1+\beta^2)^2+2}\cos(2\varphi) \tag{2.5}$$

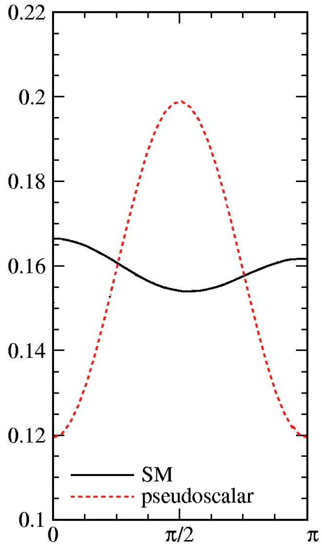

Figure 2.17: Theoretical distribution of φ for a Standard Model Higgs boson (black) and a pseudo-scalar Higgs boson (dashed red).[6]

where $\eta_i = 2v_i a_i/(v_i^2 + a_i^2)$ is the polarisation degree [2] and $\gamma = 1/\sqrt{1-\beta^2}$. For large Higgs masses, the double differential distribution approaches $\sim \sin^2\theta_1 \sin^2\theta_2$. This reflects the asymptotic longitudinal Z polarisation. The φ dependence disappears in this limit.
The two distributions for the Standard Model Higgs boson are now confronted with the decay of a pseudo-scalar Higgs boson. Only transverse Z polarisation contributes to the decay amplitude. The resulting angular distribution is independent of the Higgs mass:

$$\frac{d\Gamma_H}{d\cos\theta_1 d\cos\theta_2} \sim (1+\cos^2\theta_1)(1+\cos^2\theta_2) + 4\eta_1\eta_2\cos\theta_1\cos\theta_2 \tag{2.6}$$

and with respect to φ:

$$\frac{d\Gamma_H}{d\varphi} \sim 1 - \frac{1}{4}\cos(2\varphi)\ . \tag{2.7}$$

The distributions (2.6) and (2.7) are distinctly different from the ones predicted by the Standard Model. For the case of $m_{Higgs} = 200$ GeV the distributions with respect to φ are compared in figure 2.17. The cases of a scalar Standard Model Higgs boson and a pseudo-scalar Higgs boson are both implemented in the event generator PYTHIA 6.215 (see section 5.1.1). In this study the distribution of the angle φ will be utilised to determine the Higgs bosons CP eigenvalue.

It should be remarked that, naively, one may simply take the CP-odd correlation $O_{odd} = (\overrightarrow{p_{\mu_1^-}} \times \overrightarrow{p_{\mu_1^+}}) \cdot \overrightarrow{p_{\mu_2^-}}$ as an observable for the CP eigenvalue. However, the expectation value of this observable is proportional to $c_V c_A$, where $c_V = \frac{1}{2}(c_L + c_R)$ and $c_A = \frac{1}{2}(-c_L + c_R)$ are the vector and axial vector couplings of the Z boson. Since vector coupling of the Z boson to charged leptons is relatively small in the Standard Model, the proposed observable is hardly measurable.

[2] $v_i = 2I_{3i} - 4e_i \sin^2\theta_W$ and $a_i = 2I_{3i}$ are the electroweak charges of the fermion f_i

Chapter 3

The CMS Detector at the LHC

The CMS[1] detector will be one of the multipurpose detectors being operated at the LHC[2] at CERN[3]. In this chapter, an overview of the LHC and the CMS Detector with its subsystems will be given.

3.1 The Large Hadron Collider

The pp-collider LHC at the international research center CERN is the only approved accelerator project in particle physics which will extend the energy available for hard constituent collisions by an order of magnitude compared to current colliders.
The search for Higgs bosons in the mass range from 90 GeV up to 1 TeV is the major physics goal at the LHC. Its discovery would be the experimental evidence for the mechanism of spontaneous symmetry breaking which explains how symmetry requirements can be fulfilled in a world with massive particles. Furthermore, the LHC covers an energy scale which will probe promising theoretical concepts that offers solutions to open problems in the Standard Model. Other interesting aspects of LHC are the high production rate of heavy quarks and the possibility of precision measurements, e.g. of the W boson mass.
The LHC is currently being installed in the former LEP[4] tunnel at CERN with a circumference of 27 km and is supposed to go on line in 2007. In the pp collision mode the center of mass energy will be $\sqrt{s} = 14$ TeV with the design luminosities $\mathcal{L} = 10^{34}\,\mathrm{cm}^{-2}s^{-1}$ for high luminosity and $\mathcal{L} = 2 \cdot 10^{33}\,\mathrm{cm}^{-2}s^{-1}$ for low luminosity. The two opposite beam-lines will be filled with 2835 bunches of about 10^{11} particles. Bunch crossings will occur every 25 ns, yielding about 10^9 interactions per second.
At four interaction points, particle detectors are placed. The ALICE[5] and LHCb[6] detectors are designed for heavy ion and b-physics. ATLAS[7] and CMS are two complementary general purpose detectors which are planned to explore new physics and in particular probe the electroweak symmetry breaking. Since it is not known exactly how symmetry breaking occurs, and one should always stay open to unexpected phenomena, these two detectors must have a broad array of capabilities.

[1] Compact Muon Solenoid
[2] Large Hadron Collider
[3] European Organization for Nuclear Research in Geneva, Switzerland
[4] Large Electron Positron collider
[5] A Large Ion underlineCollider Experiment
[6] Large Hadron Collider beauty experiment
[7] A Toroidal LHC ApparatuS

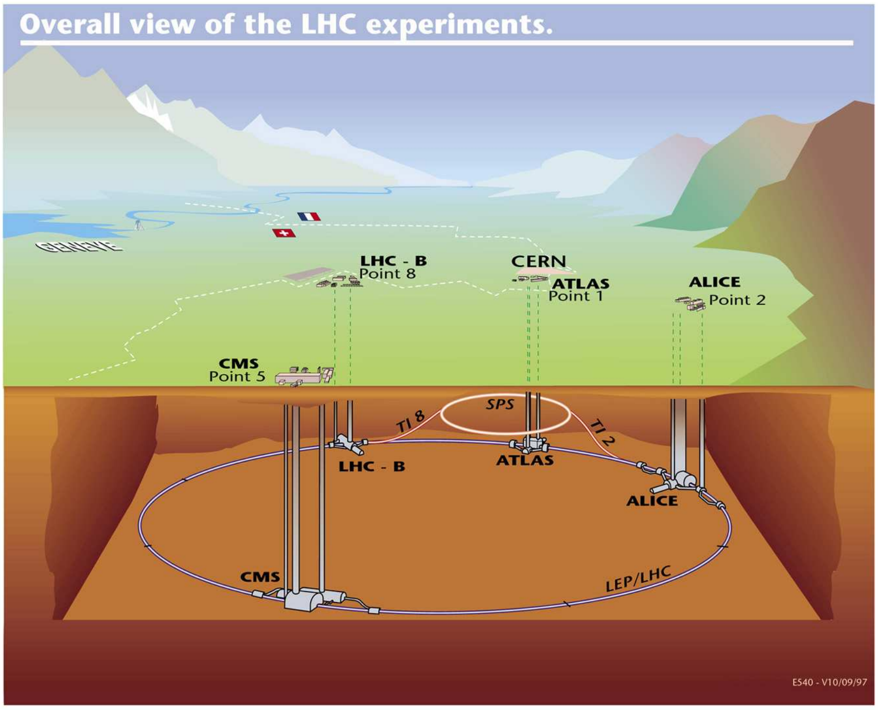

Figure 3.1: Overview of the LHC with its four detectors ALICE, ATLAS, CMS and LHCb.

3.2 The CMS Detector

More than 140 institutions from more than 30 different countries participate in the CMS collaboration. In its overall dimensions the CMS detector has a diameter of 15 m and a length of 21.6 m. A 13 m long superconducting solenoid with an inner bore of 2.95 m provides an axial magnetic field of 4 Tesla. The central tracker and the electromagnetic and hadron calorimeters are situated within the solenoid. The four muon stations of the barrel and the endcaps are embedded in the return yoke iron. Here the return field has a strength of about 1.8 Tesla.
The main components of the CMS detector will be described in the following sections.

3.2.1 The Tracking System:

The requirements for the tracker of CMS are quite challenging. It must combine efficient pattern recognition, fast response (to avoid pile up) and good spatial resolution. In addition, it has to be robust in order to guarantee long term functioning in a region where radiation levels are high. CMS uses an all-silicon approach for this challenge.

Pixel Detectors: The pixel detector system consists of two concentric barrel layers at radii of 4 and 7 cm for low luminosity and at 7 and 10 cm for high luminosity. Two “turbine blade” disks of pixel sensors at the endcaps complete the system. With the sensors having a pixel size of $150 \times 150\,\mu\mathrm{m}^2$, a total of 50×10^6 channels are envisaged. The spatial resolutions are about $10\,\mu\mathrm{m}$ and $14\,\mu\mathrm{m}$ in the ϕ and z coordinates respectively.

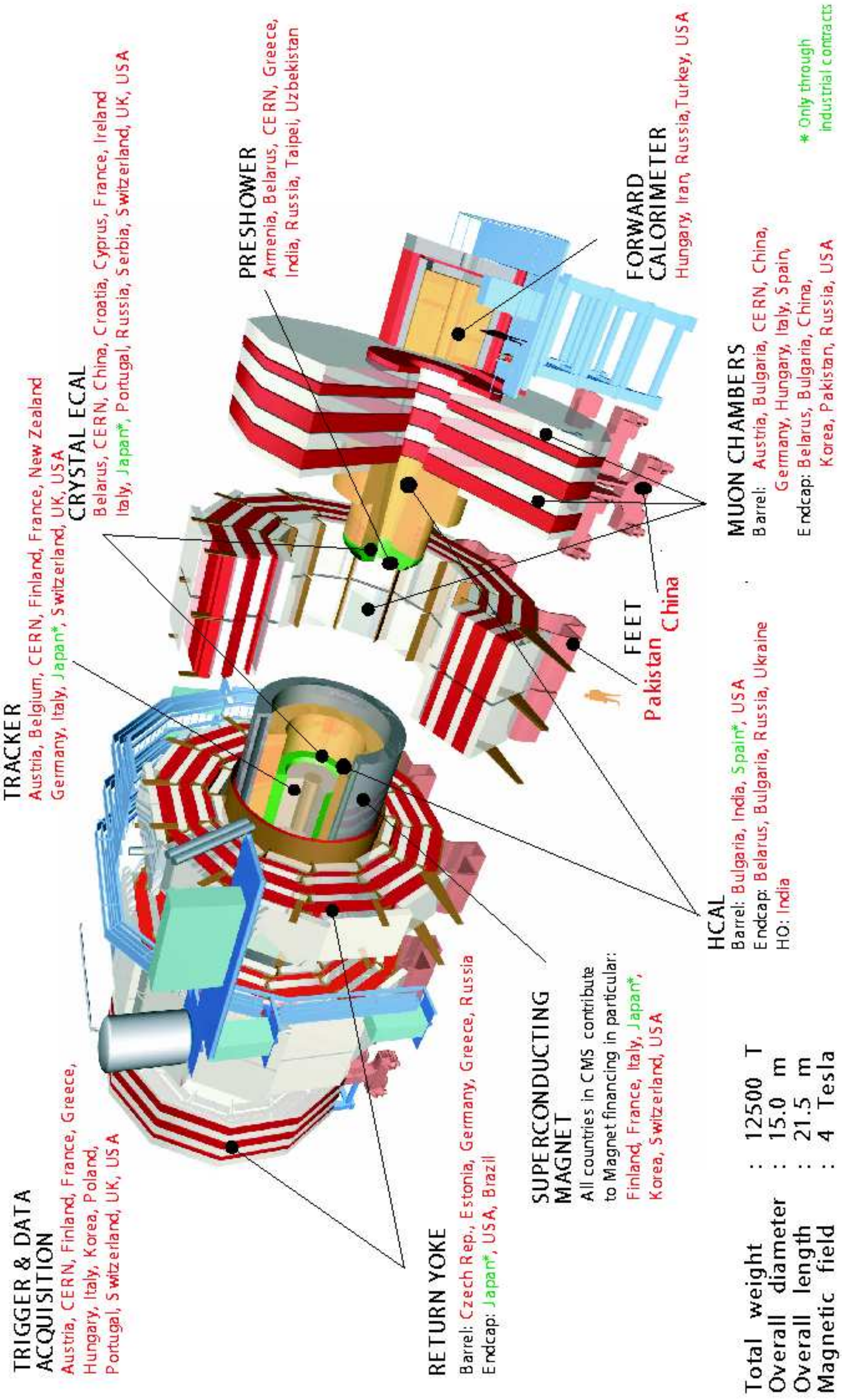

Figure 3.2: Overview of the CMS detector.

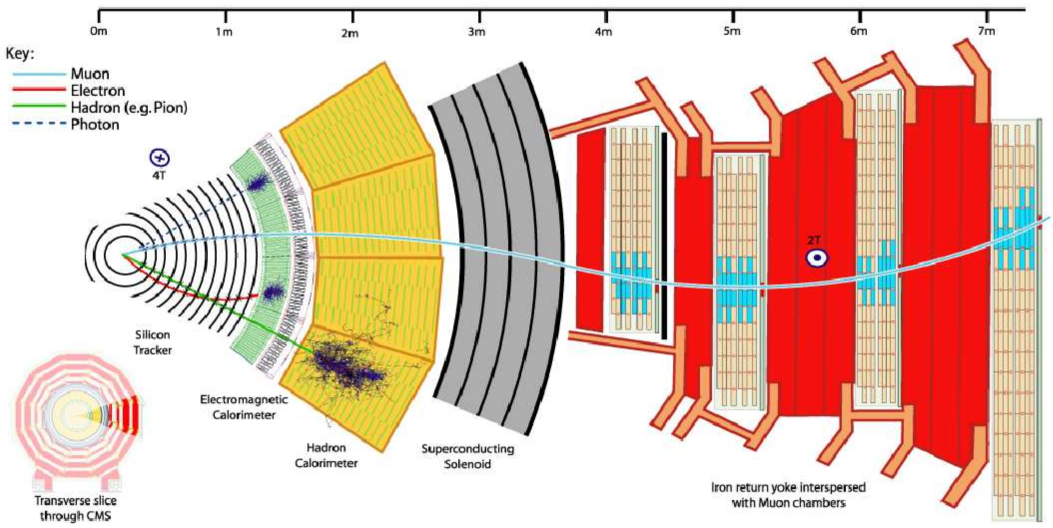

Figure 3.3: Different particles and their tracks in the CMS detector: Electrons deposit their energy in the ECAL, hadrons in the HCAL while muons pass through the calorimeters and are detected in the muon system.

Silicon Strip Detectors: The silicon strip detectors consist of five single-sided and five stereo layers in the barrel. On each side, there are three mini-endcap and nine large endcap disks. Totally, there are 7,888 single-sided and 4,032 double-sided modules.

3.2.2 Calorimeters of CMS:

Calorimeters use the total-absorption method to determine the energy and position coordinates of incoming particles. The particles interact with the material of the calorimeter, producing secondary particles, leading to a shower of particles which generates an electric pulse proportional to the particles total energy. There are two types of calorimeters: photons, electrons and positrons lose their energy in the electromagnetic calorimeter (ECAL) through interactions with the electrons of the calorimeter material. Hadrons, being more penetrating, pass through the ECAL without losing much energy. They are detected in the hadronic calorimeter (HCAL), where they interact with the atomic nuclei of the typically heavy material.

ECAL of CMS: The requirements for the electromagnetic calorimeter of CMS are largely inspired by the benchmark decay of a Higgs boson into two photons, in order to achieve a good mass resolution. CMS has opted for a homogeneous calorimeter made of lead tungstate crystals ($PbWO_4$), whose high density of 8.28 g/cm^3 and short radiation length of 0.89 cm lead to a compact calorimeter. The ECAL barrel will contain 61,200 crystals, assembled in alveolar structures, while the endcaps will consist of 21,523 crystals in total, assembled in 4 D's.

HCAL of CMS: The hadron calorimeter system consists of 5 cm thick copper alloy absorber plates interleaved with 4 mm thick scintillator tiles read out by wavelength shifting fibers. To extend the hermeticity of the HCAL at large rapidities[8] ($3.0 < |\eta| < 5.0$), very forward calorimeters are situated 6 m downstream of the endcap calorimeters. They use quartz fibers as the active medium, embedded in a copper absorber matrix.

3.2.3 The CMS Muon System:

In both, barrel and endcaps, the muon system relies on complementary detectors to fulfill its goal: a dedicated trigger device, being fast and yielding coarse position information, and tracking detectors with excellent position resolution. Resistive Plate Chambers (RPC) are used as trigger detectors and cover the pseudo-rapidity range up to $|\eta| = 2.1$. In the barrel region ($0 \leq |\eta| \leq 1.3$), Drift Tubes (DT) provide the muon tracking and in the endcap regions ($1.3 \leq |\eta| \leq 2.4$), Cathode Strip Chambers (CSC) fulfill this task. In standalone muon identification, these detectors also generate a trigger with different sensitivity to background as compared to the RPC system.
Everywhere the detectors are organised in four stations interleaved with the iron return yoke plates (see figure 3.4). One or two layers of RPC's are embedded in each muon station. In the barrel region drift tubes provide a R, ϕ resolution of about $100\mu\mathrm{m}$ and a z coordinate resolution of about $150\mu\mathrm{m}$. In the endcaps, since a highly segmented and fast detector system is required, CSC's are used. They provide a R, ϕ resolution of about $75\mu\mathrm{m}$. This muon system yields a momentum resolution of $\sim 10\%$ for muons with a p_T of 100 GeV. When combined with the central tracker this momentum resolution becomes $\sim 2\%$.

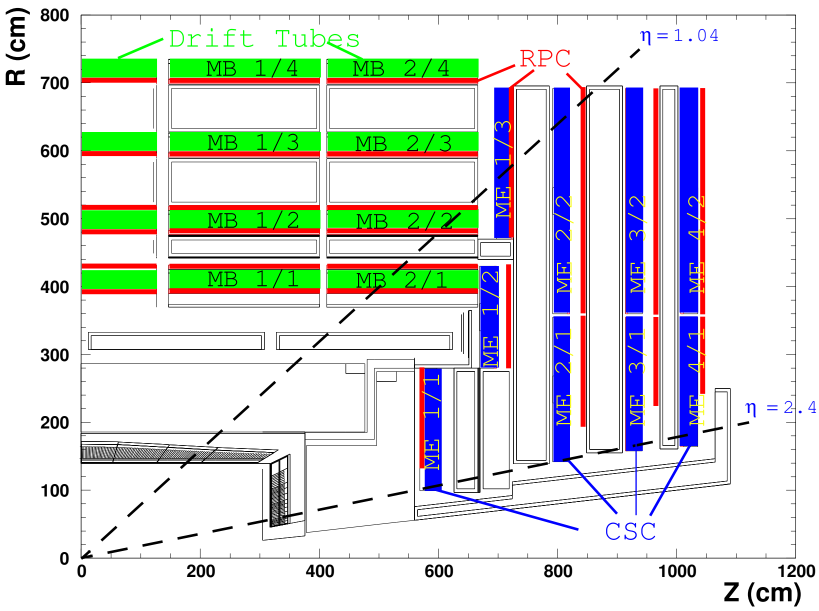

Figure 3.4: In the profile of the CMS muon system one can see the Resistive Plate Chambers (RPC), the Cathode Strip Chambers (CSC) in the endcap region and the Drift Tubes (DT) in the barrel.

3.2.4 Trigger and Data Acquisition

The LHC run at high luminosity will yield about 10^9 interactions per second, presenting a tough challenge to the CMS trigger and data acquisition system. Out of the $40 \cdot 10^6$ crossings per second

[8]definition of the pseudo rapidity $\eta = -\ln(\tan(\theta/2))$

only about 100 can be recorded. The suppression will be carried out by a 3-level trigger system (see figure 3.5).
The level-1 trigger is designed to reduce the rate to about 100 kHz. Since the time available for processing is about 2μs, the level-1 trigger is a pure hardware trigger. It utilises only data from the RPC's in the muon system and coarsely segmented calorimeter data. The full data is kept in the memory pipelines of the front-end electronics until the event is accepted or rejected. If accepted the data is passed to the High Level Trigger (HLT) where the event rate is reduced to 100 Hz. The HLT consists of processor farms and has a total processing time of about 1 s. It can be divided into a level-2 and a level-3 trigger. The level-2 trigger exploits the full calorimeter and muon chamber information while the level-3 trigger does the full event reconstruction.

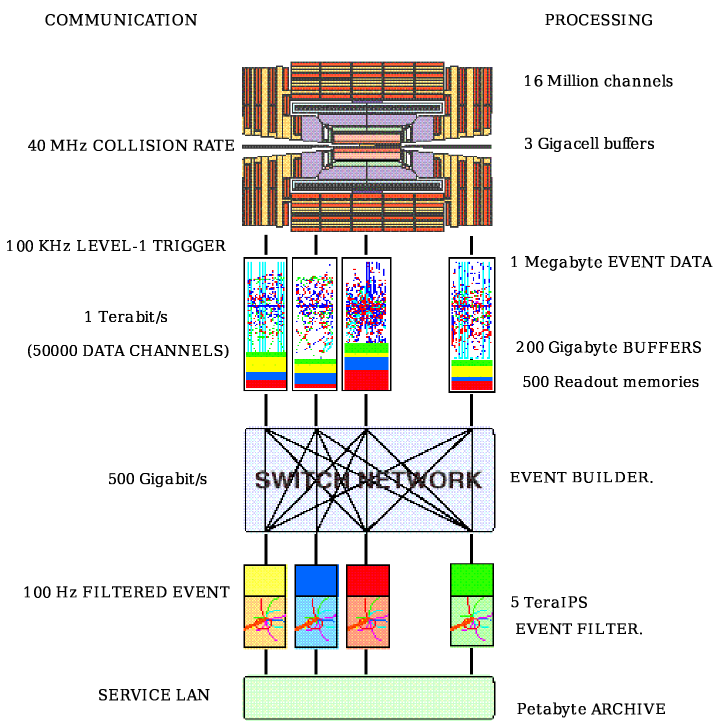

Figure 3.5: Overview of the CMS trigger and data acquisition. The raw data is filtered by the level-1 trigger to rate of about 100 kHz. The High Level Trigger (HLT) reduces the data to 100 Hz.

Chapter 4

Production and Analysis Tools

One of the main challenges of this study is the production and analysis of tens of thousands of events in order to achieve enough statistics. A full detector simulation and reconstruction of the events has been carried out. This consumes much processor time and disk space (see figure 5.1). Another problem beside this requirement on computing power is that a combination of different software packages is needed. Since many of the packages are under development and sometimes only preliminary versions are available, the interaction is not always trivial.
In this chapter, a brief description of the used software is given. All of it is part of the CMS software environment.

4.1 Software Packages

A short description of the software packages used to generate Monte Carlo events, to simulate the passage of particles through the detector, to emulate the detector response, to reconstruct the event from the detector response and to analyse it, is given in this section.

PYTHIA The PYTHIA/JETSET [11] package consists of two Fortran 77 programs, PYTHIA and JETSET, usually referred to as PYTHIA. These programs have been designed for the generation of high-energy physics events. The emphasis is on multi-particle production in collisions between elementary particles. PHYTIA is intended to generate complete events, in as much detail as experimentally observable ones.
The program contains models for a number of physics aspects, including hard and soft interactions, parton distributions, initial and final state parton showers, multiple interactions, fragmentation and decay. Jet universality is assumed, which means that fragmentation is fundamentally the same for an e^+e^- or a pp event. For fragmentation a so-called string fragmentation model known as the Lund string model is used. The short distance interactions of quarks, leptons and gauge bosons are described by a perturbative approach. The branching ratios for decays of fundamental resonances are calculated dynamically. For a decay which is not isotropic, the matrix elements are taken into account.
The order of calculations done by PYTHIA is the following: The desired hard process is produced with two partons from the beam. The event record starts off with the parton configuration existing after hard interaction, initial- and final-state radiation, multiple interactions and beam remnants have been considered plus photons and leptons produced as part of the hard interaction. At this point string fragmentation starts, ending with particles that can be passed through detector simulation.

The version used in this study is PYTHIA 6.125

CMKIN CMKIN [12] is a CMS specific interface to several event generators, e.g. PYTHIA, CompHEP[13], Isajet and HERWIG. It provides an interface between physics generators output and the detector simulation GEANT used in the CMSIM and OSCAR[14] package. The output is in HEPEVT[1] standard structure. CMKIN is also used to set LHC specific parameters and call the generator routines to make this complex work easier for the user.
The version used in this study is CMKIN 1.3.0.

CMSIM and GEANT As a detector simulation, GEANT[15] describes the passage of the generated particles trough matter, in our case the CMS detector. It is a package consisting of detector description and simulation tools. CMSIM[16] is the CMS specific interface to GEANT3. Its purpose is to give users, who are unexperienced with GEANT, access to the full detector simulation provided by GEANT3.

COBRA Coherent Object-oriented Base Reconstruction and Analysis software[17] provides the general architecture of the CMS simulation and reconstruction framework.
It includes various interfaces to Monte Carlo generator output, the magnetic field map and the detector description. The most fundamental part of COBRA is called CARF (CMS Analysis and Reconstruction Framework). CARF contains an object-oriented base for reconstruction. The structure is event driven and provides action on demand.

ORCA The Object Oriented Reconstruction for CMS Analysis is used for reconstruction and detector performance evaluations. It is implemented in C++ and contains classes and methods to access reconstructed objects at different stages of detector information.
ORCA has subsystems that describe parts of the detector like Calorimetry, Tracker, etc. It also provides classes to describe reconstructed physics objects like vertices, jets and muons and the methods needed to reconstruct these objects, i.e. vertex finders, jet finders and the muon reconstructor. The development of ORCA is still in process, so the full functionality has not yet been provided.
The version used in this study is ORCA 7.6.1.

SCRAM The Software Configuration, Release And Management software has been developed to ensure that all developers use the same set of libraries, software environments, source codes and external products.

ROOT ROOT [19] succeeds PAW as an interactive data analysis system. In contrast to PAW, which was written in FORTRAN, ROOT is written in C++ and uses an object-oriented structure. It provides a framework for data analysis, e.g. histogramming, curve fitting, etc.
ROOT has a built-in C interpreter, which allows users to analyse data interactively without compiling. The fact that commands are given in C language, enables the user to put the analysis in a standalone program.

[1] High Energy Physics event

PAX The Physics Analysis Expert [20] is a C++ toolkit, developed at the University of Karlsruhe, which provides a new level of abstraction in particle physics analysis beyond detector specific reconstruction. For efficient physics analysis it is crucial to become independent of the experiment specific software. This enables physicists working in different experiment environments to share analysis code and it also protects the code from changes in the detector reconstruction.
Another benefit of the PAX toolkit is that it can deal with the large number of possible interpretations of a reconstructed event. In high energy physics reconstructed events contain masses of particles and there are numerous combinations of these particles that provide a possible interpretation of the event. PAX provides the possibility to manage and evaluate these interpretations. Future experiments like LHC will have to deal with these combinatorial problems.
Interfaces to different HEP data sources, like Monte Carlo generators or detector reconstruction data, provide the input for the PAX analysis. These interfaces are experiment or generator specific. They are already available in many cases (CDF, CMS, HEPEVT ntuples).
As it is placed between databases and physics-plots, PAX can be seen as a tool to enable the encapsulation of physics analysis.
A more detailed description can be found in [20].

Chapter 5

Simulation and Analysis

In this chapter, the simulation of signal and background samples and the analysis of these events will be discussed. In the first section, the simulation chain of detector-simulated events is explained step by step. The full detector-simulation of about 100000 events represents an important part of this study. The second section will introduce the analysis setup including muon reconstruction, event reconstruction and the calculation of the angle φ. The technical details of the analysis setup can be found in appendix A.

5.1 Simulation of Signal and Background

For both, signal and background samples, a full detector simulation was performed. Software used for this task is described in the preceding chapter. Samples with 20000 events each were produced for the signal $H \rightarrow 4\mu$ with $m_{\mathrm{Higgs}} = 200$ GeV and CP eigenvalues odd and even. As background samples, about 2200 $Zb\bar{b}$, 13000 $t\bar{t}$ and 40000 ZZ events were processed through the full simulation.
The event production chain follows the structure of figure 5.1. The events have been generated with the Monte Carlo generator PYTHIA. At this point, a preselection of the events have been performed in order to avoid time consuming simulation steps for events with a non-signal signature. Events remaining after preselection are processed through the detector simulation performed by GEANT3 and the results are digitised using the CMS reconstruction software ORCA. The output after digitisation has the same format as the real detector data will have.

5.1.1 Event Generation

Signal samples as well as ZZ and $t\bar{t}$ background samples were generated with PYTHIA version 6.215 using the CMS specific interface CMKIN version 1.3.0. For the simulation of the $Zb\bar{b}$ background CompHEP version 41.10 had to be used since not all necessary processes were implemented in PYTHIA. Hadronisation was again performed by PYTHIA.
The numerous parameter settings for PYTHIA were taken from the official CMS production[12]. In addition to these settings, a preselection routine has been implemented and an option for choosing the CP eigenvalue of the Higgs boson has been used. This will be explained in the following two paragraphs.

Preselection: In the preselection routine, events were selected by applying the following cuts:

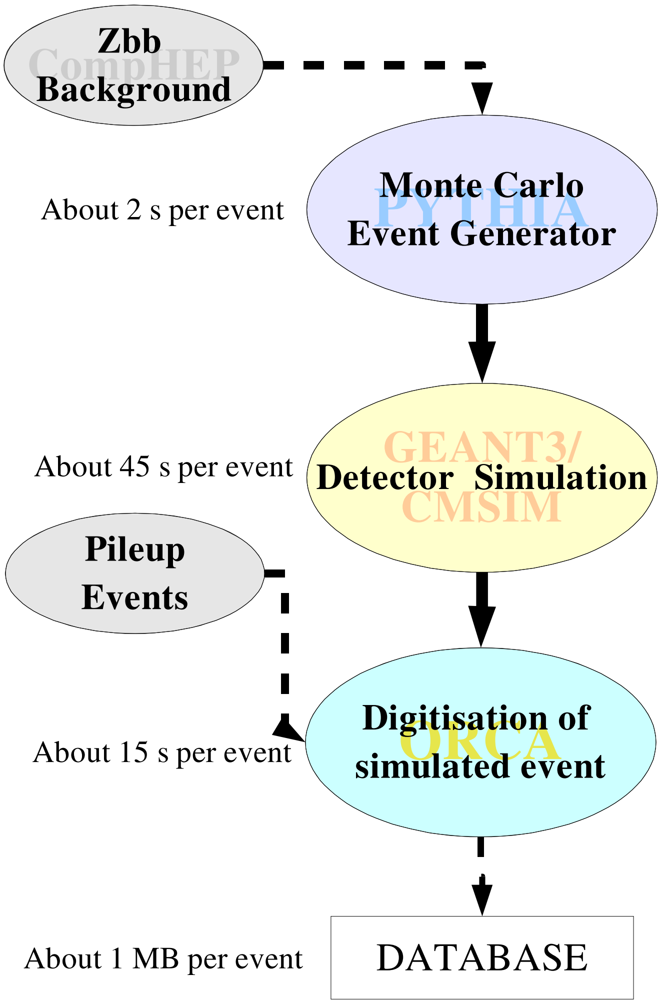

Figure 5.1: A simple visualisation of the production chain for full detector simulation. The times noted beside the different steps are approximations of the CPU times needed at the GridKa. The production ran on Pentium III and IV processors.

- At least four muons have to be in the sensitive region of the detector defined by $|\eta_\mu| < 2.5$.[1]
- The transverse momenta of at least four generated muons have to be greater then a threshold $p_{T,4}$.
- The momentum of at least one muon has to be greater then a threshold $p_{T,1}$.
- The masses of the reconstructed Z_1 and Z_2 boson have to fulfill $m_{Z_1,\min} < m_{Z_1} < m_{Z_1,\max}$ and $m_{Z_2,\min} < m_{Z_2} < m_{Z_2,\max}$.
- The mass of the reconstructed Higgs boson has to fulfill $m_{\text{Higgs,min}} < m_{\text{Higgs}} < m_{\text{Higgs,max}}$

To be able to apply cuts on the reconstructed masses the Z boson and Higgs boson masses are reconstructed using the following simple algorithm:

- Of all combinations of one μ^+ and one μ^- the combination with the invariant mass[2] $m_{\text{inv},2\mu}$ closest to the Z boson mass is taken to be the mass m_{Z_1} of the first Z boson.
- If this mass fulfills the cuts for Z_1, the invariant mass $m_{\text{inv},\mu^{+\prime},\mu^{-\prime}}$ of all combinations of two unlike charged muons $\mu^{+'}$ and $\mu^{-'}$ of the remaining muons are calculated.
- For each combination $\mu^{+'}$ and $\mu^{-'}$, satisfying $m_{\text{Z}_2,\min} < m_{\text{inv},\mu^{+\prime},\mu^{-\prime}} < m_{\text{Z}_2,\max}$, the invariant mass $m_{\text{inv},4\mu}$ of these two muons and the muons used to reconstruct the Z_1 is calculated.
- If one of these masses $m_{\text{inv},4\mu}$ fulfills $m_{\text{Higgs,min}} < m_{\text{inv},4\mu} < m_{\text{Higgs,max}}$, the event fulfills the cuts on reconstructed masses.

Values of the preselection cuts have been determined by considering distributions of the associated quantities and defining values that keep almost all of the signal events. As an example, the distribution of the reconstructed Z_1 mass is shown in figure 5.2. Preselection cuts on the transverse momentum of the muons rely on the values used by the trigger [27]. However, the selection cuts at this level have been chosen to be looser than the values for the trigger as well as the values of selection cuts after event reconstruction. Otherwise one would loose events that are just outside of the accepted region on generator level but are reconstructed inside this region due to detector resolution. The preselection cuts applied for this study are shown in table 6.1 and acceptance rates on signal and background processes can be found in table 6.2.

Higgs CP Eigenvalue in PYTHIA: Three different options for the CP eigenvalue of the Higgs boson are implemented in PYTHIA version 6.215. They can be chosen by setting the parameter MSTP(25):

- MSTP(25) = 0 is the default setting. The Higgs boson is handled as a scalar 0^{++} particle.
- MSTP(25) = 1 is the setting used to simulate a pseudo-scalar 0^{+-} Higgs boson.
- MSTP(25) = 2. Using this setting interferences of CP even and CP odd eigenstates are allowed.

The first two settings are used in this study.

[1] definition of the pseudo rapidity $\eta = -\ln(\tan(\theta/2)$

[2] $m_{\text{inv},\mu\mu'} = (E^\mu + E^{\mu'})^2 - (\vec{P}^\mu + \vec{P}^{\mu'})^2$

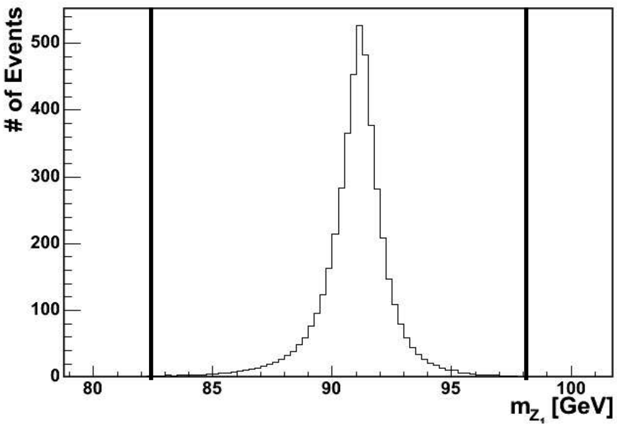

Figure 5.2: The preselection cuts, applied on the generated Z_1 boson mass. Almost no signal event is lost.

5.1.2 Detector Simulation

The generated events that had been accepted by the preselection cuts were processed through the detector simulation performed by GEANT3. The interface CMSIM version 133 was used to set CMS specific parameters and read in the geometry of the CMS detector. Parameter settings were taken from the official CMS production [12]. GEANT3 computes the passage of the particles, produced by the event generator, through the detector and determines the energy deposit at every point of the track. This step is very processor-time consuming as can be seen in figure 5.1.

5.1.3 Digitisation

Now, the detector output for the results from GEANT3 is simulated and converted into an ORCA database. This was performed by the routines `writeHits()` and `writeDigis()` implemented in ORCA version 7.6.1. The steering parameters are set according to the official CMS production [12]. The resulting databases are of a form which is similar to the real detector data. They are stored in the POOL [21] format which provides functionality needed to store databases in distributed structures as it is planed for grid-computing.
During digitisation it is possible to mix pileup into the database. This is explained in the following paragraph.

Pileup: Due to the high density of the beams at the LHC, more than one collision will appear per bunch crossing. These events are mostly minimum bias events. Furthermore, the high bunch crossing rate leads to the situation that particles of the preceding bunch crossing are still in the detector while an event is recorded. Altogether, every interesting event is stored together with a number of minimum bias events. This effect is called “pileup” and the underlying events are called “pileup events”. At CMS the number of pileup events are estimated to be about 3.5 events at low luminosity $L = 2 \cdot 10^{33}\ \mathrm{cm}^{-2}\mathrm{s}^{-1}$ and 17 events at high luminosity $L = 10^{34}\ \mathrm{cm}^{-2}\mathrm{s}^{-1}$.

For event simulation, pileup events are mixed into the database during digitisation. Minimum bias events are generated and processed through detector simulation. While digitising a signal event, minimum bias events are taken from this sample and mixed with the signal event. The detector output of signal and minimum bias events is then stored in one ORCA database.
In this study, pileup turned out to reduce the reconstruction efficiency due to a problem in the reconstruction software (see section 6.2). Therefore, the samples used in this study were produced without pileup.

5.2 Analysis Setup

The analysis performed in this study follows the structure shown in figure 5.3. More technical details of the analysis and its implementation in the object-oriented analysis framework PAX can be found in Appendix A.
Since the input databases of the analysis are processed through full detector simulation, the analysis will work with real detector data as well. In the first step, the muons are reconstructed with ORCA. From these muons the event will be reconstructed using methods implemented in PAX. Once the event is reconstructed, it can be analysed. In this study, the event analysis consists of: matching of the reconstructed particles with generated particles, comparison of reconstructed and generated quantities and the calculation of the decay plane angle φ. The results are stored in ROOT trees. After all events have been analysed, signal events can be separated from background events by applying selection cuts. To achieve the best possible results a cut-optimising procedure has been implemented (see section 7.3). Histogramming and visualisation of the results have been implemented in ROOT.

5.2.1 Muon Reconstruction

Muons are reconstructed from the ORCA databases using the *L3MuonReconstructor* implemented in ORCA. This routine returns the reconstructed tracks of the muons in the event. The kinematics, masses and charges of the muons can be calculated from these tracks. The *L3MuonReconstructor* is based on routines used for triggering the events. A standalone muon reconstructor was not yet available.
To be able to compare reconstructed and generated quantities, the generated event is also read from the ORCA database. In this study, also the energy deposit and transverse momentum in an area around the muons is of interest. With help of these quantities, events containing non-isolated muons can be excluded, which is important to suppress $t\bar{t}$ and $Zb\bar{b}$ background.

Muon Isolation: Two different quantities are of interest concerning muon isolation: the energy deposit (calorimeter isolation) and the transverse momentum (tracker isolation) around the muons. Both quantities are added up in a cone around the muon. Different cone sizes $\Delta R = \sqrt{\Delta\eta^2 + \Delta\phi^2}$ are possible. The optimal cone sizes to separate the channel $H \rightarrow 4\mu$ from its background have been determined in a recent study [26]. For tracker isolation a cone with $\Delta R = 0.24$ was found to be the optimal choice whereas for calorimeter isolation a wider cone size $\Delta R = 0.45$ was chosen.

5.2.2 Event Reconstruction

After reconstructing the muons, the $H \rightarrow ZZ \rightarrow 4\mu$ event has to be rebuilt. A particle is reconstructed from its decay products by calculating, the momentum as the sum of the decay products

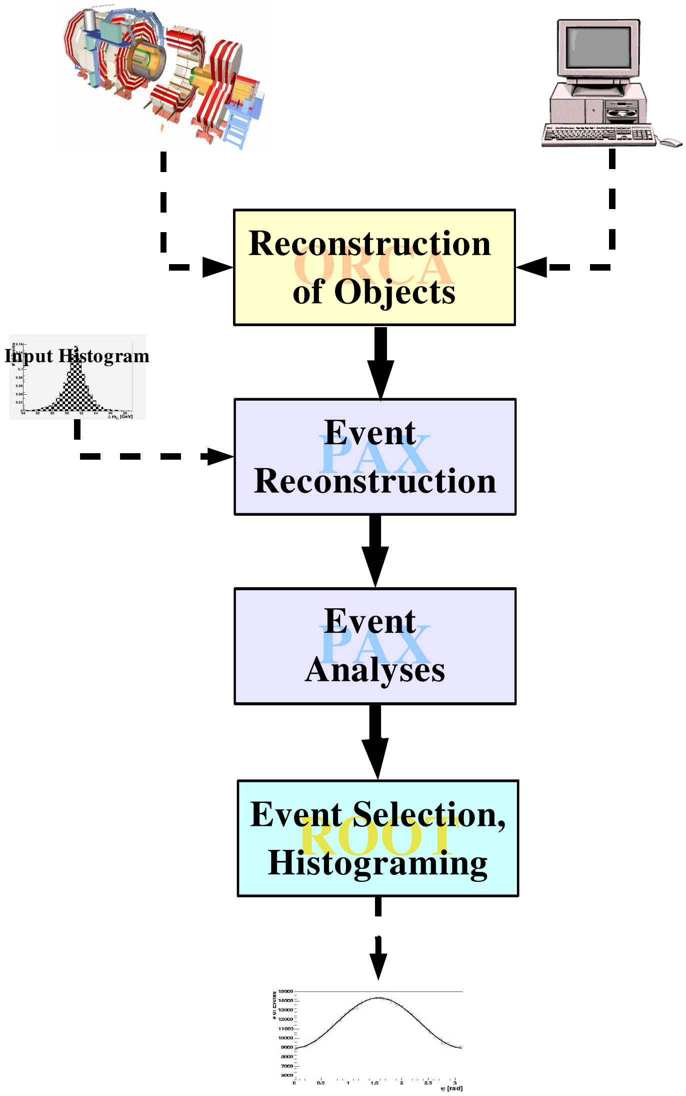

Figure 5.3: A simple overview of the event reconstruction and analysis and the software used for the different parts.

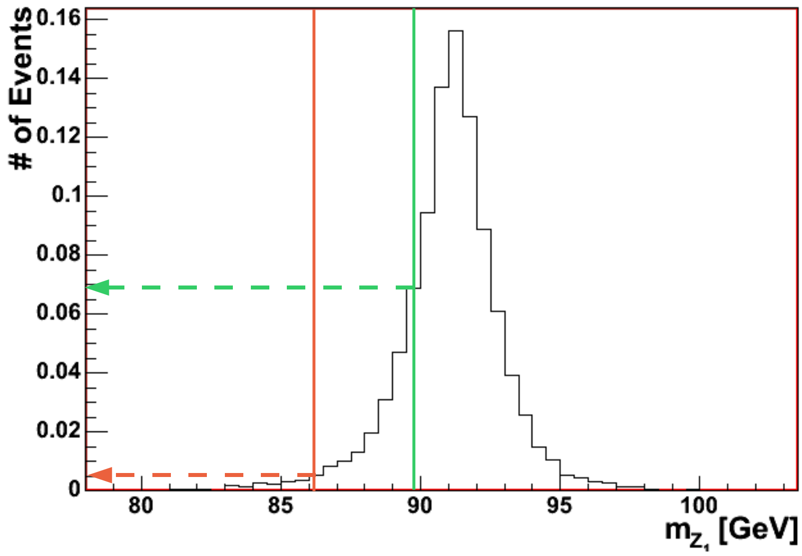

Figure 5.4: Rating of an event interpretation by comparing the reconstructed Z_1 mass with a reference histogram. The event closer to the expected value for the Z_1 mass is rated higher.

momenta, the mass as the invariant mass, and the charge as the difference of the two charges. The whole decay tree of one event is reconstructed in the following way:

- Every combination of the reconstructed muons (of one event), yielding two Z bosons (μ_1^+,μ_1^- and μ_2^+,μ_2^- plus X), is calculated.
- For each of these combinations, the Higgs boson is reconstructed from the Z bosons.
- Every combination with a $H \to ZZ \to 4\mu$ decay tree is added to a list of possible event interpretations.
- The interpretations are ranked by a likelihood rating, which compares the reconstructed quantities, e.g. the reconstructed Z boson masses, with reference histograms. An example is shown in figure 5.4. More information about the reference histograms used in this study can be found in appendix A.7.
- The event interpretation with the best likelihood rating is selected as signal.

5.2.3 Analysis of the Reconstructed Event

Once the event has been reconstructed, the reconstructed quantities can be filled into ROOT trees. To be able to compare these quantities with generated ones, the reconstructed particles have to be matched with the according generated particles.

Matching of Particles: Two methods of matching are implemented in the analysis at hand. Reconstructed Muons are matched to their generated counterparts by comparing the hits of the simulated track to the hits of the reconstructed track.

Muons that could not be matched in this way, as well as Z and Higgs bosons are matched via a minimum angular difference criterion. The criterion q used in this study is defined as:

$$q = e^{-\sqrt{frac\Delta\phi\sigma_{\phi}{}^2 + frac\Delta\theta\sigma_{\theta}{}^2}}\,. \tag{5.1}$$

The matching via simulated and reconstructed tracks is obviously more accurate since about ten hits are matched for each muon. This is much more information than is used for the matching in θ and ϕ, done for the minimum angular difference criterion.

After matching is performed, reconstructed and generated quantities can be compared and resolution studies can be performed. A special quantity needed for this study is the angle φ between the decay planes of the Z bosons. Its calculation is explained in the following paragraph.

Calculation of the Angle φ: The angle φ is calculated in the following way [22]:

- A transformation of the particles into the rest frame of one of the Z bosons is performed.
- The z-axis is given by the negative momentum of the other Z boson, the decay plane of this boson defines the x-z-plane and the y-axis is chosen in the way, that one gets a right-handed coordinate system.
- The decay plane of the latent Z boson is projected on the x-y-plane.
- Now φ is the angle between the x-axis and this projection.

5.2.4 Event Selection and Histogramming

When signal and background events are analysed, selection cuts can be applied and the results can be filled into histograms. Event selection and histogramming of the results are performed with ROOT. This part of the analysis is described in detail in the following chapters.

Chapter 6

Detector Studies

This chapter addresses resolution and efficiency studies on the reconstructed quantities relevant for this analysis. The results will be compared to earlier studies [26, 25] and the values specified in the Tracker Technical Design Report [28].

6.1 Branching Ratios, Preselection and Expected Number of Events

At first a summary of the preselection cuts applied at the level of event generation, the associated acceptance for signal and background events as well as the resulting cross sections will be given. Values used for the preselection cuts can be seen in table 6.1. Production cross sections, branching ratios, preselection acceptance and the resulting numbers of events are shown in table 6.2. The production cross sections are taken from [26] and [23]. The acceptance ξ is defined as the ratio of the number of events accepted by the preselection cuts and the number of events produced by the event generator:

$$\xi = N_{\text{accepted}}/N_{\text{generated}} \, . \tag{6.1}$$

η	$p_{T,1}$ [GeV]	$p_{T,4}$ [GeV]	m_{Z_1} [GeV]	m_{Z_2} [GeV]	m_{Higgs} [GeV]
$< 2,5$	> 10	> 2.8	82–98	50–98	170–210

Table 6.1: Preselection cuts applied during event generation with the Monte Carlo generator PYTHIA.

channel	σ_{prod} in [pb]	$\sigma_{prod} \cdot$ BR in [pb]	ξ in [%]	$\sigma_{tot} \cdot \xi \cdot$ BR in [fb]	expected events for $\int L = 20$ fb^{-1}
$H \to 4\mu\ : m_H = 200$ GeV	17.30	0.0051	58.5	3.02	60.4
Zbb	1492	512	0.0041	2.08	41.6
$t\bar{t}$	886	8.86	0.013	1.13	22.6
$Z\bar{Z}$	18.2	0.021	7.68	1.584	31.68

Table 6.2: Cross sections, branching ratios, preselection acceptance ξ and the resulting expected numbers of events for signal and background for an integrated luminosity of $\int L = 20$ fb^{-1}.

6.2 Reconstruction Efficiency

6.2.1 Definition of the Reconstruction Efficiency

The reconstruction efficiency in the context of this study is defined as the ratio of the number of reconstructed events with at least four muons and the number of generated events with four muons, both fulfilling the requirements of $|\eta_\mu| < 2.4$ and $p_{\mathrm{T},\mu} > 3$ GeV:

$$\epsilon_{4\mu} = N_{4\mu,\mathrm{rec}}/N_{4\mu,\mathrm{gen}} \tag{6.2}$$

This reconstruction efficiency is directly depending on the reconstruction efficiency of one muon ϵ_μ, which is defined as the ratio of the number of reconstructed muons and the number of generated muons where the generated muons fulfill $|\eta_\mu| < 2.4$ and $p_{T,\mu} > 3\mathrm{GeV}$. It is also required that the reconstructed muons can be matched via a minimum angular difference criterion to a generated muon:

$$\epsilon_\mu = N_{\mu,\mathrm{rec}}/N_{\mu,\mathrm{gen}} \tag{6.3}$$

6.2.2 Reconstruction Efficiency of the Samples

The reconstruction efficiency ϵ_μ of one muon using the *L3MuonReconstructor* in ORCA version 7.6.1 turned out to be lower than specified in the Tracker Technical Design Report (TDR) for the CMS detector [28]. The efficiency as a function of the pseudo-rapidity η of the muons for high and low luminosity and without pileup can be seen in figure 6.1. A correlation between the reconstruction efficiency and the amount of pileup events mixed into the database can be observed. The obviously too small efficiency is due to problems with the preliminary version of the CMS reconstruction software that was used for this study. In order to achieve the best possible efficiency, the samples were produced without pileup. The reconstruction efficiency for samples without pileup was found to be about 90% compared to 97% expected in the TDR. However, signal and background processes are affected in the same way and the problem has no influence on the resolution of the observables. A lower reconstruction efficiency of one muon results in a lower efficiency to reconstruct the event. The reconstruction efficiencies $\epsilon_{4\mu}$ for signal and background events after preselection are shown in table 6.3.

channel	reconstruction efficiency
$H \to 4\mu : m_H = 200$ GeV	65.87%
$ZZ^* \to 4\mu$	57.9%
$t\bar{t} \to 4\mu$	57.0%
$Zb\bar{b} \to 4\mu$	58.7%

Table 6.3: Efficiency to reconstruct four muons in signal and background events after applying preselection cuts as defined in table 6.1 and for the region of $|\eta_\mu| < 2.4$. Due to problems with the muon reconstruction in ORCA version 7.6.1 the reconstruction efficiency is about 15% lower than in [26] and in the Tracker TDR [28].

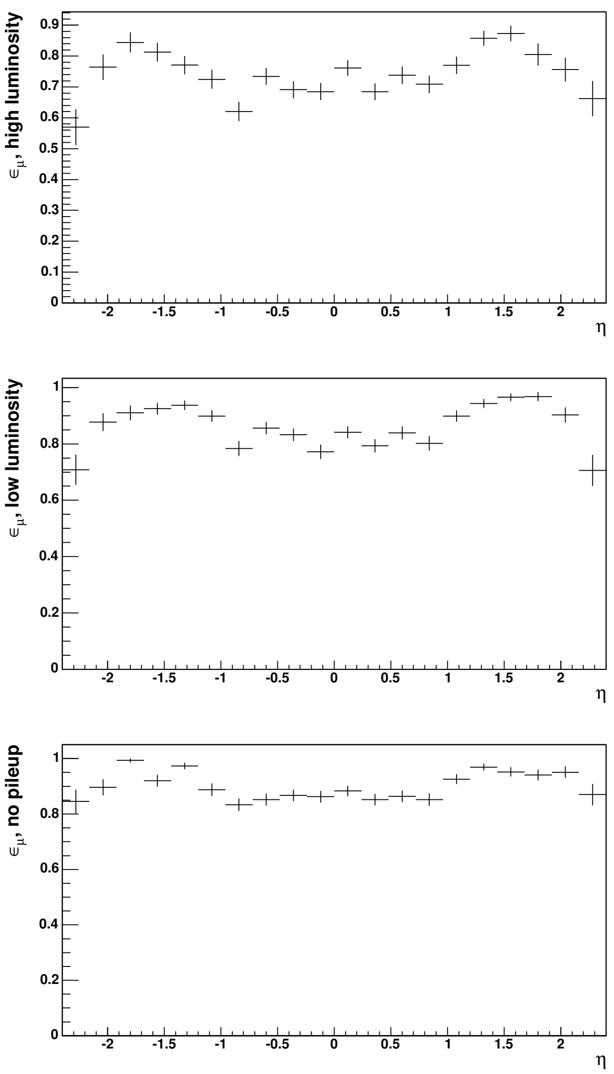

Figure 6.1: Reconstruction efficiency ϵ_μ using ORCA version 7.6.1. The error bars are the statistical errors of the measurement. The mean values are for high luminosity: $\epsilon_{\mathrm{mean}} \approx 74\%$, low luminosity: $\epsilon_{\mathrm{mean}} \approx 84.6\%$ and without pileup: $\epsilon_{\mathrm{mean}} \approx 89.2\%$ using ORCA version 7.6.1.

6.3 Reconstructed Quantities and Resolution Studies

In this section a study of the distributions of the relevant reconstructed quantities and the resolution achieved on these quantities will be performed. The results will be compared to earlier studies [25, 26] and the values specified in the Tracker Technical Design Report. The distributions will also give an outlook, which quantities can be used to separate the signal events from background events. In order to improve the comparability of signal and the background processes, the total number of events is normalised to one for most of the distributions in this section. Signal process are taken from the CP even signal sample. Distributions for the CP odd sample are similar.

6.3.1 Angular Resolutions of the Muons

Since the analysis of the CP eigenvalue of the Higgs boson, performed in this study is based on the angular distribution of the muons, a good resolution of the detector angles of the muons is essential for the success of the analysis. In figure 6.2 and figure 6.3 the resolution of ϕ and θ for the muons in the signal sample is shown. Matching of the generated muons with the reconstructed muons is done by using the method described in appendix A.3. The angular resolution is about 0.4 mrad for ϕ and 0.5 mrad for θ. This is in good agreement with the Tracker TDR [28] and recent studies [25, 26].

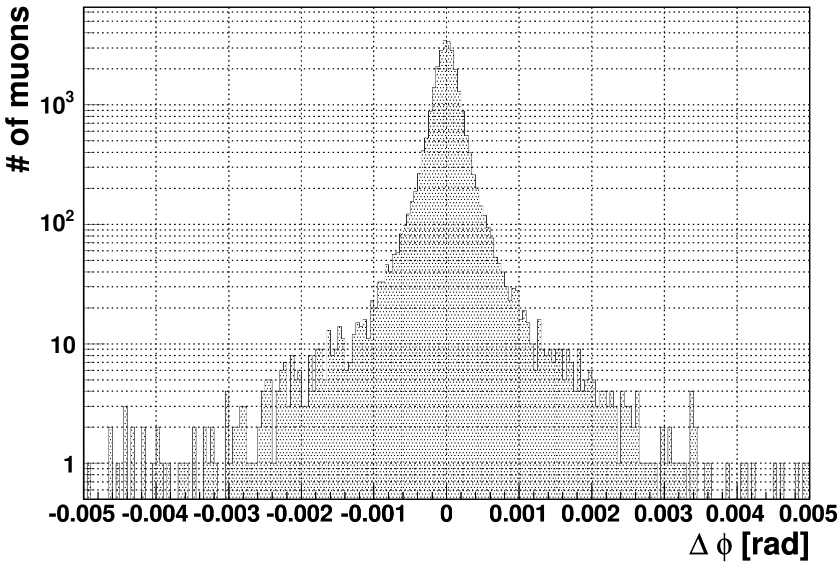

Figure 6.2: The angular resolution of the muons is about 0.4 mrad for ϕ.

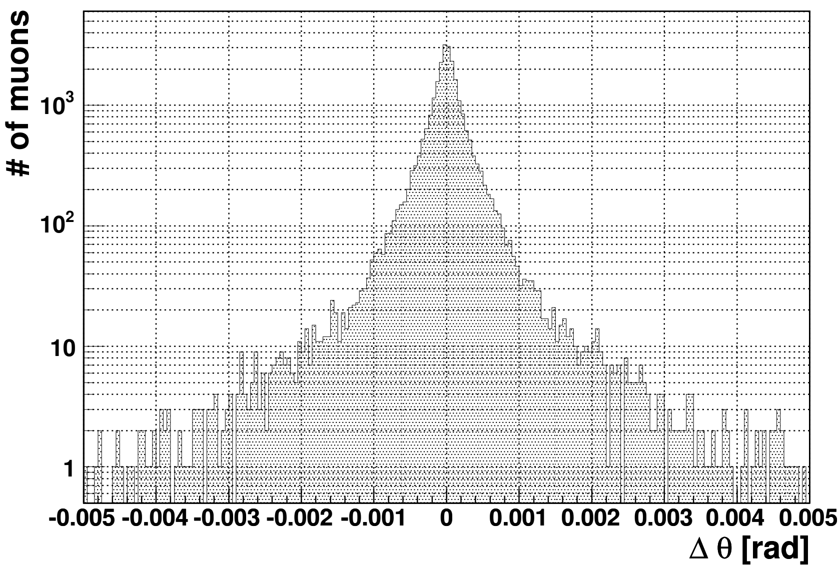

Figure 6.3: The angular resolution of the muons is about 0.5 mrad for θ.

6.3.2 Transverse Momenta of the Muons

Since the muons in the final state of $H \rightarrow 4\mu$ are decay products of Z bosons, they have a high transverse momentum compared to muons from other processes. This characteristic is used in the trigger to discard uninteresting events. It can also be used to suppress background events especially from the $t\bar{t}$ and $Zb\bar{b}$ channel. This can easily be seen by looking at figure 6.4 and 6.5 where the distributions of transverse momentum for each of the four reconstructed muons sorted from highest to lowest p_T are plotted for signal and background events. There is no significant difference in the distributions of the muons with highest and second highest p_T. This is obvious since for ZZ and $Zb\bar{b}$ processes two muons originate from a Z boson and for the $t\bar{t}$ process two muons are W boson decay products. However, additional muons in $Zb\bar{b}$ and $t\bar{t}$ processes originate from b quark jets and have therefore lower transverse momentum than the signal event. This characteristic offers a possibility to suppress the $Zb\bar{b}$ and $t\bar{t}$ background.

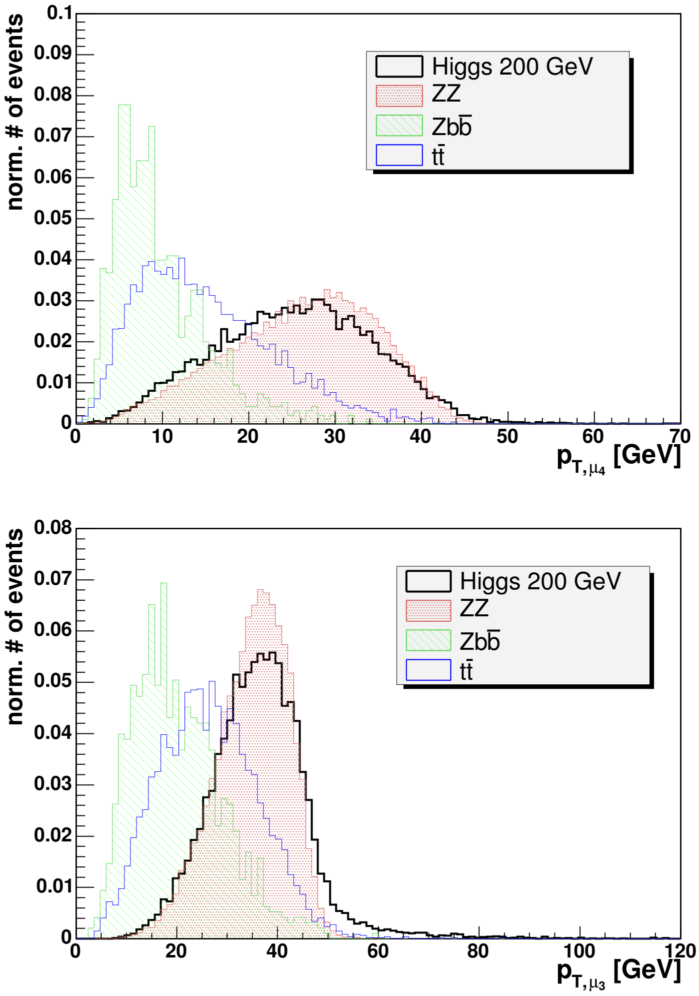

Figure 6.4: Distribution of the transverse momentum of the reconstructed muons μ_4 and μ_3 with the lowest and second lowest transverse momentum. The total number of events of a distribution is normalised to one.

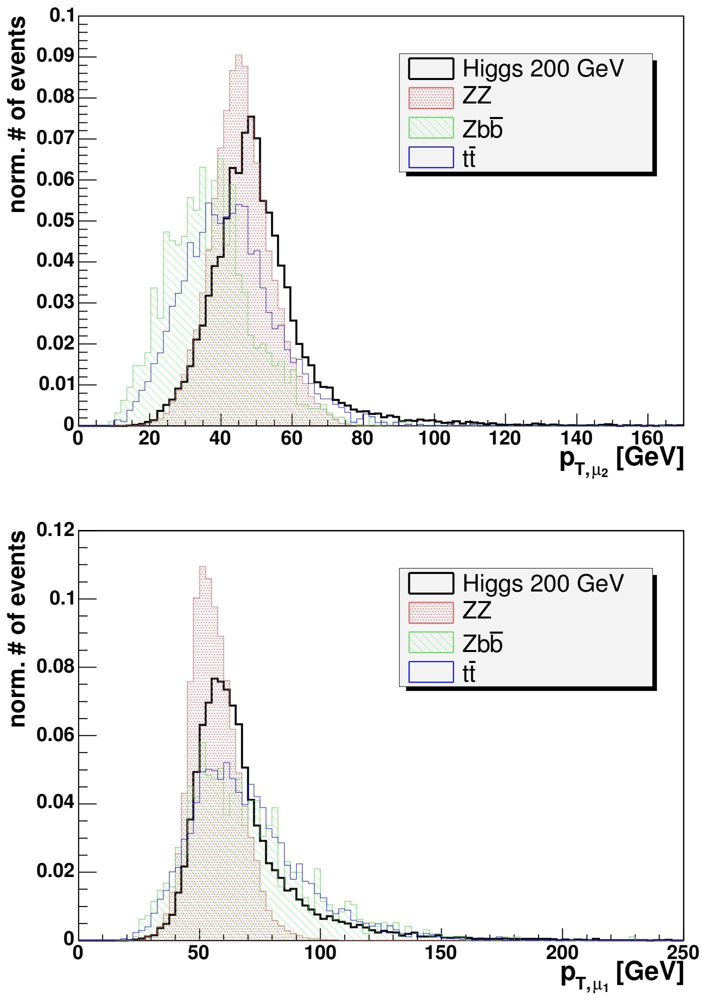

Figure 6.5: Distribution of the transverse momentum of the reconstructed muons μ_1 and μ_2 with the highest and second highest transverse momentum. The total number of events of a distribution is normalised to one.

The kinematics of the event including the Z and Higgs boson masses are calculated from the momenta of the reconstructed muons. Therefore, a good resolution of the reconstructed momentum of the muons is one of the major challenges of the CMS detector. In figure 6.6, the resolution of $1/p_T$ is plotted in a logarithmic histogram. Its standard deviation is about 0.0009 GeV^{-1}. The p_T resolution changes depending on the transverse momentum as it is shown in figure 6.7. This is due to the fact, that the momentum is calculated from the bending of the track in the magnetic field. This is harder for high momenta since the bending approaches zero. The resolution is between 1% and 2% throughout the whole range. This is in agreement with the Tracker Technical Design Report [28] which specifies the resolution to about 1.2% for low transverse momentum degrading to 4.3% for p_T's higher than 100 GeV.

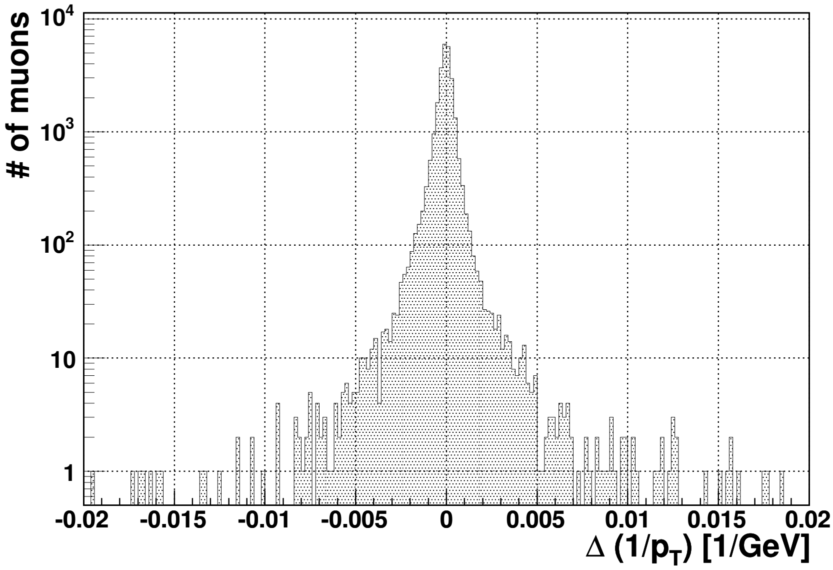

Figure 6.6: Resolution of the transverse momentum of the reconstructed muons with $\Delta 1/p_T = 1/p_{T,gen} - 1/p_{T,rec}$ and $\sigma \approx 0.0009$ [1/GeV].

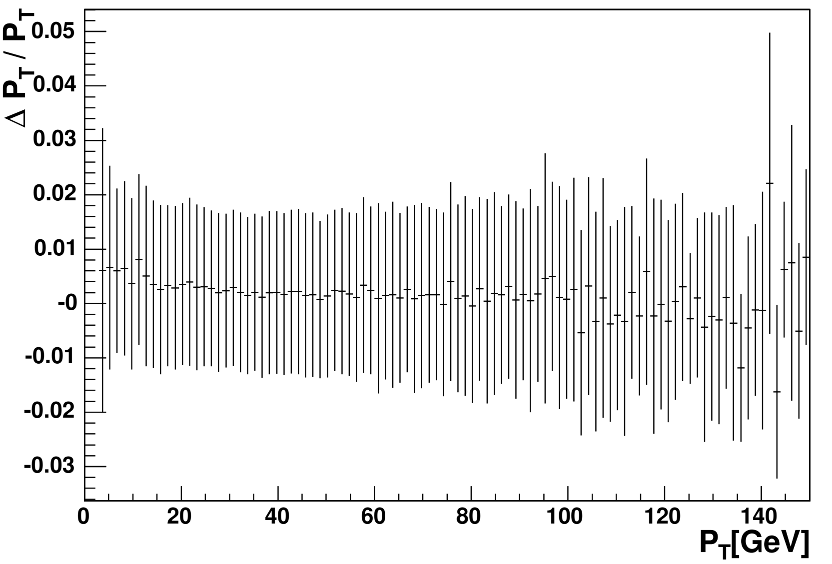

Figure 6.7: Resolution of the transverse momentum of the reconstructed muons $\Delta p_T/p_T$ as a function of p_T. The error bars are the standard deviations of the distributions in each slice in p_T.

6.3.3 Muon Isolation

One of the outstanding characteristics of the channel $H \rightarrow 4\mu$ is the presence of four isolated muons in the final state. Especially $t\bar{t}$ and $Zb\bar{b}$ events can be suppressed by applying an isolation criterion. Two criteria are used in this study. The sum over all transverse momenta (tracker isolation) and the sum over the transverse energy deposits (calorimeter isolation) in a cone with radius ΔR around the muon as it is explained in section 5.2.1. Figure 6.8 shows the sum of transverse momenta for signal and background processes. The small peak visible at 10 GeV can be explained by the reconstruction method. The transverse momentum of any single track inside ΔR, which is greater than 10 GeV is set to 10 GeV.

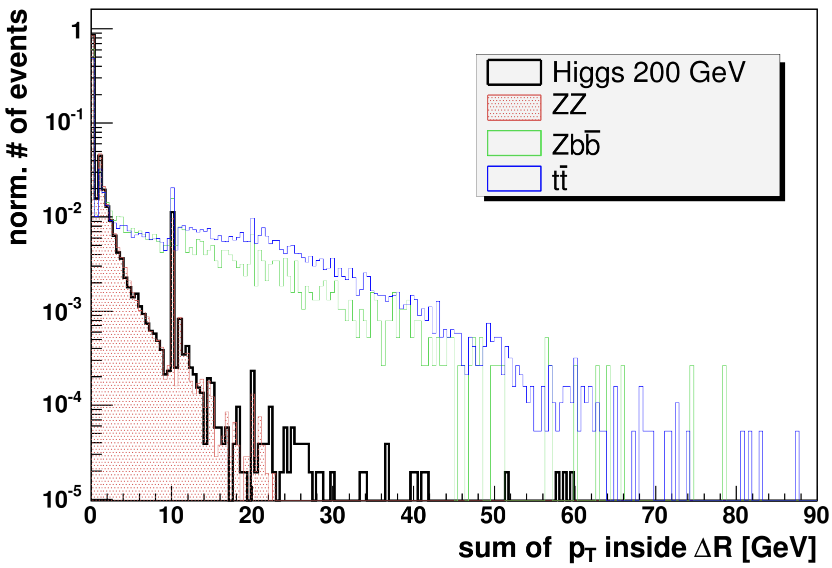

Figure 6.8: Distribution of the sum of transverse momenta around the reconstructed muons for signal and background events. The total number of events of a distribution is normalised to one. Considering the peak at 10 GeV note the text. If the only one track inside the cone has a transverse momentum greater than 10 GeV, the cone energy is set to 10 GeV.

6.3.4 Reconstructed Z Bosons

The Z bosons are reconstructed as described in section 5.2.2. Since the $H \to 4\mu$ sample is produced with a Higgs mass of 200 GeV, which is above the ZZ threshold, two real Z boson mass distributions are expected for the signal events. For the ZZ background the distributions will not differ significantly. However for $t\bar{t}$ and $Zb\bar{b}$ events, where two of the four muons emerge from b quark jets, only one Z mass distribution resembles the Z boson mass distribution. The two mass distributions for the Z bosons are shown in figure 6.9 and figure 6.10. During event reconstruction, the reconstructed Z boson whose mass is closer to the theoretical value of 91.187 GeV is named Z_1 the other one is named Z_2. Since both Z bosons are real, this selection procedure results in a dip around 91.187 GeV in the distribution of Z_2. Furthermore, the distributions of Z_2 for $t\bar{t}$ and $Zb\bar{b}$ show a significant amount of events in which the Z boson mass is reconstructed outside the preselection cuts applied at generator level. Especially a peak near $m_{Z_2} = 0$ is noticeable. The reason for this is the low efficiency for muon reconstruction. About 30 % of the generated $t\bar{t}$ and $Zb\bar{b}$ events have more than four muons. When losing one muon as a result of reconstruction inefficiency the Z bosons reconstructed after detector simulation consist of a different set of muons than was used at generator level and generally the reconstructed Z_2 mass is lower.

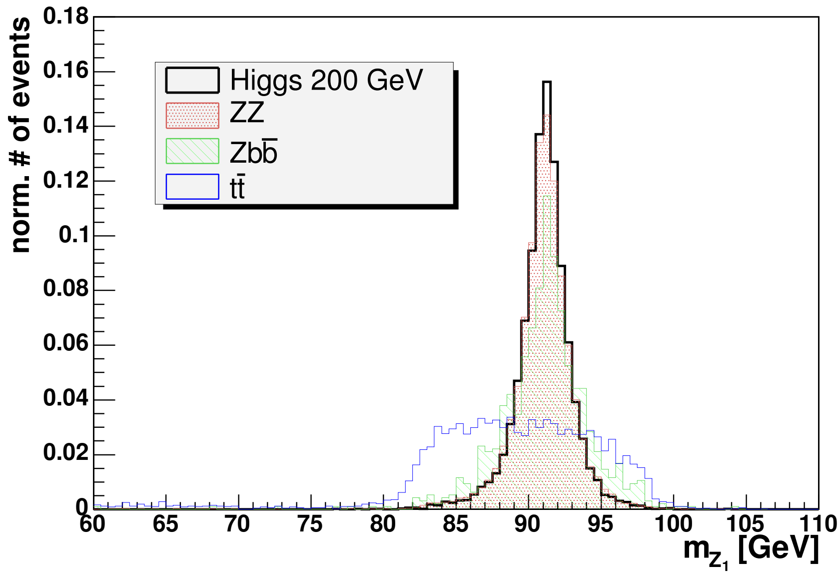

Figure 6.9: Distribution of the reconstructed Z_1 boson mass. The total number of events of a distribution is normalised to one.

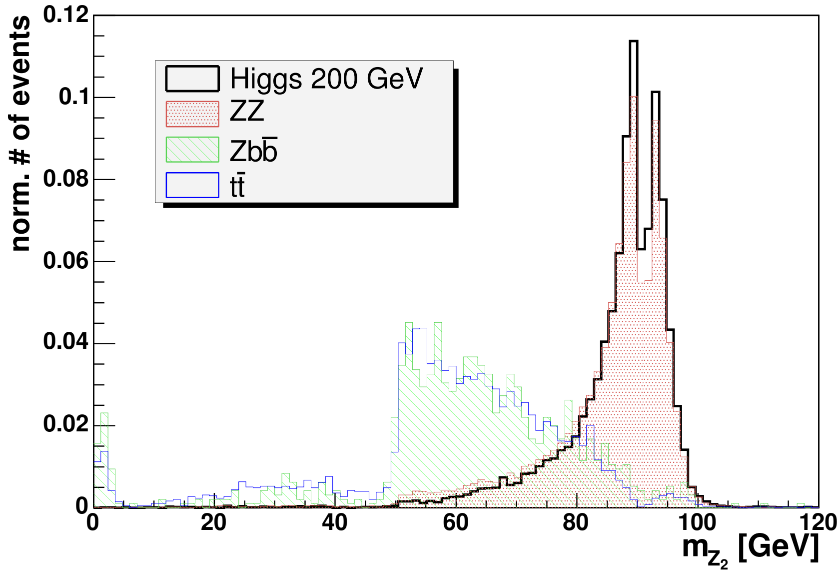

Figure 6.10: Distribution of the reconstructed Z_2 boson mass. The total number of events of a distribution is normalised to one.

The resolutions of the two reconstructed Z boson masses, defined as $\Delta m^{Z}_{\text{rec}} = m^{2\mu}_{\text{inv,rec}} - m^{2\mu}_{\text{inv,gen}}$, are shown in figure 6.11 and figure 6.12. The standard deviation is about 1.2 GeV for Z_1 and 1.7 GeV for Z_2. This is in good agreement with recent studies [25, 26].

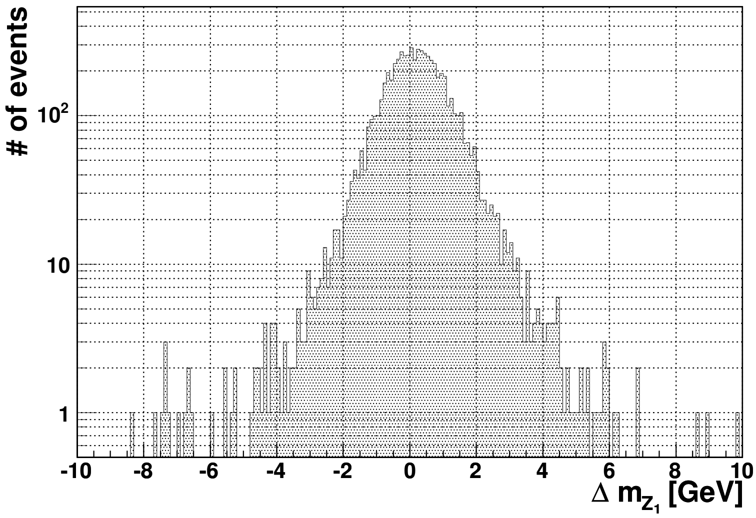

Figure 6.11: Resolution of the reconstructed Z_1 boson mass with $\sigma \approx 1.2$ GeV.

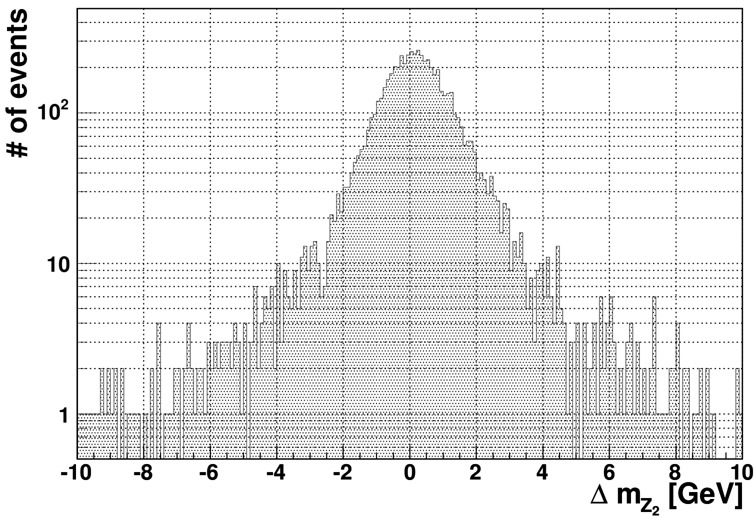

Figure 6.12: Resolution of the reconstructed Z_2 boson mass with $\sigma \approx 1.7$ GeV.

6.3.5 Reconstructed Higgs Boson

Figure 6.13 shows the distributions of the invariant Higgs boson mass for signal events with $m_{\mathrm{Higgs}} = 200\,\mathrm{GeV}$ and background events after detector simulation and reconstruction. The distributions are weighted to represent an integrated luminosity of $20fb^{-1}$, which corresponds to one year operating time of the LHC at low luminosity. The only cuts applied are the preselection cuts at Monte Carlo generator level. Compared to recent studies at lower masses [26, 25, 24] the level of $t\bar{t}$ and $Zb\bar{b}$ background is significantly lower, whereas the ZZ background has its maximum around the double of the Z boson mass of about 180 GeV. The ZZ background can already be identified as the most relevant background process for the study of observability and the CP eigenvalue determination. Parametrisation of the background, as will be done in section 7.2, is not trivial in the mass range shown in figure 6.13. However, considering a Higgs boson mass of 200 GeV, one can narrow the mass window to a range between 190 GeV and 207 GeV. In this mass range the background can be considered flat. The accuracy of Higgs boson mass measurement can be estimated by looking at the residual $\Delta m_{\text{Higgs,rec}}$ of the invariant reconstructed Higgs boson mass defined as $\Delta m_{\text{Higgs,rec}} = m^{4\mu}_{\text{inv,rec}} - m^{4\mu}_{\text{inv,gen}}$ (see figure 6.14). The standard deviation of the distribution of the residuals is about 2.5 GeV.

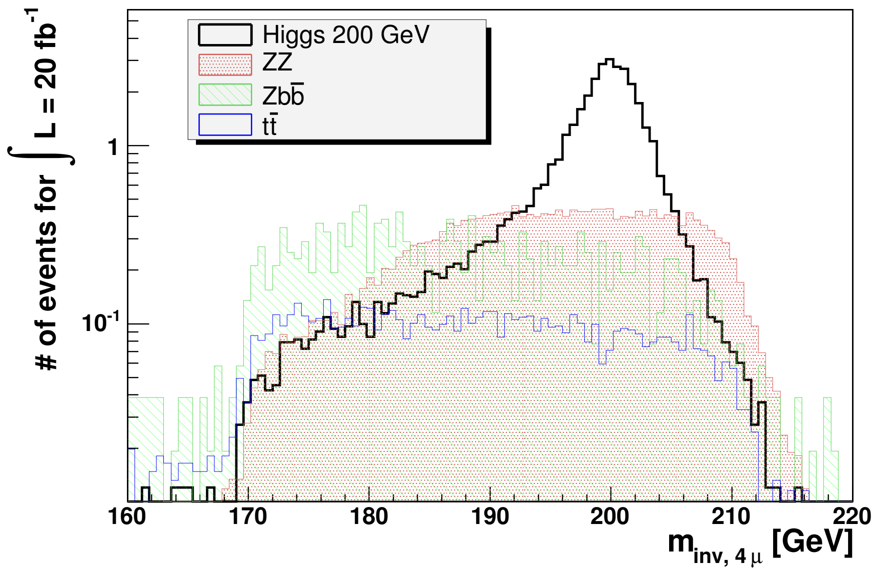

Figure 6.13: Logarithmic distribution of the invariant four muon mass (reconstructed Higgs boson mass) for signal and background events.

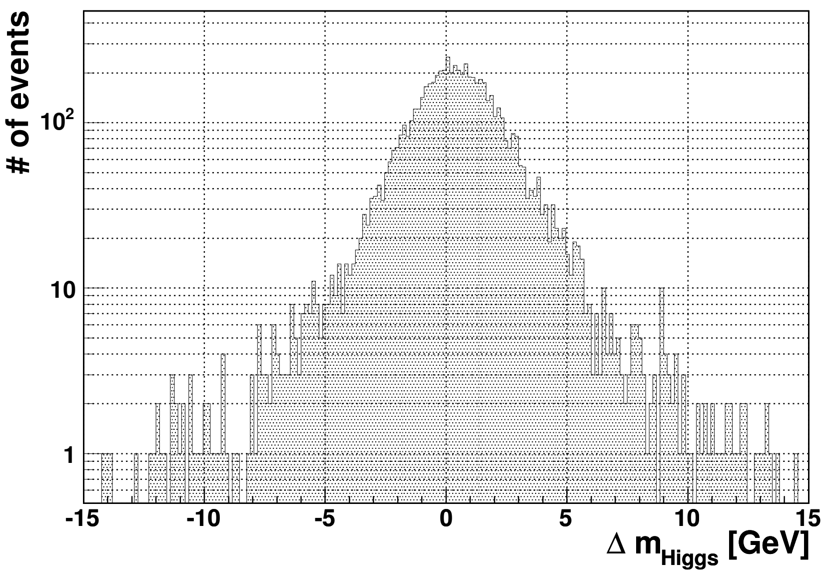

Figure 6.14: Resolution of the reconstructed Higgs boson mass with $\sigma \approx 2.5$ GeV.

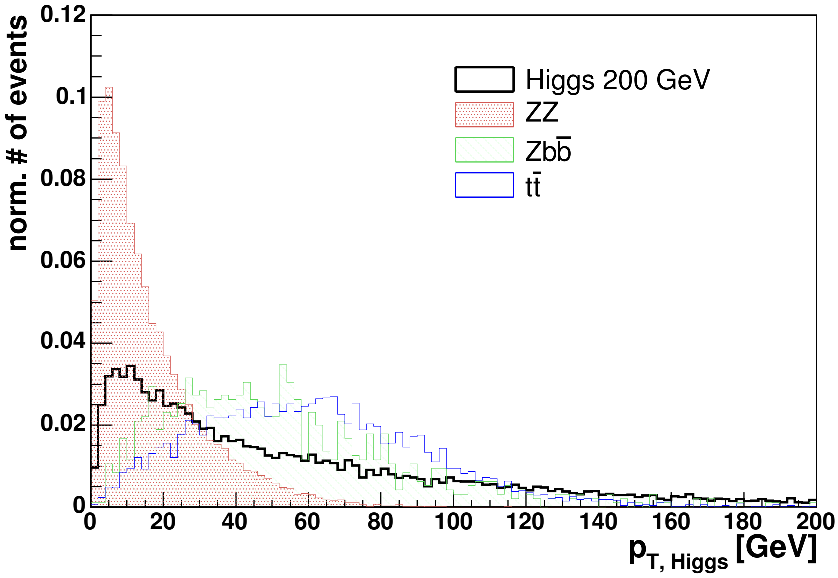

Figure 6.15: Transverse momentum of the reconstructed Higgs boson for signal and background events. The total number of events of a distribution is normalised to one.

6.3.6 Transverse Momentum of the Reconstructed Higgs Boson

In a recent study [23] the transverse momentum of the four muon system, here also called the transverse momentum of the reconstructed Higgs boson, is proposed as a selection criterion for events above the ZZ threshold. This criterion is especially useful for the suppression of the ZZ background which is almost indistinguishable from the signal. The Higgs boson is predominantly produced in gluon fusion with a p_T of the order of the gluon transverse momentum inside the proton. A Higgs boson generated in higher order processes in association with other partons has a higher transverse momentum. Whereas considering ZZ background, quark-antiquark annihilation is the dominant production mechanism, giving the four muon system a softer transverse momentum. This effect is shown in figure 6.15.

Chapter 7

Signal Observability

In this section the estimation of significance of signal observability for a Higgs boson mass of 200 GeV and an integrated luminosity of $20fb^{-1}$ will be carried out. At first the selection cuts applied to suppress the background will be introduced. In order to optimise these cuts, a procedure, described in the following section, has been implemented. In the last sections different estimators of significance will be discussed and the results after cut optimisation will be presented.

7.1 Selection Cuts

The preceding chapter already gave an impression of the selection quantities that are the most relevant for the $H \rightarrow 4\mu$ channel. This section will offer a closer look at the selection cuts applied at the level of fully simulated and reconstructed events.

Cuts on the Transverse Momenta of the Reconstructed Muons: The distribution of the muons with the highest and second highest transverse momentum (see figure 6.4) show only small differences between signal and background events. The distributions for the two muons with lowest transverse momentum look more promising (see figure 6.5). Muons from signal events have a higher transverse momentum compared to $t\bar{t}$ and $Zb\bar{b}$ events where muons emerge from b quark jets. One is able to cut away a good part of these background events while losing just a small amount of signal events. The cut on the muon with the lowest transverse momentum has to be set to at least 3 GeV, since otherwise the reconstruction efficiency would be to low. This restricts the scope for a selection cut on this value.

Cuts on the Reconstructed Z Boson Masses: Looking at the distribution of the reconstructed Z_1 mass (see figure 6.9) it is evident that a cut on this mass will only help to suppress $t\bar{t}$ background effectively since this background process does not contain a Z boson like ZZ and $Zb\bar{b}$ events do. Since $Zb\bar{b}$ contains just one Z boson, this background can be suppressed by cuts on the Z_2 boson mass (see figure 6.10).

Muon Isolation: A cut on the muon isolation described in section 6.3.3 effectively suppresses $Zb\bar{b}$ and $t\bar{t}$ background since these processes contain non-isolated muons. The sum of transverse momenta around the muons is shown in figure 6.8. This criterion and the sum of deposited energy around the muons are highly correlated. The cut on the sum of transverse momenta turned out to be more effective in this study. Applying a cut on the deposited energy in addition does not show a significant effect.

Cut on the Transverse Momentum of the Reconstructed Higgs: This cut is especially helpful in suppressing the ZZ background. The signal events have a higher transverse momentum than ZZ events (see figure 6.15), an effect which is explained in section 6.3.6. This characteristic offers the best possibility to reduce ZZ background.

7.2 Parametrisation of the Mass Distribution

For the process of cut optimisation a parametrisation of the mass distribution of signal plus background events is needed for the determination of the number of signal and the number of background events. Parametrisation of the signal consists of a Gaussian distribution, centered at the Higgs boson mass with a width of Δ_{m_H}, and an additional term taking into account the radiative tail of the signal peak. This term is of the form $t(m; m_H) = C \cdot (m_H - m)^2 \cdot \exp{(m - m_H)/\lambda}$ for $m < m_H$ and 0 for $m > m_H$. For the study at hand with $m_{\mathrm{Higgs}} = 200$ GeV the parameters of the additional term have been determined to be $C = 0.01$ and $\lambda = 2.8$. The background distribution was assumed to be a straight line which is reasonable in the investigated mass range between 190 and 208 GeV (see figure 6.13). Finally the complete function, parameterising the signal plus background distribution, is given by:

$$
\begin{aligned}
f_{s+b}(m) &= f_s(m) + f_b(m)\ , && (7.1)\\
f_b(m) &= B\ , && (7.2)\\
f_s(m) &= \begin{cases} A \cdot \left[e^{(m-m_H)^2/(2\cdot\Delta_{m_H})} + t(m; m_H) \right] & ,\text{for m} < \mathrm{m_H} \\ A \cdot \left[e^{(m-m_H)^2/(2\cdot\Delta_{m_H})} \right] & ,\text{for m} > \mathrm{m_H} \end{cases} && (7.3)
\end{aligned}
$$

with

$$t(m; m_H) = C \cdot (m_H - m)^2 \cdot e^{(m-m_H)/\lambda} \qquad (7.4)$$

With this parametrisation, N_s and N_b can be obtained by fitting function (7.1) to the mass distribution and integrating the terms for the signal and the background in a mass window of $m_H \pm \Delta_m$. During the optimisation of the cut values, Δ_m has been determined to be $1.9 \cdot \Delta_{m_H}$. An example of this parametrisation fitted to the mass distribution of signal plus background events can be seen in figure 7.1.

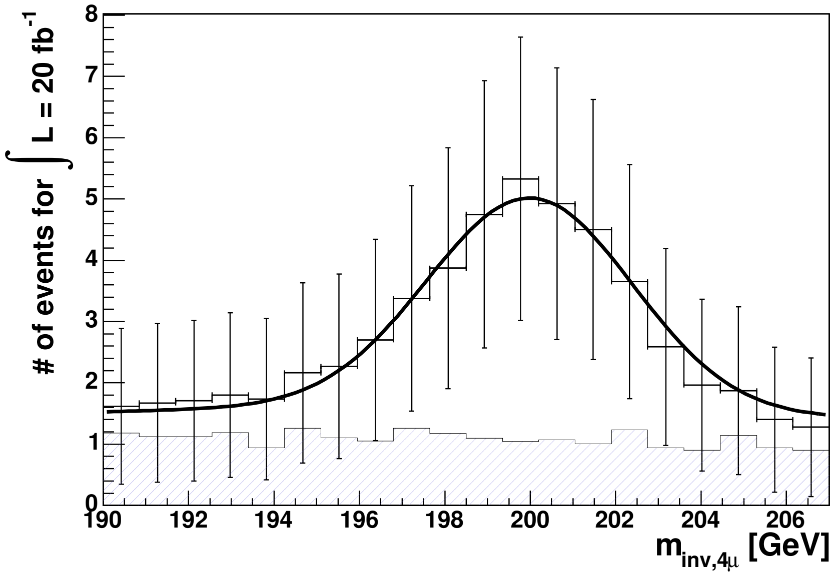

Figure 7.1: Reconstructed Higgs mass distribution of signal plus background events for $\int L = 20f^{-1}$. The background added to the distribution is marked in hatched blue. Only preselection cuts are applied. The error bars are the statistical errors for $\int L = 20f^{-1}$

7.3 Cut Optimisation

For the optimisation of the cuts in order to achieve the highest possible significance a program based on the data analysis framework ROOT has been developed. This program uses an iterative approach. The value of one cut is altered until the best value is found while the others remain fixed. After processing all cuts in this way they are passed through the process a second or even third time in order to adjust changes due to the correlation between the selection quantities.
As an estimator of significance $S_K = 2 \cdot (\sqrt{N_s + N_b} - \sqrt{N_b})$, which is described in the following section, has been chosen. It has the quality of not diverging for the number of background events approaching zero. This is important because it ensures that there appears a maximum before one is cutting away all signal and background events. Fitting of the function (7.1) to the mass distribution, which is needed for calculation of N_s and N_b, is performed by a binned log-likelihood fit. For every bin a Poisson distribution is assumed. However, since the distribution is weighted to $\int L = 20fb^{-1}$ the entries are not integer. For this purpose, the Poisson distribution is modified by replacing $n!$ with $\Gamma(n + 1)$. Now, the distribution is defined for non-integer values as well. This modified likelihood function has been implemented in ROOT version 3.10 and is used in this study for fitting the function (7.1) to the mass distribution using a likelihood method. In the following the algorithm used to optimise the cuts will be described step by step:

1. The cuts listed in section 7.1 are implemented in the program.

2. In the beginning no cut is “optimised”. They are all set to the preselection values.

3. The first cut in the list is selected as “candidate” cut. For this cut, the user has to provide a list of test values.

4. For each test value, the following calculation is performed:

- The already "optimised" cuts are applied to the signal and background events.
- Then the "candidate" cut with the current input value is applied.
- The events, fulfilling the already "optimised" cuts and the "candidate" cut, are filled into a mass distribution.
- After all events have been processed, the function (7.1) is fitted to the distribution and the significance estimator S_K is calculated.

5. After significances for all test values have been calculated the "candidate" cut is set to the value which yields the highest significance S_K and is now considered as "opitimised" cut.

6. Until all cuts are processed, the next cut from the list is selected as "candidate" cut and item 4. and 5. are repeated.

7. Now every cut has an "optimised" value.

8. All cuts are processed again from item 3. to 6. with the current "candidate" cut being removed from the "optimised" cuts.

9. This is repeated until the "optimised" values of the cuts do not change any more.

7.4 Estimators of Significance

There are several methods to estimate the significance of the existence of a signal in the presence of background. Four commonly used definitions are applied in this study:

- The most commonly used estimator using event counting:

$$S_1 = \frac{N_S}{\sqrt{N_B}} \tag{7.5}$$

- An event counting estimator proposed by Bityukov and Krasnikov [30], defined as:

$$S_K = 2 \cdot (\sqrt{N_S + N_B} - \sqrt{N_B}) \tag{7.6}$$

- A likelihood-ratio estimator:

$$S_L = \sqrt{2 \cdot lnQ} \tag{7.7}$$
$$Q = \frac{L_{s+b}}{L_b} \tag{7.8}$$

- Applying Poisson statistics, estimator S_L can be transformed to:

$$S_{CL} = \sqrt{2 \cdot lnQ} \tag{7.9}$$
$$Q = \left(1 + \frac{N_s}{N_b}\right)^{N_s+N_b} e^{-N_s} \tag{7.10}$$

The two event counting estimators S_1 and S_K use the number of signal events N_s and the number of background N_b. Contrary to these methods the likelihood-ratio estimator S_L takes into account the shape of the distribution. It uses the maximum likelihood value obtained in the signal-plus-background fit, L_{s+b}, and the maximum likelihood from the background-only fit, L_b. A

likelihood estimator can also be used for event counting methods if one applies Poisson statistics. Q becomes the ratio between two Poisson distributions which leads to the definition of S_{CL}.
It has to be stressed that S_1 overestimates the significance in the case of small background event numbers, a case which is typical for the four-muon channel. Having a low background level it is recommended to use more sophisticated estimators like likelihood ratios. S_K also shows a more consistent behaviour in this case. By looking at equation (7.6) one easily can see that S_K does not diverge for N_b approaching zero. More details on significance estimators can be found in [29].

7.5 Results of the Cut Optimisation

A list of the cuts yielding the best significance is shown in table 7.1. It is a bit surprising that these values are quite loose. However, this effect can be understood by considering the number of selection quantities, used for this analysis. In figure 7.2 the mass distribution after applying the optimised cut can be seen. Comparing this distribution to figure 7.1 the background has been efficiently suppressed while keeping most of the signal events. The associated suppression rates for signal and background can be found in table 7.2.

Selection cut	p_{T,μ_1}	p_{T,μ_2}	p_{T,μ_3}	p_{T,μ_4}	Tracker isolation
Opt. value	27 GeV	22 GeV	12.2 GeV	3 GeV	11 GeV
Selection cut	$m_{Z_1,\text{down}}$	$m_{Z_1,\text{up}}$	$m_{Z_2,\text{down}}$	$m_{Z_2,\text{up}}$	$p_{\text{T,Higgs}}$
Opt. value	87.8 GeV	97.6 GeV	85.4 GeV	98.8 GeV	3.6 GeV

Table 7.1: The list of values for the selection cuts described in section 7.1, optimised for significance of the signal.

channel	suppression
$H \to ZZ^* \to 4\mu : m_H = 200$ GeV	34.3 $\pm$ 0.4 %
$ZZ^* \to 4\mu$	47.3 $\pm$ 0.3 %
$t\bar{t} \to 4\mu$	99.36 $\pm$ 0.11 %
$Zb\bar{b} \to 4\mu$	98.2 $\pm$ 0.4 %

Table 7.2: In this table the suppression rates of the optimised cuts and the statistical errors according to the number of generated events are shown for signal and background processes.

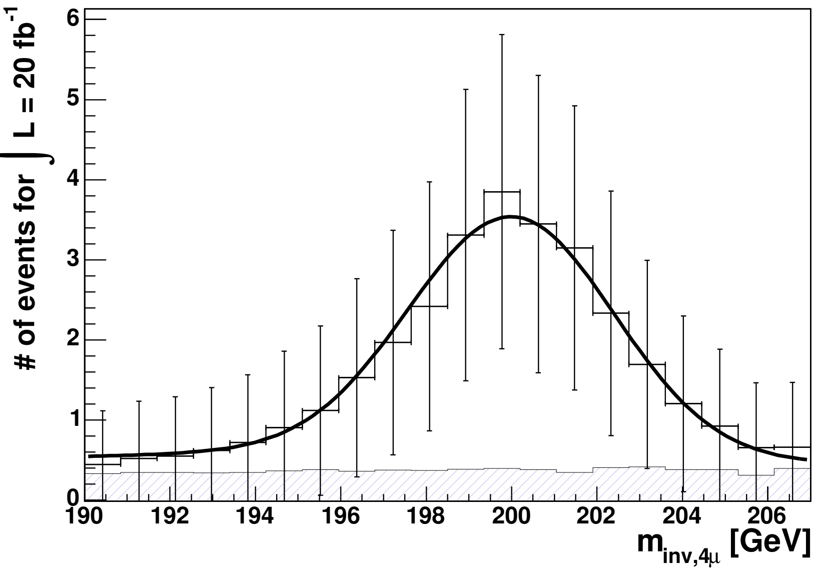

Figure 7.2: Reconstructed Higgs mass distribution of signal plus background events for $\int L = 20f^{-1}$ after applying optimised cuts. The background added to the distribution is marked in hatched blue. The error bars are the statistical errors for $\int L = 20f^{-1}$

The resulting significances calculated by the estimators introduced in the preceding section are listed in table 7.3. The significance achieved in this study is in good agreement with a recent study [23] that analysed the channel at a Higgs boson mass of 200 GeV. The lower significances can be completely explained by the low reconstruction efficiency (see section 6.2). Extrapolating the result to an event reconstruction efficiency of 80% obtained in [26] the significance estimators are within the statistical error of the results in [23]. The statistical error of this study can be neglected because of the large number of events analysed. The extrapolated results are shown in the second row in table 7.3. In this table the likelihood-ratio significance estimator S_L is not listed. This is due to the fact that the mass window, used in this study, is quite small. The reason for this is that the background is only plain in the range between 190 GeV and 208 GeV. As a result, the errors on the fits used for the likelihood-ratio are high and this spoils the value of the estimator S_L. However, the likelihood-ratio based Poisson estimator S_{CL}, which also has a good performance for small event numbers, can be used. This estimator needs the fit just for the calculation of N_s and N_b. By looking at figure 7.2 it is obvious that the fit is good enough to provide accurate values for N_s and N_b.

	N_S	N_B	S_K	S_1	S_{CL}
$\epsilon_{4\mu} = 66\%$	20.85	4.85	5.74	9.47	6.64
$\epsilon_{4\mu} = 80\%$	25.27	5.87	6.32	10.43	7.31

Table 7.3: The number of signal and background events N_S and N_B and different significance estimators after optimising the selection cuts. The estimator proposed by Bityukov and Krasnikov: S_K in equation (7.6), the simple event counting estimator (overestimating the significance): S_1 in equation (7.5) and the Poisson estimator: S_{CL} in equation (7.9).

Chapter 8

Determining the CP Eigenvalue of the Higgs Boson

In this chapter the CP Eigenvalue of the Higgs boson will be determined by using the distribution of the angle φ between the planes of the muon pairs (see figure 8.1), as described in section 2.4. A CP even Standard Model Higgs boson is confronted with the assumption of a CP odd pseudo-scalar Higgs boson and the probability to reject the pseudo-scalar hypothesis is calculated. It should be emphasized that in this analysis it is assumed that the signal of the Higgs boson is identified and its mass is determined.
The first section will offer a look at the distribution yielded by the Monte Carlo generator PYTHIA. Then the influence of detector simulation and event reconstruction will be discussed. Background is taken into account in the third section with a description of its suppression and the determination of the significance of the distributions. The last section deals with the evolution of probability to reject the pseudo-scalar hypothesis as a function of the integrated luminosity.

8.1 Distributions at the Level of Generated Events

About 500000 events for CP even and CP odd Higgs boson each have been produced with the Monte Carlo generator PYTHIA, in order to reproduce the theoretical distributions of the angle φ, equation (2.5) and (2.7). The resulting distributions, achieved by the analysis described in section 5.2.3, are shown in figure 8.2 and figure 8.3. The fitted theoretical functions proof the consistency with the implementation in PYTHIA.

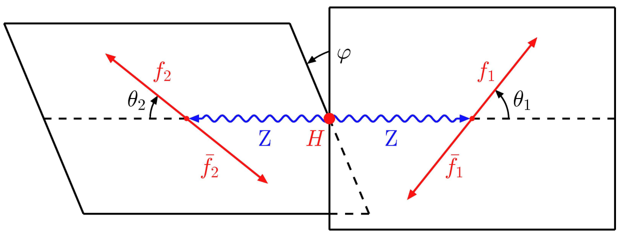

Figure 8.1: The definition of polar angles θ_1 and θ_2 and the angle φ for the decay $H \to ZZ \to f_1\overline{f_1}f_2\overline{f_2}$ in the rest frame of the Higgs boson.[6]

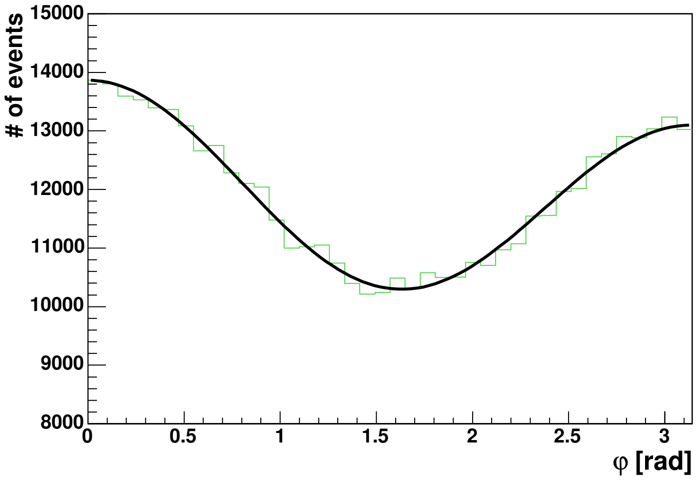

Figure 8.2: Distribution of the angle φ between the decay planes of the Z bosons for CP even Higgs sample with about 500000 generated events. The function $N(\varphi) = A + B\cos 2\varphi + C\cos\varphi$ with A, B and C as free parameters (compare with equation (equation 2.5)) is fitted to the distribution.

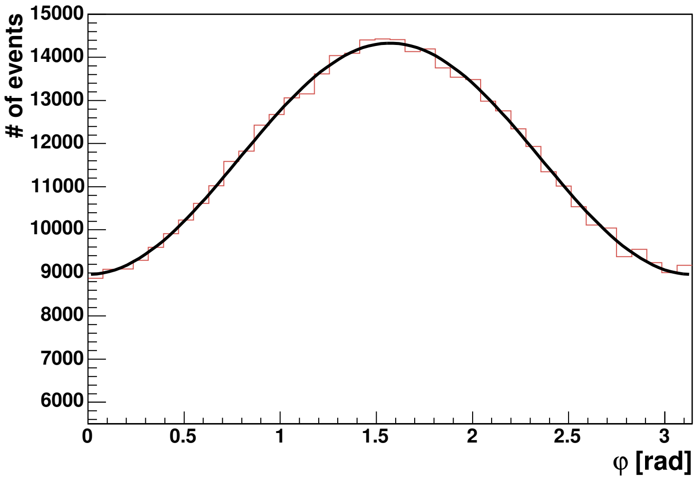

Figure 8.3: Distribution of the angle φ between the decay planes for CP odd Higgs sample with about 500000 generated events. The function $N(\varphi) = A + B\cos 2\varphi$ with A and B as free parameters (compare with equation (equation 2.7)) is fitted to the distribution.

8.1.1 Symmetry of the Distributions

The distribution for the CP odd Higgs boson is clearly symmetric around $\varphi = \pi/2$ as it is required by the theoretical dependency on φ defined in equation (2.7). A check is performed in figure 8.4 where the distribution shown in figure 8.3 is mirrored at $\varphi = \pi/2$. The difference between the left and right side of the distribution is due to statistical fluctuations, which is proven by calculating the χ^2 difference[1] between both sides.

[1] $\chi^2 = \sum_i \frac{(N^i_{left} - N^i_{right})^2}{(N^i_{left} + N^i_{right})}$

For the CP even Higgs on the other hand, the distribution on Monte Carlo generator level is clearly not symmetric around $\varphi = \pi/2$. The right side is lower than the left side (see figure 8.2). The reason for this is the $\cos\varphi$ term in the theoretical distribution in equation (2.5). The term depends on the polarisation of the Z bosons. For the reconstructed event, were the muons are in arbitrary order and not sorted like they are in the Monte Carlo generator sample, information about the polarisation of the Z bosons is not accessible. Because of the arbitrary order, the $\cos(\varphi)$ term of the differential distribution is “washed out”, the distribution for the reconstructed event only shows the $\cos(2\varphi)$ of equation (2.5). When using a Monte Carlo generator sample, this effect can be achieved by sorting the muons in random order. The resulting distribution is shown in figure 8.5. Symmetry of the distribution around $\varphi = \pi/2$ is proven in the same way like for the CP odd distribution by calculating the χ^2 (see figure 8.6).
The same symmetry holds for the background processes. They are not explicitly discussed here. The ZZ background turns out to be flat after selection cuts are applied while $t\bar{t}$ and $Zb\bar{b}$ will be suppressed almost completely. In the following analysis, the distribution will be mirrored at $\varphi = \pi/2$ and the right and left side are added up making use of the symmetry and doubling the statistics. The resulting distributions for CP odd and even Higgs samples are shown in figure 8.7.

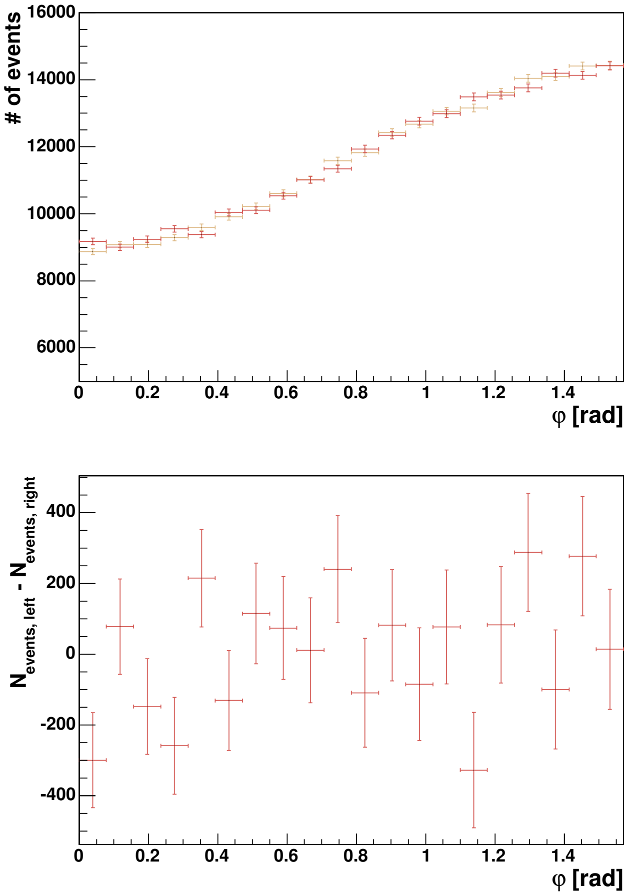

Figure 8.4: The distribution of φ at the level of generated events for CP odd Higgs, $m_{\text{Higgs}} = 200$ GeV, mirrored at $\varphi = \pi/2$, and below the difference between these distributions with error-bars corresponding to $\sigma = (\sigma_{\text{left}} + \sigma_{\text{right}})/\sqrt{2}$. The according χ^2 of the distributions is calculated to be 28.4 with $\text{ndf} = 20$, which corresponds to a probability of 10%. The distribution can be assumed to be symmetric around $\pi/2$.

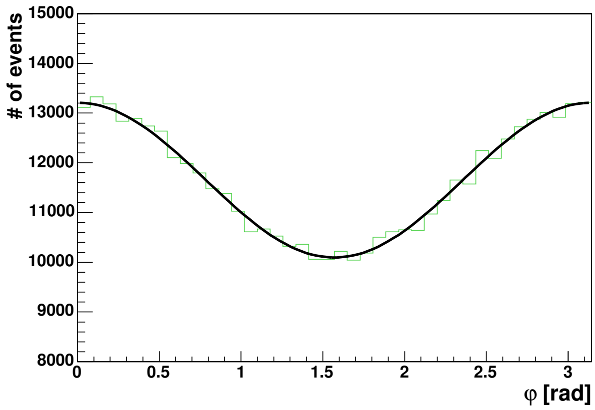

Figure 8.5: The same distribution as in figure 8.2 but this time with arbitrary order of the muons. The term proportional to $\cos\varphi$ is "washed out".

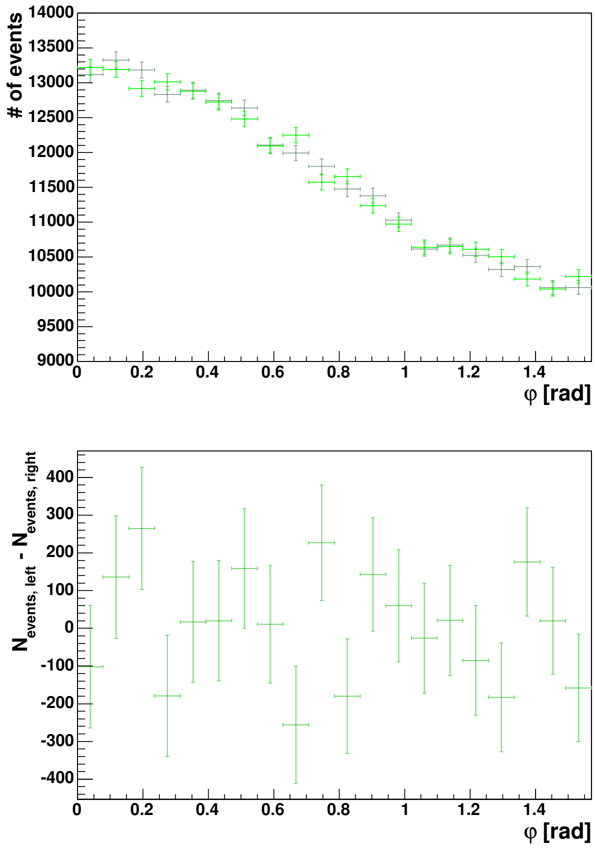

Figure 8.6: The distribution at the level of generated events for CP even Higgs, $m_{\text{Higgs}} = 200$ GeV, mirrored at $\varphi = \pi/2$, and below the difference between these distributions with error-bars corresponding to $\sigma = (\sigma_{\text{left}} + \sigma_{\text{right}})/\sqrt{2}$. The associated χ^2 of the distributions is calculated to be 18.2 with $\text{ndf} = 20$, which corresponds to a probability of 57.4%. The distribution can be assumed to be symmetric around $\pi/2$.

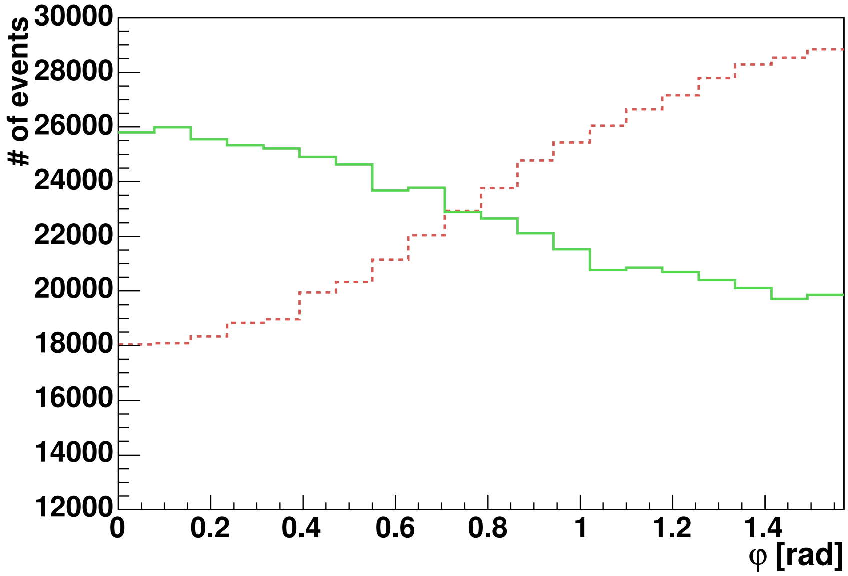

Figure 8.7: Distribution of the angle φ for CP even Higgs (green) and CP odd Higgs (dashed red) with $m_{\text{Higgs}} = 200$ GeV, mirrored at $\varphi = \pi/2$ and left and right side added. About 500000 Monte Carlo generator events each.

8.2 The Influence of Detector Simulation and Reconstruction

To perform the calculation of the angle φ with full detector simulation and reconstruction, it is important to estimate the influence of detector simulation and reconstruction on the distribution at the level of generated events (see figure 8.7). Two characteristics are important: The resolution of φ shown in figure 8.8 and the reconstruction efficiency as a function of φ, which can be seen in figure 8.9. The resolution of φ does not show any conspicuous behaviour. The standard deviation of the resolution, which would indicate a smearing of the reconstructed distribution of φ, is rather small at a value of 0.015 rad. The mean of the resolutions distribution is inside the statistical error defined by $\sigma/\sqrt{N}$, where N is the number of events. This suggests that there is no systematic shift of the distribution of φ as a result of detector simulation and reconstruction.
More concerning is the behaviour of the event reconstruction efficiency as a function of the angle φ. The efficiency drops significantly for $|\varphi| < 0.5$. This effect deforms the distribution of φ. It is still not understood. However, the CP even and CP odd signal as well as background events are affected in the same way.

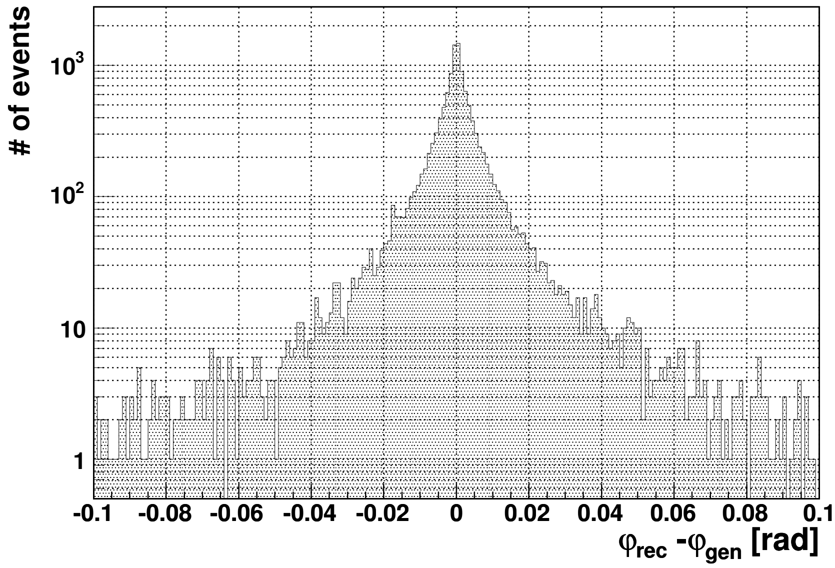

Figure 8.8: The resolution of the angle φ between the decay planes, defined as $\Delta\varphi = \varphi_{rec} - \varphi_{gen}$, can indicate a possible deformation of the distribution. A high standard deviation will result in a smearing of the distribution and a large mean would indicate a systematic shift of the distribution. The standard deviation is rather small, $\sigma = 0.015\,\mathrm{rad}$, and the mean is also not problematic.

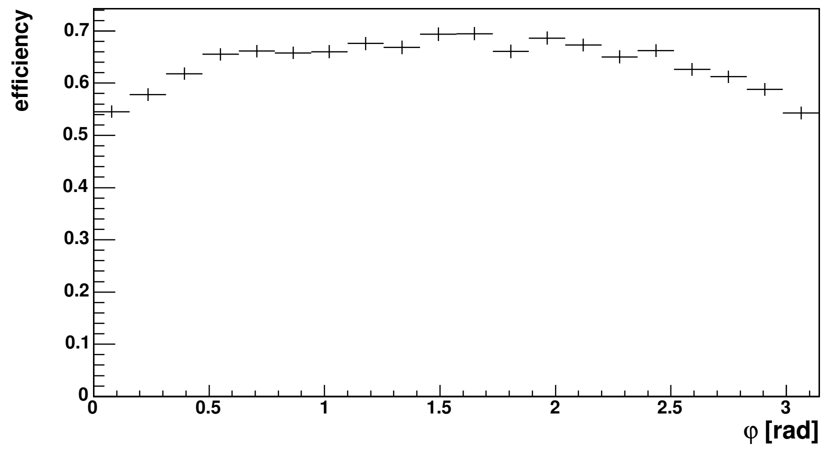

Figure 8.9: The efficiency, to reconstruct the event, as a function of φ. The error bars denote the statistical error of the event sample. The efficiency drops significantly for $|\varphi| < 0.5$. This effect is responsible for the deformed φ distribution after reconstruction.

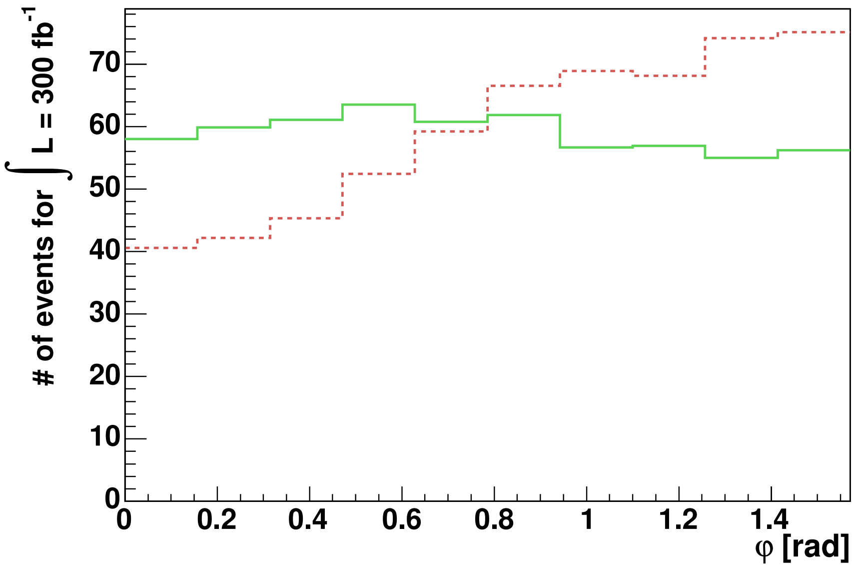

Figure 8.10: Distribution of the angle φ between the decay planes for events after full detector simulation and reconstruction with $m_{\text{Higgs}} = 200$ GeV. (CP even Higgs $\equiv$ green and CP odd Higgs $\equiv$ dashed red) .

8.3 The χ^2 Probability of the CP Odd Hypothesis

In this section, background events are added to the CP even and CP odd samples, all weighted according to their cross section to represent an integrated luminosity of 300 fb^{-1}. The resulting distributions before selection cuts are shown in figure 8.11. The CP odd Higgs distribution is understood as the curve of the confronting pseudo-scalar assumption to which the analysis data of the CP even Higgs sample is compared. The fact that the CP odd distribution is assumed to be a hypothesis and the CP even Higgs distribution presents a measurement is pointed out in figure 8.11: the CP odd distribution is shown as a line without error bars (dashed red line) while the CP even sample is plotted with error bars (green line). The χ^2 difference between the two distributions is calculated as an estimator of the probability of the CP odd hypothesis. All bins are summed up:

$$\chi^2 = \sum_i \frac{(N^i_{\text{odd}} - N^i_{\text{even}})^2}{N^i_{\text{even}}} \tag{8.1}$$

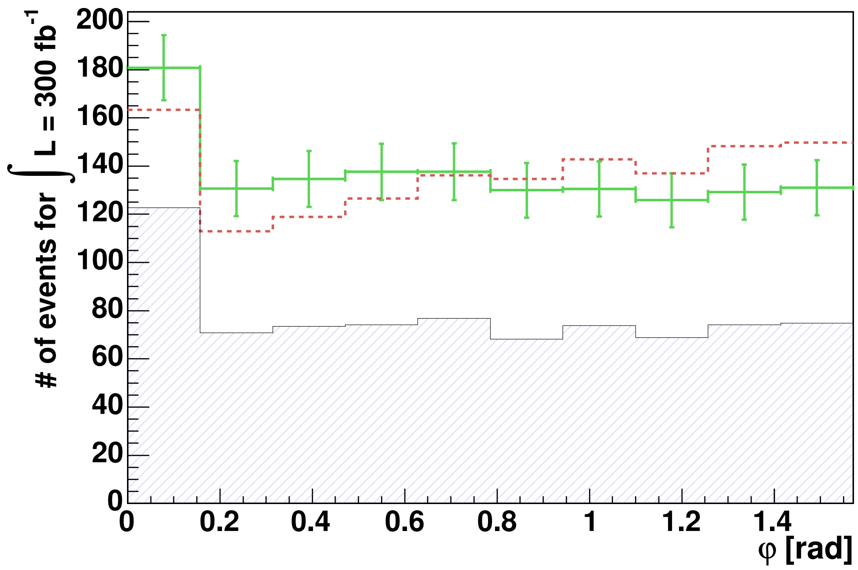

Figure 8.11: Reconstructed distribution of the angle φ between the decay planes with background added. $m_{\mathrm{Higgs}} = 200$ GeV and no selection cuts are applied. CP even Higgs $\equiv$ green, CP odd Higgs $\equiv$ dashed red and the total background $\equiv$ hatched blue. The error bars of the CP even distribution are the statistical errors for an integrated luminosity of $300 fb^{-1}$.

8.3.1 Optimising the Cuts

The same method of optimising selection cuts, introduced in the preceding chapter, can be used to maximise the χ^2 probability to exclude the CP odd assumption. Only this time χ^2 is used to rate the cut values.

Another difference has to be pointed out. Since for the analysis of the CP eigenvalue the Higgs boson signal is assumed to be identified and its mass determined, it is possible to apply cuts on the reconstructed Higgs boson mass in addition to the list of cuts already used in the preceding chapter. As an example for the cut optimisation process, the variation of χ^2 as a function of the cut on the transverse momentum of the reconstructed Higgs boson can be seen in figure 8.12.

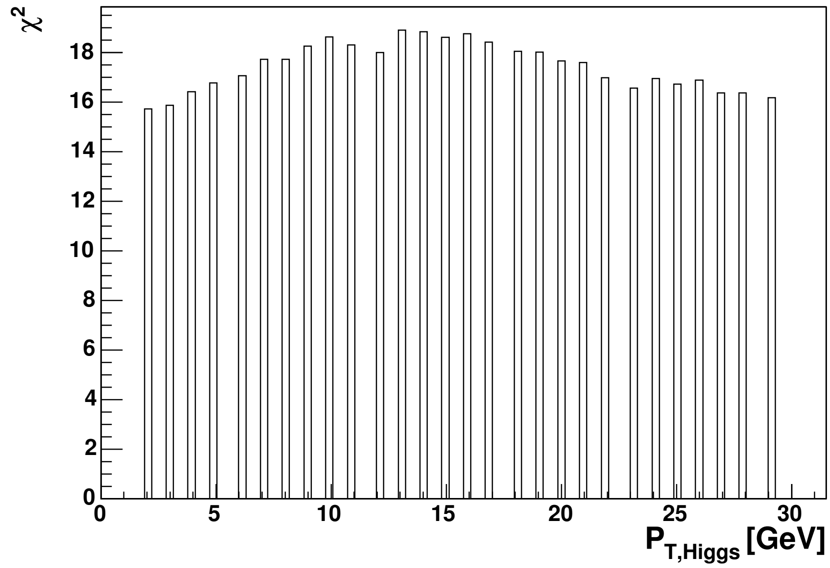

Figure 8.12: The χ^2 difference of the distributions for CP odd and CP even Higgs bosons as a function of the cut on the transverse momentum of the reconstructed Higgs boson.

Sel. cut	p_{T,μ_1}	p_{T,μ_2}	p_{T,μ_3}	p_{T,μ_4}	$p_{T,\text{Higgs}}$	p_T isolation
Opt. value	21 GeV	20.4 GeV	17 GeV	10.6 GeV	5.8 GeV	11.9
Sel. cut	$m_{Z_1,\text{down}}$	$m_{Z_1,\text{up}}$	$m_{Z_2,\text{down}}$	$m_{Z_2,\text{up}}$	$m_{\text{Higgs,down}}$	$m_{\text{Higgs,up}}$
Opt. value	86.7 GeV	98.3 GeV	81.7 GeV	102.4 GeV	191.1 GeV	206.6

Table 8.1: The list of values for the selection cuts, optimised for the χ^2 probability to reject the CP odd assumption.

8.3.2 The Distributions after Cut Optimisation

The optimised values for the selection cuts can be see in table 8.1. They are different from the values optimised for the signal observability. This is obvious since there were different criteria for the optimisation. The distributions, after optimised cuts have been applied, are shown in figure 8.13. Compared to figure 8.11 the background level is significantly lower. Furthermore, the peak at $\varphi = 0$ which is caused by the $t\bar{t}$ and $Zb\bar{b}$ background has been suppressed completely. The remaining ZZ background is flat. Comparing figure 8.13 with figure 8.10 one can see that the CP even and CP odd distributions have been recovered. The χ^2 difference between the CP even and CP odd distributions is equal to 26.4 with $\mathrm{ndf} = 20$, which corresponds to a χ^2 probability of 0.33 %.

In this study the χ^2 probability P_{χ^2} corresponds to the probability that the CP odd assumption is correct, $(1 - P_{\chi^2})$ is the probability that the CP odd hypothesis is rejected. P_{χ^2} is calculated using an incomplete gamma function $P(a, x)$, where $a = \mathrm{ndf}/2$ and $x = \chi^2/2$. ndf is the number of degrees of freedom, which in this case is 10, the number of bins. The function is implemented in the `TMath` class of ROOT [19].

Without taking into account other information than the angle φ, the CP odd hypothesis can be excluded during LHC operating time using only the $H \rightarrow 4\mu$ channel. A further going examination will follow in the next section.

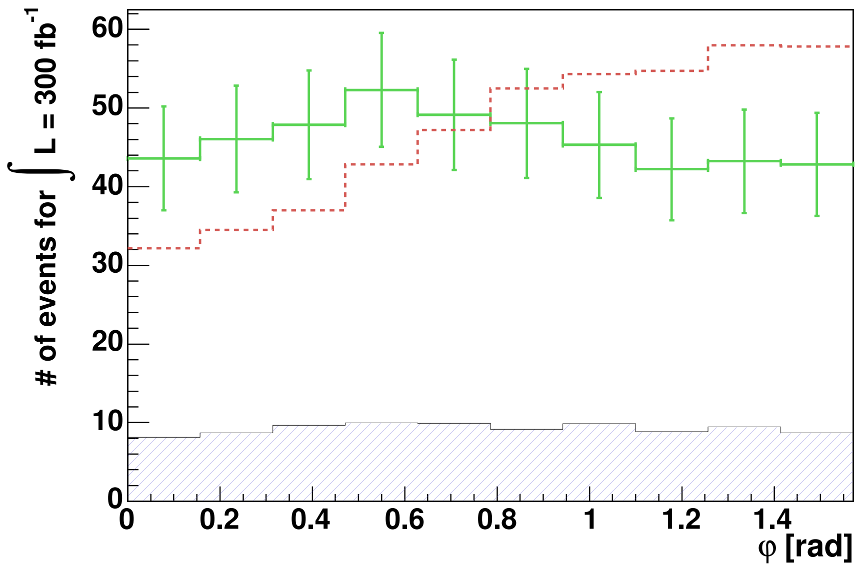

Figure 8.13: Distribution of the angle φ between the decay planes with background added. $m_{\text{Higgs}} = 200$ GeV and optimised cuts are applied. CP even Higgs $\equiv$ green, CP odd Higgs $\equiv$ dashed red and the total background $\equiv$ hatched blue. The error bars of the CP even distribution are the statistical errors for an integrated luminosity of $300 fb^{-1}$.

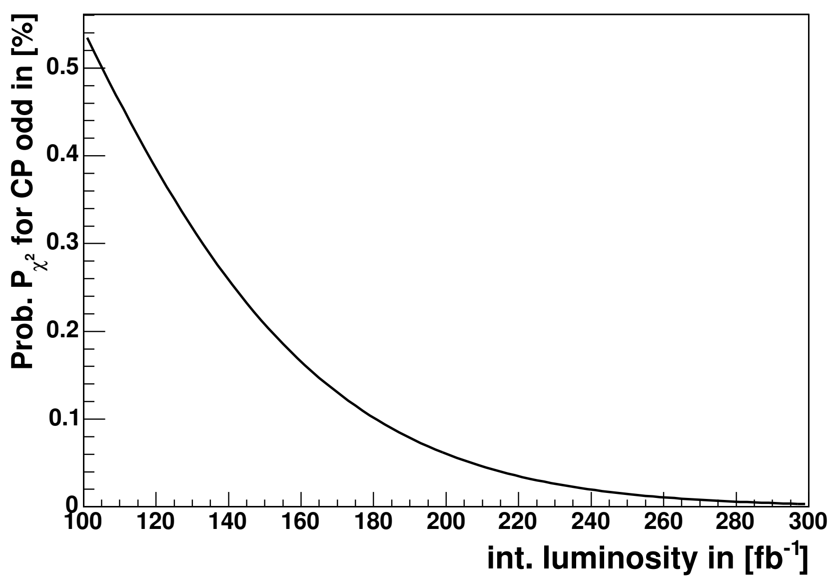

Figure 8.14: Probability P_{χ^2}, that the CP odd hypothesis is correct, as a function of the integrated luminosity. Details on the meaning of P_{χ^2} can be found in the text.

8.4 χ^2 Probability as a Function of the Integrated Luminosity

Since the χ^2 difference between the CP even and CP odd distribution is defined as $\chi^2 = \sum_i \frac{(N^i_{odd} - N^i_{even})^2}{N^i_{even}}$, it is anti-proportional to the number N_{even} of CP even signal plus background events. This number is obviously proportional to the integrated luminosity of the LHC. The probability for the χ^2 difference is calculated like described in the preceding chapter. Its dependency on the integrated luminosity of the LHC is shown in figure 8.14. Here the anti-proportional dependency between χ^2 and the integrated luminosity is used to extrapolate the value for the probability determined in section 8.3.2 to other integrated luminosities. It has to be stressed, that the low reconstruction efficiency for muons in ORCA version 7.6.1 of course has a direct impact on the calculated probability. Assuming reconstruction efficiencies reached in [26] about 15 % less integrated luminosity will be required.

The results of the study demonstrate that the exclusion of the CP odd hypothesis is possible at the CMS detector during LHC operation time, only taking into account the distribution of the angle φ. In theoretical studies on this subject [4] observables have been proposed that take the full angular distribution of the muons into account. These observables are expected to improve the sensitivity of CP eigenvalue determination significantly. Using the analysis setup developed for this study (see appendix A), additional observables can easily be integrated in the analysis.

Chapter 9

Conclusion and Outlook

This study addresses the "gold plated channel" $H \rightarrow ZZ \rightarrow 4\mu$ at a Higgs boson mass of 200 GeV. Full detector simulated events for this channel and its background have been produced. On the produced signal and background samples detector studies and the determination of the Higgs discovery potential at the CMS detector at the LHC have been performed. Furthermore, an analysis that utilises the angle φ between the decay planes of the two Z to determine the CP eigenvalue of the Higgs boson has been carried out. The analyses applied in this study were based on selection cuts.
In order to have small statistical errors in the analysis, about 100000 signal and background events were processed through full detector simulation. The events were processed on the computing facilities at the GridKa cluster at the Forschungszentrum Karlsruhe and at the EKP-cluster at the University of Karlsruhe, using CMS simulation and reconstruction software. The enormous effort of full detector simulation had to be made in order to achieve a realistic analysis.
The Analysis of the channel $H \rightarrow ZZ \rightarrow 4\mu$ has been implemented in the object-oriented C++ toolkit PAX. Therefore, it is possible to make the analysis code independent of the CMS specific reconstruction code. Furthermore, additional functionality can easily be added to the analysis. In order to optimise the cuts for the analysis of signal observability, a method has been implemented in ROOT, which optimises the selection cuts, taking the significance as a criterion.
During determination of the event reconstruction efficiency it turned out that in the preliminary version of the reconstruction software (ORCA version 7.6.1), used for this study, the reconstruction efficiency for one muon is significantly lower (about 90 %) than in a recent study[26] and specified in the Tracker Technical Design Report[28] (about 97 %). The effect has shown to be even worse for events with pileup. Therefore, the event samples used for this study were produced without pileup.
To be able to compare generated and reconstructed quantities, a matching of the muons via simulated and reconstructed track hits has been performed. The lower reconstruction efficiency had no influence on the detector resolution. It is in good agreement with the Tracker Technical Design Report and [26, 25].
The significance of the observability of the signal for an integrated luminosity of $20\ \mathrm{fb}^{-1}$ was determined to be $S_{cL} = 6.64$. Assuming a reconstruction efficiency achieved in [26] the significance is $S_{cL} = 7.31$. The results are within the statistical error of a recent study [23]. The results are summarised in table 7.3.
The CP eigenvalue has been determined by confronting the CP even Higgs boson with a pseudoscalar CP odd Higgs. The distributions of φ for both cases with full detector simulated events were reconstructed. The distribution for the CP odd case was assumed to be a theoretical distribution while the CP even events were treated as real detector data. The χ^2 probability, to verify the CP

odd hypothesis, has been calculated. For an integrated luminosity of $300\ \mathrm{fb}^{-1}$, the probability was found to be about 0.36 %. The CP odd assumption could be rejected. The distribution of this χ^2 probability as a function of the integrated luminosity can be found in figure 8.14. If one assumes a reconstruction efficiency achieved in [26] about 15 % less integrated luminosity will be required.

Some tasks remain for the future:

- Both analyses, estimation of the signal observability and determination of the CP eigenvalue, have to be redone with a later version of the CMS reconstruction software, where muon reconstruction is fully supported.
- When the problem of lower reconstruction efficiency for events with pileup is fixed, the analysis has to be redone with events including pileup.
- The effect of muon reconstruction on the distribution of φ has to be qualified and a more sophisticated estimator of the significance of the CP even hypothesis, e.g. a likelihood-ratio, should be used.
- Improved observables for CP eigenvalue determination, which take into account the whole angular distribution of the muons, have been proposed. Implementing these observables in the analysis at hand will increase the significance.
- Up to know, the event selection is based on cuts. Likelihood methods or neural networks are expected to give a better performance.

Appendix A

Analysis Setup

This appendix will introduce the analysis that was developed for this study. PAX [20] was chosen as a framework for the analysis since it is an object-oriented software project which offers the possibility to easily expand the analysis with additional functionality and apply the analysis code to different sources of data. ORCA [18] is used for accessing the data samples and reconstructing the muons while ROOT [19] is utilised for histogramming and storage of the results. How this interaction is handled and which features are implemented in the analysis will be explained in the following sections.

A.1 Overview - Structure

The structure of the analysis is shown in figure A.1. The *Observer* class controls the program flow. It inherits from the ORCA class `Observer<G3EventProxy*>`. This class calls the "user analysis", implemented in the function `analysis(G3EventProxy* ev)`, at the arrival of a new event. The *Observer* has an instance of the class *Filler*, and a certain number of instances of the *Analyses* class. The *Filler* reconstructs the muons using ORCA code and fills them into *PaxEventInterprets* that are owned by the *Observer*. These *PaxEventInterprets* are the input for the *Analysis* class: one as data input that has to be reconstructed, and one as reference, to be compared with the reconstructed event. Each instance of the *Analysis* class contains an instance of the class *PaxAnalysisFrame* which handles the bookkeeping for histograms, ROOT trees, input histograms and constants. Furthermore, for each event analysed, the *Analysis* initialises an instance of the class *EventClassH4Mu*, which is the heart of the analysis and provides all the functionality needed for the event reconstruction and analysis. The functions for event reconstruction, matching and comparing with a reference event and analysis of the event are called for each input event by the *Analysis* instance. Details about the classes of the analysis and their functionality are given in the following subsections.

A.2 The Observer Class

The Observer initialises the different *Analyses* and a *Filler* that fills the event data into *PaxEventInterprets*. In this study the input data is read from ORCA databases. In order to access the database, the *Observer* has to adapt to the ORCA used principle of "Event Driven Notification". This is done by inheriting from the ORCA class `Observer<G3EventProxy*>`. This class manages the iteration over all events and for each event starts the "user analysis" contained in the function `analysis(G3EventProxy* ev)`.

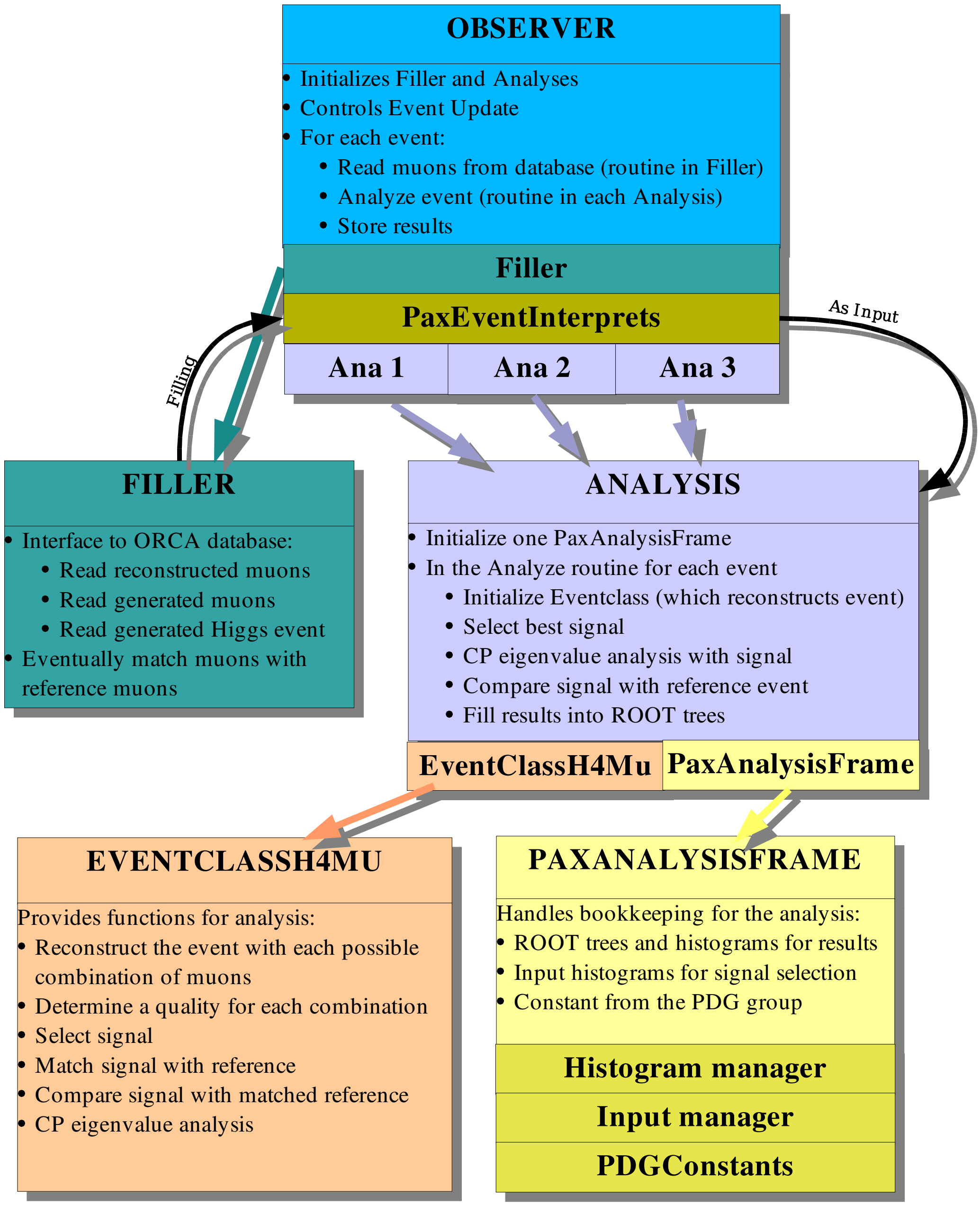

Figure A.1: An overview of the structure of the analysis.

However, the analysis is not restricted to ORCA. Any source of data that provides the necessary information, i.e. reconstructed muons, can be used. The only thing needed is a *Filler* that fills the event information into *PaxEventInterprets*. The easiest way is to use a `.pax` file where the *PaxEventInterprets* can just be read in. In section 8.1 this was done to access Monte Carlo generated events. The files in HEPEVT[1] standared were transformed to `.pax` files and then analysed.

A.3 The Filler Class

The *Filler* is an interface between the event samples, in this case ORCA databases, and the *Analyses* which need *PaxEventInterprets* as input. The *Filler* used in this analysis accesses three different levels of event data, stored in ORCA databases:

- Generated Event data: The decay tree of a $H \rightarrow ZZ \rightarrow 4\mu$ event, as it is produced by the Monte Carlo event generator.
- Generated Muons: The final state muons as they are generated by the event generator
- Reconstructed Muons: Muons as they are reconstructed after full detector simulation by the *L3MuonReconstructor*, implemented in ORCA. .

How reconstructed and generated muons are accessed through ORCA routines is explained in section A.6. With the objects returned by the ORCA routines the kinematics of the muons can be accessed. However, in this study also the energy and transverse momentum deposit in an area around the muons is of interest. With the aid of these quantities, events containing non-isolated muons can be excluded, which is important to suppress $t\bar{t}$ and $Zb\bar{b}$ background.

Muon Isolation Package

In order to determine the energy and transverse momentum deposit around the muons the *Muon Isolation* package implemented in ORCA has been used. Tracker isolation and calorimeter isolation were applied in this study. The packages search for tracks or energy clusters in a cone $\Delta R = \sqrt{\Delta\eta^2 + \Delta\phi^2}$ around the muon and add up p_T and E_T. Different values of the cone sizes are defined in the packages. The optimal cone sizes for an analysis of the channel $H \rightarrow 4\mu$ have been determined in a recent study [26]. For tracker isolation a cone with $\Delta R = 0.24$ was found to be the optimal choice whereas for calorimeter isolation a wider cone size $\Delta R = 0.45$ was chosen.

Matching via Simulated and Reconstructed Track Hits

Another feature of the *Filler* used in this analysis is the possibility to match the reconstructed muons with generated muons provided by a reference *PaxEventInterpret* using simulated and reconstructed hits in the detector:

- The reconstructed muons provide a pointer to their reconstructed track.
- This reconstructed track is matched to the simulated tracks of the event by comparing the reconstructed hits with the simulated hits.
- The matched simulated track provides a pointer to the according generated particle. The momentum of this generated particle is compared to the momenta of the generated muons provided by the reference event.

[1] High Energy Physics event

- If one of the reference muons fits, the two muons are matched.
- This is done for all reconstructed muons.

In recent studies [25, 26] a matching in ϕ and θ was performed. The method used in this analysis is more accurate. Particles that are not processed with this method are matched by a minimum angular difference later in the analysis.

A.4 The Analysis Class

The *Analysis* class is implemented in a way that offers the possibility to reconstruct the "candidate" $H \rightarrow 4\mu$ event and compare it with a reference event. The function `analyze(PaxEventInterpret* RecPart, PaxEventInterpret* RefEvent)`, in which the methods for reconstruction, analysis, matching and comparison are called, has two input parameters:

- The reconstructed particles, in this case the reconstructed muons in the event.
- The reference event, containing the Higgs and Z bosons and the muons, taken from event generator data or reconstructed before in a different way.

Within this function the event is reconstructed, the resulting particles are matched with the particles in the reference event and finally the quantities of the matched particles are compared and the results filled into ROOT trees. E.g. one can compare the reconstructed Z boson mass for full detector-simulated events and the associated generated events. In the analysis at hand comparisons at three different levels of event data have been implemented:

- Between events reconstructed from full detector-simulated muons and events reconstructed from generated muons. At this level detector resolution studies are made.
- Between events reconstructed from generated muons and Monte Carlo generator events. Here the change of quantities due to initial state radiation can be examined.
- Between events reconstructed from full detector-simulated and reconstructed muons and Monte Carlo generator events where one can see the difference between the skeleton generator event $H \rightarrow 4\mu$ and the event reconstructed from full detector simulated and reconstructed data.

For each of these comparison levels a separate instance of the *Analysis* class is needed. More analyses, i.e. comparing reconstructed events with events reconstructed in another way can be added. The *Analysis* class contains an instance of the class *PaxAnalysisFrame*, which handles the bookkeeping of ROOT trees, histograms, input histograms and constants. The functions for event reconstruction, matching, comparison and furthergoing analyses are provided by the class *EventClassH4Mu*, which is instantiated for each event.

A.5 The Class EventClassH4Mu

This class provides the functions needed for event reconstruction and analysis. It inherits from the *PaxEventClass* which implements the basic functionality of the reconstruction of an event.
During initialisation, the function `reconstruct()` is called. It trys to build Z bosons and a

Higgs boson from the muons given as input. The reconstruction of the Z and Higgs bosons is handled by an algorithm defined in the class *PaxUserAlgorithm*. Every possible combination of the muons, that results in an $H \rightarrow 4\mu$ event is stored in a *PaxEventInterpret*. These interpretations are then stored in a `map`. In fact, the class *PaxEventClass* is a `map`, i.e. it inherits from the `map` of the Standard Template Library.
The *PaxEventInterprets* stored in the list are now rated by a likelihood estimation. Reconstructed quantities like the Z boson masses and the transverse momenta of the muons are compared with reference histograms and the result of this comparison is assigned to the *PaxEventInterpret* as quality of the interpretation. The *PaxEventInterpret* with the highest quality is chosen as the signal.
Now, the particles in this signal *PaxEventInterpret* can be matched with the particles of a reference event. Particles that are not already matched with the method described in subsection 5.2.3 are matched via a minimum angular difference criterion.
In the function `compare()` quantities of the matched particles are compared and the results filled into ROOT trees. In the function `decayPlaneAnalysis(PaxEventInterpret* Ref)` the calculation of the angle φ between the decay planes of the Z bosons is performed for the signal and the according reference.

A.6 Routines to Access ORCA Databases

In order to get the information needed for this analysis, the *Filler* class has to access the Monte Carlo generated event as well as the reconstructed objects both stored in the ORCA database:
The generated event is read using the *HepEventG3EventProxyReader* implemented in COBRA. With the aid of this reader the generated event is filled in a *RawHepEvent*. In this data structure all particles of the event are stored as *RawHepEventParticles*. The *RawHepEventParticles* contain all the informations needed to fill *PaxEventInterprets*.
Reconstructed muons are accessed by an *AutoRecCollection*. at initialisation of the *AutoRecCollection* a reconstruction technique is set. In this analysis the *L3MuonReconstructor*, which is based on the reconstructor used in the trigger, is used since a standalone reconstructor was not available in ORCA version 7.6.1. The reconstructed muons stored in the *AutoRecCollection* can be accessed with a pointer to a list of *RecTracks*. The *RecTracks* provide all the necessary informations.
The muon reconstruction efficiency reached with ORCA version 7.6.1 was significantly lower than in a recent study [26] or specified in the Tracker Technical Design Report [28]. In order to achieve a better performance, two options for reconstruction were set in the `.orcarc` steering file. The level-1 trigger sensitivity region was widened from $|\eta| < 2.1$ to $|\eta| < 2.4$ [1] and the quality requirement for a muon candidate to be accepted was lowered [2]. More information on muon reconstruction in ORCA can be found in [31].

A.7 Reference Histograms for the Likelihood Rating

Input histograms are used as a reference for the likelihood estimator of a *PaxEventInterprets* (see the preceding subsection). The function `selectSignalUsingRef()` of the *EventClassH4Mu* offers the possibility to construct these input histograms from ORCA databases. It is required that the reconstructed muons have been matched to the generated muons like explained in section 5.2.3. With this information, the function `selectSignalUsingRef()` can select the one

[1] by setting the option `CSCTrigger:twentyDegreeSubSectors=1`.
[2] by setting the option `CSCTrackFinder:lowQualityFlag=4`.

event interpretation as signal, which has the same combination of muons like the original Monte Carlo generated event. In this way perfect event reconstruction is simulated and the resulting histograms of reconstructed quantities can be used as reference for the realistic analysis. Of course, in a realistic analysis, no generator data of the event may be used.

Bibliography

[1] David Griffith: “Introduction to Elementary Particles”, John Wiley and Sons 1987

[2] Chris Quigg: “Gauge Theories of the Strong, Weak and Elekromagnetic Interactions” Frontiers in Physics, Lecture Note Series 56

[3] J. F. Gunion, H. E. Haber, G. Kane, S. Dawson: “The Higgs Hunter’s Guide”, Frontiers in Physics, Lecture Note Series 80

[4] C.P. Buszello, I. Fleck, P. Marquard, J.J van der Bij: “Prospective Analysis of Spin and CP-sensitive Variables in $H \to ZZ \to l_1^+ l_1^- l_2^+ l_2^-$ with ATLAS”, hep-ph/0212396

[5] Torsten Arens und L. H. Sehgal: “Energy Spectra and Energy Correlations in the Decay $H \to ZZ \to \mu^+\mu^-\mu^+\mu^-$”, hep-ph/9409396

[6] S.Y. Choi, D.J. Miller, M.M. Mühlleitner and P.M. Zerwas: “Identifying the Higgs Spin and Parity in Decays to Z Pairs”, hep-ph/021007

[7] Robert V. Harlander: “Recent Theoretical Progress on Higgs Production at Hadron Colliders”, Talk given at HCP2002, Karlsruhe, Germany

[8] M. Spira, A. Djouani, D. Graudenz and P. M. Zerwas, Nucl. Phys. B453(1995) 17

[9] A. Djouani: “Higgs Phenomenology: A Short Review”, hep-ph/9612361

[10] M. Spira, A. Djouani, J. Kalinowski: “HDECAY: a Program for Higgs Boson Decays in the Standard Model and its Supersymmetric Extension”, hep-ph/9704448

[11] T. Sjöstrand, P. Edén, C. Friberg, L. Lönnblad, G. Miu, S. Mrenna and E. Norrbin, Computer Physics Commun. **135** (2001) 238. `http://www.thep.lu.se/˜torbjorn/Pythia.html`

[12] CMS Computing Production: `http://cmsdoc.cern.ch/cms/production/www/html/general/index.html`

[13] “CompHEP - a package for evaluation of Feynman diagrams and integration over multi-particle phase space”, Feb. 2000, hep-ph/9908288 v2

[14] Object Oriented Simulation for CMS Analysis and Reconstruction: `http://cmsdoc.cern.ch/OSCAR/`

[15] S.Agostinelli et al.: “Geant4 - A Simulation Toolkit”, Nuclear Instruments and Methods A **506** (2003) 250-303.

`http://wwwasd.web.cern.ch/wwwasd/geant4/geant4.html`

[16] "CMS Simulation Package CMSIM", User Guide and Reference Manual in http://cmsdoc.cern.ch/cmsim/cmsim.html

[17] COBRA homepage http://cobra.web.cern.ch/cobra/

[18] ORCA homepage http://cmsdoc.cern.ch/orca

[19] R. Brun and F. Rademakers: "ROOT - An Object Oriented Data Analysis Framework 3.10" see also http://root.cern.ch

[20] M. Erdmann *et al.*: "Physics analysis expert PAX: First applications", proceedings of the talk given at the International Conference on Computing in High Energy and Nuclear Physics, CHEP03, La Jolla, USA (2003), [arXiv:physics/0306085]. http://pax.home.cern.ch

[21] Pool of Persisten Objects for LHC: http://pool.cern.ch/

[22] Marc Hohlfeld: "On the determination of Higgs parameters in the ATLAS experiment at the LHC", ATL-PHYS-2001-004 (2001)

[23] M.Sani, V. Ciulli: "Search for the Standard Model Higgs boson in four-muon final state with the CMS detector", CMS Internal Note 2003/005

[24] Joanna Weng: "Analyse des Kanals $H \to 4\mu$ in der objektorientierten Softwareumgebung von CMS", Diplomathesis, University of Karlsruhe (2003)

[25] Debora Miksat: "Studien zur Suche nach dem Higgs-Boson in simulierten pp-Kollisionen in der objektorientierten Softwareumgebung des CMS-Experiments am LHC für den Kanal $H \to ZZ* \to 4\mu$", Diplomathesis, University of Karlsruhe (2004)

[26] Valeria Bartsch: "Simulation of silicon sensors and study of the Higgs decay $H \to ZZ^* \to 4\mu$ for CMS (LHC)", PhD thesis, University of Karlsruhe (2003), IEKP-KA/2003-026

[27] "Level-1 Trigger Technical Design Report", 15. Dezember 2000, CERN/LHCC 2000-038

[28] The CMS Collaboration, The Tracker Project, Technical Design Report, CERN/LHCC 98-6, 1998

[29] V. Bartsch, G. Quast: "Expected signal observability at future experiments", CMS IN-2003/039

[30] S. I. Bityukov, N. V. Krasikov: "On observability of signal over background", NIM A452:518- 524, 2000

[31] Rick Wilkinson: "Muon Software Tutorial", Caltech, http://webcms.ba.infn.it/cms-software/MuonTutorial.pdf

Deutsche Zusammenfassung

Das Standardmodell der Teilchenphysik beschreibt die elementaren Teilchen und ihre fundamentalen Wechselwirkungen. Es ist allgemein akzeptiert und in vielen Präzissionsmessungen bestätigt worden. Ein wesentlicher Bestandteil verschließt sich allerdings bis heute der experimentellen Überprüfung: der Higgs Sektor. Im Standardmodell werden die Massen der elementaren Fermionen und Vektorbosonen durch den sogenannten Higgsmechanismus erzeugt. Dieser Mechanismus sagt ein neues Teilchen voraus, das Higgs-Boson.
Die Suche nach dem Higgs-Boson ist mit Sicherheit eines der aufregendsten Gebiete der modernen Teilchenphysik. A priori ist die Masse des Higgs-Bosons ein freier Parameter. Sie kann allerdings aufgrund von Messungen und theoretischen Vorhersagen auf einen Bereich zwischen 100 und 200 GeV beschränkt werden. Neben dem Standardmodell gibt es erweiterte Modelle, beispielsweise supersymmetrische Modelle, die einen komplexeren Higgs Sektor voraussagen. Durch die Messung ihrer Quantenzahlen lassen sich die Higgs-Bosonen der erweiterten Modelle und des Standardmodells unterscheiden.
Um die Fragen nach der Entstehung der Masse zu klären, wird zurzeit am CERN ein neuer Beschleuniger gebaut. Der Proton-Proton Beschleuniger LHC wird eine Schwerpunktsenergie von 14 TeV erreichen und ermöglicht hiermit die Suche nach dem Higgs-Boson im Bereich von 100 GeV bis 1 TeV. Der CMS Detektor, einer von vier Detektoren am LHC, ist konzipiert, um das Higgs-Boson zu entdecken. Einer der wichtigsten Zerfallskanäle hierfür ist der Kanal $H \rightarrow ZZ \rightarrow 4\mu$. Er zeichnet sich durch seinen Endzustand mit vier isolierten Myonen aus und ermöglicht den Nachweis des Higgs-Bosons fast im gesamten Massenbereich.
In der vorliegenden Studie wird der Zerfallskanal $H \rightarrow ZZ \rightarrow 4\mu$ für eine Higgs-Masse von 200 GeV betrachtet. Für die Analyse wurden Ereignisse nach voller Detektorsimulation rekonstruiert. Es handelt sich also um eine wirklichkeitsnahe Analyse, die bereits Rekonstruktionssoftware des zukünftigen Experiments verwendet. Die Sudie kann in zwei Teile unterteilt werden. Teil 1 befasst sich mit der Nachweiswahrscheinlichkeit des Higgs-Bosons für eine Higgs-Masse von 200 GeV. Teil 2 konzentriert sich auf die Bestimmung des CP-Eigenwertes mit Hilfe der Winkelverteilungen der vier Myonen. Die Higgs-Masse von 200 GeV wurde gewählt, da für diese Masse Zerfälle von CP-geraden und CP-ungeraden Higgs-Bosonen simuliert werden konnten.
Kapitel 1 stellt einen Überblick über das Standardmodell dar. Besonderes Augenmerk wird hierbei auf lokale Eichinvarianz und den Higgsmechnismus gelegt. Am Beispiel der QED wird das Prinzip der lokalen Eichinvarianz beschrieben. Durch dieses Prinzip lässt sich die elektromagnetische Wechselwirkung aus der Lagrangedichte eines freien Dirac-Teilchens herleiten. Spontane Symmetriebrechung wird am Bild eines skalaren Feldes erläutert. Die Anwendung dieser Prinzipien auf die elektroschwache $SU(2)_L \otimes U(1)$ Symmetrie führt dann zum Higgsmechanismus. Auf erweiterte Modelle jenseits des Standardmodells wird am Ende des Kapitels eingegangen.
Kapitel 2 behandelt die Physik des Higgs-Bosons am LHC. Zunächst werden die verschiedenen Produktions- und Zerfallsprozesse erklärt. Im Anschluss daran wird detaillierter auf den Kanal $H \rightarrow ZZ \rightarrow 4\mu$ und seine wichtigsten Untergrundprozesse, $ZZ \rightarrow 4\mu$, $t\bar{t} \rightarrow 4\mu + X$ und

$Zb\bar{b} \rightarrow 4\mu + X$ eingegangen. Die Verwendung des Winkels φ zwischen den Zerfallsebenen der Z Bosonen zur Bestimmung des CP-Eigenwertes des Higgs Bosons wird am Ende des Kapitels erläutert. Im dritten Kapitel wird der CMS Detektor am LHC vorgestellt und seine Komponenten werden erklärt. Zunächst werden wichtige Eckdaten des LHC genannt: Eine Schwerpunktsenergie von 14 TeV, Luminosität von $\mathcal{L} = 10^{34}\,\mathrm{cm}^{-2}s^{-1}$ bei hoher und $\mathcal{L} = 2 \cdot 10^{33}\,\mathrm{cm}^{-2}s^{-1}$ bei niedriger Luminosität sowie 25 ns Abstand zwischen den einzelnen Ereignissen. Nun wird auf die einzelnen Komponenten des CMS Detektors eingegangen. Das Myonsystem hat hierbei einen besonderen Stellenwert. Ein effizienter Nachweis und eine gute Detektorauflösung für Myonen sind unverzichtbar.

Vor der Analyse müssen zunächst die Signal- und Untergrundereignisse generiert und ihr Verhalten im Detektor simuliert werden. Hierin besteht ein wesentlicher Teil der Arbeit. Die hierfür benötige Software wird in Kapitel 4 vorgestellt.

Die Simulation und Analyse der Ereignisse werden in Kapitel 5 geschildert. Zunächst wird der Monte Carlo Generator PYTHIA[11] verwendet, um Signal- und Untergrundereignisse zu generieren. Hierbei wird eine Vorauswahl der Ereignisse durchgeführt. Die generierten Ereignisse werden nun in der Detektorsimulation CMSIM/GEANT3 verarbeitet und die Ergebnisse mit Hilfe von ORCA digitalisiert und in einem CMS spezifischen Datenformat gespeichert. Für diese Studie wurden jeweils 20000 Ereignisse für den Signalprozess $H \rightarrow 4\mu$ mit CP-Eigenwert gerade und ungerade sowie 2200 $Zb\bar{b}$, 13000 $t\bar{t}$ und 40000 ZZ Untergrundereignisse mit der vollen Detektorsimulation produziert. Die Simulation der Ereignisse stellt hohe Anforderungen an Rechenzeit und Speicherplatz. Es wurden mehrere 1000 Stunden Prozessorzeit benötigt, wobei einige 100 Gigabyte an Daten erzeugt wurden.

Während der Analyse der Ereignisse werden zunächst die Myonen mit Hilfe von ORCA rekonstruiert. Die erforderlichen Informationen wie Impuls, Ursprung, rekonstruierte Masse und Ladung werden in einem Objekt gespeichert. Zusätzlich werden auch Daten über Isoltionskriterien der Myonen rekonstruiert und gespeichert. Die Daten aus dem generierten Ereignis werden ebenfalls eingelesen. Aus den Myonen wird nun das physikalische Ereignis rekonstruiert. Dies wird mit Hilfe des in Karlsruhe entwickelten Analysewerkzeuges PAX durchgeführt. Aus zwei entgegengesetzt geladenen Myonen lassen sich Z Bosonen rekonstruieren und in gleicher Weise aus zwei Z Bosonen ein Higgs-Boson. Jede mögliche Kombination der Myonen, auch Ereignisinterpretation genannt, die den Prozess $H \rightarrow ZZ \rightarrow 4\mu$ ergibt, wird in einer Liste abgelegt. Die einzelnen Ereignisinterpretationen werden nun bewertet, indem rekonstruierte Größen, wie beispielsweise die Z Boson Massen, mit Einträgen in Referenzhistogrammen verglichen werden. Die Interpretation mit der besten Bewertung wird als Signalereignis genommen. Nachdem nun das Ereignis rekonstruiert ist, können die Ergebnisse analysiert werden. Um Auflösungsstudien zu ermöglichen, werden die Teilchen aus dem rekonstruierten Ereignis Teilchen aus dem generierten Ereignis zugeordnet. Im Fall der Myonen wird dieses "Matching" durch Vergleich der simulierten und generierten Hits erreicht. Diese Zuordnung ist zuverlässiger als ein "Matching" über die Winkel ϕ und θ, wie es in früheren Studien verwendet wurde. Zum Abschluss der Ereignisanalyse folgt nun die Berechnung des Winkels φ der zur Bestimmung des CP-Eigenwertes des Higgs-Bosons benötigt wird. Die Ergebnisse der Analyse werden im ROOT-Format gespeichert.

Nachdem alle Ereignisse analysiert sind, können die Ergebnisse ausgewertet werden. Dies geschieht mit Hilfe des Analysepaketes ROOT. In Kapitel 6 werden Detektorstudien durchgeführt. Zunächst wurde die Effizienz der Myonenrekonstruktion untersucht. Während der Analyse fiel auf, dass die Rekonstruktionseffizienz deutlich unter den Werten liegt, die in einer früheren Arbeit [26] erzielt, oder im Tracker Technical Design Report [28] spezifiziert wurden. Zudem stellte sich heraus, dass die Effizienz bei höherem Pileup unerwartet niedrig war. Da dieser Effekt auf ein Problem in der Myonenrekonstruktion der CMS Rekonstruktionssoftware zurück zu führen war, und

der Fehler in der verwendeten Version nicht behoben wurde, wurde die Analyse in dieser Studie mit Ereignissen ohne Pileup durchgeführt. Die erzielte Rekonstruktionseffizienz für Signal- und Untergrundereignisse findet man in der Tabelle 6.3.
Nun wurden die Verteilungen von rekonstruierten Größen und deren Auflösung, definiert als $\Delta X = X_{\text{rec}} - X_{\text{gen}}$, untersucht. Die betrachteten Größen waren: Transversalimpulse der vier Signalmyonen, die rekonstruierten Z Boson Massen, das Isolationskriterium der Myonen, die rekonstruierte Higgs-Boson Masse sowie der Transversalimpuls des Higgs-Bosons. Die gemessenen Auflösungen entsprechen sehr genau den Werten in früheren Studien [26, 25, 24] und im Tracker Technical Design Report.
Die in Kapitel 6 untersuchten Größen werden in Kapitel 7 nun als Selektionsgrößen verwendet. In diesem Kapitel wird in einer auf Selektionsschnitten basierenden Analyse die Nachweiswahrscheinlichkeit des Higgs-Bosons mit einer Masse von 200 GeV untersucht. Hierfür wurde eine Prozedur zur Optimierung der Schnitte nach der Signifikanz S_K implementiert. Die hierdurch bestimmten Werte der Selektionsschnitte sind in der Tabelle 7.1 aufgelistet.
Zur Bestimmung der Nachweiswahrscheinlichkeit wurden verschiedene Abschätzungen der Signifikanz verwendet:

- Die sehr verbreitete Ereignis-Zählmethode:

$$S_1 = \frac{N_S}{\sqrt{N_B}} \tag{A.1}$$

- Eine Ereignis-Zählmethode, vorgeschlagen von Bityukov and Krasnikov [30],:

$$S_K = 2 \cdot (\sqrt{N_S + N_B} - \sqrt{N_B}) \tag{A.2}$$

- Eine auf Likelihood-ratio beruhende Ereignis-Zählmethode:

$$S_{CL} = \sqrt{2 \cdot \, lnQ} \tag{A.3}$$

$$Q = \left(1 + \frac{N_s}{N_b}\right)^{N_s + N_b} e^{-N_s} \tag{A.4}$$

N_s und N_b stellen die Anzahl der Signal- und Untergrundereignisse dar. Die Ergebnisse dieser Abschätzungen werden in Tabelle A.1 gezeigt. Das Signal kann eindeutig nachgewiesen werden. Die Unterschiede zwischen den Ergebnissen dieser Studie und denen einer vorherigen Studie dieses Massenbereiches [23], können vollständig mit der kleineren Myonrekonstruktionseffizienz erklärt werden.

	N_S	N_B	S_K	S_1	S_{CL}
$\epsilon_{4\mu} = 66\%$	20.85	4.85	5.74	9.47	6.64
$\epsilon_{4\mu} = 80\%$	25.27	5.87	6.32	10.43	7.31

Table A.1: Die Anzahl der Signal- und Untergrundereignisse N_S und N_B und die verschiedenen Signifikanzabschätzungen: Die Ereignis-Zählmethode nach Bityukov and Krasnikov (verwendet bei der Signifikanzoptimierung): S_K, die einfachste Ereignis-Zählmethode (hier wird die Signifikanz für kleine Ereigniszahlen überschätzt): S_1 und die Poisson Abschätzung: S_{CL}.

In Kapitel 8 wird nun die Möglichkeit der Bestimmung des CP-Eigenwertes des Higgs-Bosons mit Hilfe der Winkelverteilung der Myonen untersucht. Zu diesem Zweck wird die Verteilung

des Winkels φ, zwischen den Zerfallsebenen der Z Bosonen, für CP-gerade Higss-Bosonen mit der Verteilung für CP-ungerade Higgs-Bosonen verglichen. In dieser Studie wird die Verteilung für den CP-ungeraden Fall als Gegenhypothese angesehen und wie eine theoretische Kurve behandelt. Die CP-geraden Ereignisse werden wie Detektordaten behandelt. Es wird nun versucht, die CP-ungerade Hypothese zu widerlegen. Hierfür wird die χ^2-Wahrscheinlichkeit P_{χ^2} für den ungeraden Fall berechnet. $1 - P_{\chi^2}$ entspricht dann der Wahrscheinlichkeit, dass der CP-ungerade Fall ausgeschlossen werden kann.
Zuerst wird die theoretische Verteilung mit generierten Ereignissen reproduziert. Betrachtet man die gleiche Verteilung mit rekonstruierten Ereignissen, so sieht man, dass die Verteilung für $\varphi < 0,5$ stark abfällt. Dies ist die Folge von niedriger Rekonstruktionseffizienz in diesem Bereich. Um die Signalereignisse vom Untergrund zu trennen, wird wieder eine Schnittoptimierung vorgenommen. Allerdings wird diesmal die χ^2-Wahrscheinlichkeit für den CP-ungeraden Fall als Kriterium genommen. Als zusätzliche Selectionsgröße kann nun auch die Higgs-Boson Masse verwendet werden, da die Higgs-Masse als bereits gemessen vorausgesetzt wird. Das Ergebnis der Schnittoptimierung für eine integrierte Luminosität von $\int L = 300\,\mathrm{fb}^{-1}$ kann man in Abbildung A.2 sehen. Die χ^2-Wahrscheinlichkeit P_{χ^2} liegt bei 0.36 %. Diesen Wert für $\int L = 300\,\mathrm{fb}^{-1}$ kann man für andere Luminositäten extrapolieren. Das Ergebnis sieht man in Abbildung A.3. Der Hypothese eines CP-ungeraden Higgs-Bosons lässt sich also während der Laufzeit des LHC ausschliessen.

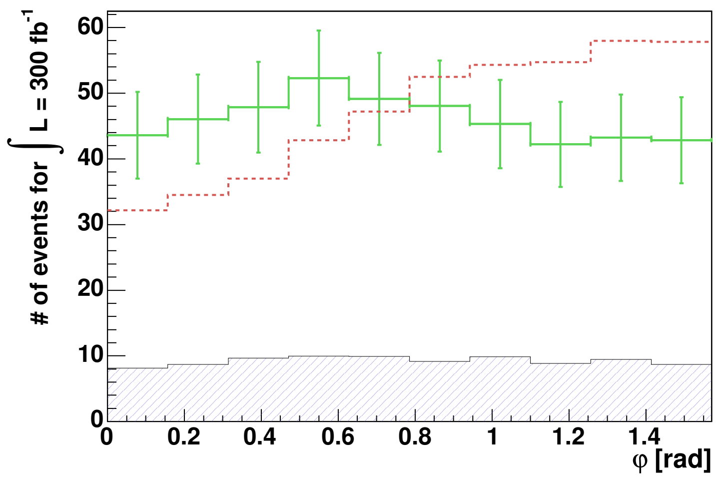

Figure A.2: Verteilung des Winkels φ nach der Anwendung optimierter Schnitte. $m_{\mathrm{Higgs}} =$ 200 GeV, CP-gerades Higgs $\equiv$ grün, CP-ungerades Higgs $\equiv$ rot gestrichelt und der gesamte Untergrund $\equiv$ blau schraffiert. Die Fehlerbalken der CP geraden Verteilung stellen den statistischen Fehler für eine integrierte Luminosität von $300 fb^{-1}$ dar.

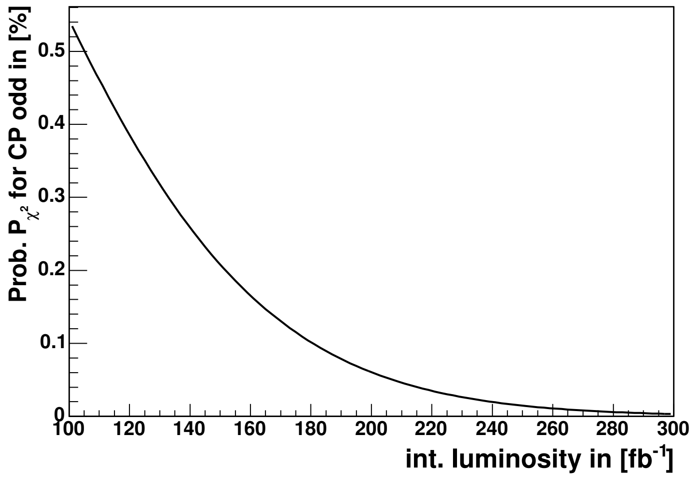

Figure A.3: Wahrscheinlichkeit P_{χ^2} für die CP-ungerade Hypothese, in Abhängigkeit von der integrierten Luminosität.

Trotz erfolgreicher Ergebnisse dieser Studie bleiben Aufgaben für die Zukunft. So müssen beide Analysen mit einer Version der CMS Rekonstruktiossoftware wiederholt werden, in der die Probleme der Rekonstruktionseffizienz gelöst sind. In der Analyse des CP-Eigenzustandes des Higgs-Bosons sollte zudem eine bessere Signifikanzabschätzung als die χ^2-Wahrscheinlichkeit verwendet werden. Zusätzlich können aussagekräftigere Observablen als der Winkel φ, die in theoretischen Betrachtungen vorgeschlagen wurden, verwendet werden. Ein weiterer Punkt ist die Möglichkeit, die auf Schnitten basierende Ereignisselektion durch Likelihood Methoden oder neuronale Netzwerke zu ersetzen. Diese Verbesserungen sollten allerdings aufgrund der objektorientierten Implementation der Analyse leicht durchzuführen sein.

Danksagung

Ich möchte mich zuerst bei Herrn Prof. Dr. Günter Quast bedanken. Ich hätte mir keine bessere Betreuung wünschen können. Die Aufgaben haben mir sehr viel Spaß gemacht. Er ließ viel Platz für Eigeninitiative, hatte aber immer ein Ohr für Fragen offen, so dass ich viel lernen konnte.

Ich danke auch Herrn Prof. Dr. Thomas Müller für die Übernahme des Korreferats.

Dank gilt auch Dr. Klaus Rabbertz, der stets Zeit für meine Fragen hatte und mir viele Male weitergeholfen hat. Nicht weniger danke ich ihm für seinen ständigen Einsatz, um aktuelle CMS Software zur Verfügung zu stellen.

Der Grund, weshalb ich immer gerne hier ans Institut komme, ist die nette Atmosphäre. Ich fühle mich hier sehr wohl, und das ist der Verdienst von: Christopher Jung, Ulrich Felzmann, Steffen Kappler, Deborah Miksat, Christian Piasecki und Alexander Schmidt. Ich danke ihnen nicht nur für Hilfe und Ratschläge, sondern vor allem für die schöne Zeit. Natürlich gehen auch Dankesgrüße ans CERN an Joanna Weng und Christian Weiser.

Den Systemadministratoren am EKP kann man garnicht genug danken. Sie investieren viel Zeit und Mühen, um alles am Laufen zu halten, und sind trotzdem immer hilfsbereit und finden auch im grössten Stress freundliche Worte. Vielen Dank an: Yves Kemp, Ulrich Kerzel, Jens Rehn, Christian Sander und Thorsten Scheidle.

Vielen Dank an alle Korrekturleser. Noch nicht erwähnt habe ich Giulia Conforti, Stefanie Freudenstein, Thomas Gnielka und Marc Herold.

Ganz besonders möchte ich mich bei meinen Eltern und meiner Freundin bedanken. Sie haben mich immer unterstützt und mir den Rücken gestärkt. Sie haben mir erst alles möglich gemacht.

Hiermit versichere ich, die vorliegende Arbeit selbständig verfasst und nur die angegebenen Hilfsmittel verwendet zu haben.

Sven Schalla

Karlsruhe, den 1. Juni 2004